ABSTRACT

ABDULMOJEED, MUSTAPHA BABATUNDE. Advancing SABRE-SHEATH Hyperpolarization for pH Sensing and Reaction Monitoring. (Under the direction of Prof. Thomas Theis).

This thesis presents the development and application of Signal Amplification by Reversible Exchange (SABRE) for the hyperpolarization of novel biologically and chemically relevant molecules. Specifically, it highlights the use of SABRE-SHEATH as an efficient method to increase signal sensitivity in novel MRI pH probe, such as Z-4-methyl-2-oxopent-3-enedioic acid ([1,5-$^{13}C_2$]-Z-OMPD). The first three chapters introduce the principle of hyperpolarized magnetic resonance, parahydrogen, and the SABRE technique. Chapter 4 describes the successful hyperpolarization of [1,5-$^{13}C_2$]-Z-OMPD using SABRE-SHEATH. Chapter 5 focuses on the direct hyperpolarization of imidazole in water, addressing the challenge of SABRE biocompatibility for pre-clinical and clinical application. Finally, chapter 6 demonstrates the application of SABRE-SHEATH hyperpolarization for real-time reaction monitoring, using the diazonium product of ^{15}N-labelled sodium nitrite and its azo coupling reactions with phenol and cresol as a model.

Advancing SABRE-SHEATH Hyperpolarization for pH Sensing and Reaction Monitoring

by
Mustapha Babatunde Abdulmojeed

A dissertation submitted to the Graduate Faculty of
North Carolina State University
in partial fulfillment of the
requirements for the degree of
Doctor of Philosophy

Chemistry

Raleigh, North Carolina
2025

APPROVED BY:

Thomas Theis Committee Chair	Vincent Lindsay
Alexander Nevzorov	Elena Jakubikova

DEDICATION

To my lovely family: Nafisah, Aaminah, Abdurrahmaan, Anas and Uthman.

BIOGRAPHY

Mustapha Abdulmojeed grew up in the city of Akoka, Lagos State, Nigeria. Despite not formally educated, His parents were keen on providing the best educational experience for him and his siblings. Afterall, Akoka is the host of many of the nation's top educational institutions, which includes University of Lagos, Yaba College of Technology, and CMS Grammar School Lagos, among others. The latter being the oldest high school in Nigeria. Thus, Mustapha grew up like a normal Akoka kid, coasting through the school system until completing high school in 2004.

He then took a three-year break to study the Islamic sciences—a tradition his father had followed with his siblings—before being admitted to Ladoke Akintola University of Technology (LAUTECH) to study transport management, a course he did not enjoy. Therefore, it was not surprising that he switched majors to chemistry in the second year of college. Chemistry was Mustapha's favorite science subject in high school; it was only apt that the two friends united in college.

Mustapha graduated from college in the summer of 2014 with a first-class honor as the best graduating student in chemistry, that year. In the next four years after graduation, he worked as a college educator in both private and public institutions in Nigeria until he was admitted to Middle Tennessee State University in the fall of 2018 to pursue a master's degree in chemistry on a graduate assistantship award. Here, Mustapha rekindled his love for chemistry, honing is skill in physical organic chemistry under the supervision of Dr. Andrienne Friedli and Dr. Piotr Kaszynski.

In the fall of 2020, at the height of COVID, Mustapha was proud to be admitted to the chemistry PhD program at NC State, where He felt enamored of the hyperpolarization techniques in Dr. Thomas Theis lab. This feeling led him to make a bold decision to join the Theis lab. A decision he would continue to cherish.

ACKNOWLEDGMENTS

I am grateful to my creator who has endowed me with the faculty to acquire knowledge and the ability to synthesize and analyze information to contribute positively to humanity. I am thankful to my parents, who despite their modest background and resources, encouraged and supported my siblings and I on the path of seeking meaningful knowledge. I am grateful to my wife for supporting me and taking care of our kids while I wander in the wilderness of the research laboratory.

I am grateful to those who have mentored, taught, lectured, encouraged or advised me on this journey. Specifically, I would like to thank my undergraduate advisors Dr. Abdulhameed Misbaudeen and Dr. Adewusi John Adepeju who guided and inspired my chemistry journey. My utmost gratitude to Dr. Andrienne Friedli and Dr. Piotr Kaszynski for training me in boron cluster chemistry and helping me hone my synthetic skills. I am grateful to Dr. Simon Kapuszynski, a postdoctoral candidate in Dr. Friedli' s lab, who showed me some of the in's and out in the lab.

I am grateful to NC State chemistry for creating a welcoming, safe and rigorous program to grow as a chemist. I am particularly thankful to my advisor, Dr. Thomas Theis, for his kind words as always, dedication and passion to educate and get the best out of me as a scientist. I am grateful to my committee, Dr. Vincent Lindsay, Dr. Alexander Nevzorov, Dr Elena Jakubikova and Dr. David Schultz.

Finally, I would like to thank all my colleagues, both current and past members in the Theis hyperpolarization lab: Stephen McBride, Christopher Nelson, Seth Dilday, Megan Pike, Brojo Dhali, Erica Curran, Nicholas Volya, Rielly Harisson, Franziska Theiss, Reagan Womack, Abdul-Rahman Sweilam, Iuliia Mandzhieva, Adam Ortmeier, Austin Browning, Keilian MacCulloch, Patrick TomHon and Soeren Lehmkuhl. I am grateful for every minute I spent working with this

group of talented and hardworking scientists. I would not have achieved this without you all. Thank you.

TABLE OF CONTENTS

LIST OF TABLES

LIST OF FIGURES

Chapter 1 Background

1.1 Magnetic Resonance

Magnetic resonance is arguably the most informative analytical technique widely used across multiple fields of science[1]. It relies on the weak interaction of nuclear spins with external magnets under certain matching conditions commonly referred to as resonance (*hence the name Magnetic Resonance*). There are two major MR techniques: Nuclear Magnetic Resonance (NMR)[2,3] and Magnetic Resonance Imaging (MRI)[4–6].

Nuclear Magnetic Resonance (NMR) spectroscopy is a widely used analytical technique in chemistry, particularly for the structural elucidation of organic compounds[7–10]. In the field of structural biology, multidimensional NMR methods enable detailed investigation of protein structures and their dynamic behavior[11–15]. Beyond the laboratory, Magnetic Resonance Imaging (MRI) is routinely employed in medical diagnostics to non-invasively visualize internal body structures, aiding in the diagnosis of diseases and monitoring of therapeutic outcomes[16–18].

The origin of magnetic resonance is tightly linked to the discovery of nuclear spin. Spin is an intrinsic quantum property of particles such as electrons and nuclei. Its existence was first demonstrated in the early 20th century through the pioneer Stern-Gerlach experiment[19]. As spin possess angular momentum, it also gives rise to a magnetic moment, making particles responsive to external magnetic field. Magnetic resonance techniques leverage this property to non-destructively extract detailed information about a wide range of materials of all kinds, from solids[2,20–22] to fluids[2,7,23], macromolecules[24,25] to small molecules[7,10], and systems ranging from subsurface of the earth[26] to interstellar space[27]. The profound scientific and practical significance of MR techniques have been recognized through the awarding of seven Noble prizes across the fields of physics, chemistry, and medicine[1].

1.2 Sensitivity Challenge in NMR and MRI

Magnetic resonance, despite its numerous applications, suffers from low sensitivity.[28,29] This limitation stems from low thermal polarization. Thermal polarization refers to the difference in population between specific nuclear spin states at a given temperature and magnetic field.[28–30]

This inherent limitation in sensitivity originates from small population difference between nuclear Zeeman states, the source of signal in NMR and MRI. To break it down further, consider an ensemble of nuclei, with spin angular momentum I. According to quantum mechanics, the system would consist of 2I+1 degenerate states. In the presence of a static magnetic field B_0, the degeneracy of the states is broken into m Zeeman states ($m \in \{-I,-I+1,\ldots I-1,+I\}$) as illustrated in Figure 1.

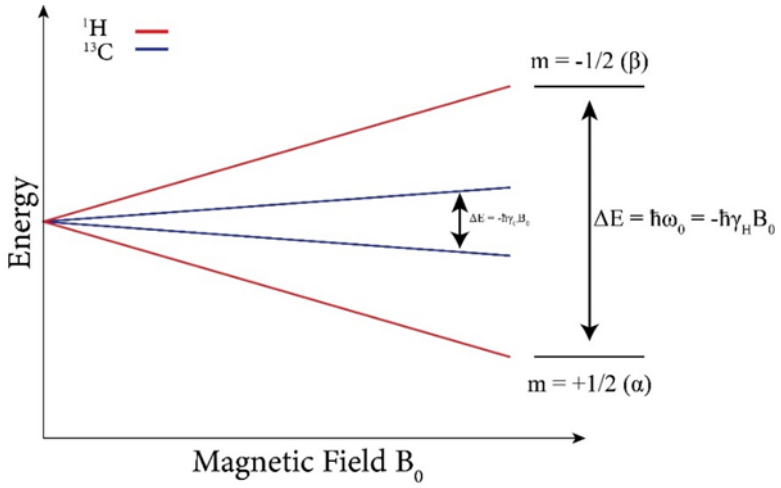

Figure 1.1. The Zeeman splitting of 1H and 13C in the presence of Magnetic field B0.

For a spin ½ system, such as ^{1}H, ^{13}C, and ^{15}N, two degenerate states are formed (2(1/2)+1=2) with $m_s = \pm 1/2$ values and energies:

$$E_m = -m\gamma\hbar B_0 \qquad \text{Eq 1.1}$$

Where γ is the gyromagnetic ratio, a fundamental property unique to all nuclei which measures their magnetic susceptibility, ħ is the reduced Planck's constant. The population difference per total number of nuclei between these two states (±1/2, or α and β) also known as Polarization, P is given by the Boltzmann distribution as shown in equation 1.2:

$$P = \frac{n_\alpha - n_\beta}{n_\alpha + n_\beta} = tanh\left(\frac{\gamma \hbar B_0}{2k_B T}\right)$$

Eq 1.2

Where n_α and n_β is the population in the α and β states at thermal equilibrium. The difference in energy between the two states is described in equation 1.3.

$$\Delta E = \gamma \hbar B_0 \qquad \text{Eq 1.3}$$

ΔE is very small compared to thermal energy ($k_b T$) at ambient temperatures. Therefore, both states are almost equally populated. For example, from Eq 1.2, the Polarization at 298 K corresponds to 3ppm/T, this means for an 11.7 T (^{1}H 500 MHz) magnet, only 35.1 ppm polarization is achieved. This means for every 1 million ^{1}H nuclei in the sample, only ~35 of them is giving the signal seen on the instrument, the others are silent.

Consequently, the pursuit of enhanced NMR signal sensitivity has been a central focus for researchers, scientists, and commercial institutions since the inception of the technique.[1] This drive has led to the development of high-field superconducting magnets, capable of generating magnetic fields corresponding to resonance frequencies exceeding 1.2 GHz.[28,29] While high-field NMR offers significant advantages in terms of resolution and sensitivity, the associated costs, large physical footprint, and potential safety concerns render such systems impractical for many applications. These include routine clinical MRI scans, industrial quality control, and subsurface investigations in fields such as oil exploration. As a result, various strategies have been developed to boost NMR signal strength by increasing nuclear spin polarization independently of the main magnetic field (B_0). These techniques are collectively referred to as hyperpolarization (HP).[25,29]

Hyperpolarization refers to the process of perturbing an ensemble of nuclear spins from their thermal equilibrium distribution into a non-Boltzmann state. In such a state, one spin energy level becomes significantly overpopulated relative to the other, resulting in a substantial increase in net magnetization. This enhanced magnetization directly translates into a dramatic improvement in signal intensity in magnetic resonance experiments. Achieving hyperpolarization requires an external source of spin order to drive the system away from equilibrium. Several techniques have been developed to accomplish this, each exploiting different physical principles. The three most employed hyperpolarization methods are summarized below.[28–32]

1.3 Hyperpolarization methods

1.3.1 Dynamic Nuclear Polarization (DNP)

Dynamic Nuclear Polarization (DNP) is one of the earliest hyperpolarization methods developed in magnetic resonance.[33–39] In this method, the target nuclei are placed in contact with an unpaired electron, the relatively large thermal polarization of the electron is then transferred to the target nuclei via the application of microwave irradiation at or near the electron spin resonance (ESR) transition frequency.[34,40] This method has been extensively studied and used to hyperpolarize a wide range of MRI contrast agents, such as ^{13}C-pyruvate which is a subject of several pre-clinical and clinical trials for diagnosing, assessing and monitoring various types of cancers.[41,42] The robustness, reproducibility and large polarization achieved with DNP is unparalleled among other HP methods, however DNP polarizers are very expensive, often characterized with large footprints and require time and expertise to run.

1.3.2 Spin Exchange Optical Pumping (SEOP)

Spin exchange optical pumping (SEOP) is another example of hyperpolarization method that is used in polarizing gases such as ^{3}He, ^{129}Xe and ^{83}Kr. Here, polarization is transferred from laser photons to the electrons of an alkali metal vapor placed in a closed jar containing the target gas and a gaseous buffer.[43,44] The ensuing nuclear collision between the target and the polarized electrons of alkali metals results in the polarization of noble gases. This method has been used clinically to evaluate pulmonary structure and function, in addition to ventilation imaging.[45]

1.3.3 Parahydrogen Induced Polarization (PHIP)

Finally, Parahydrogen induced hyperpolarization is a relatively new hyperpolarization technique that uses parahydrogen as the spin order source. Details of this method will be discussed in subsequent chapters of this thesis as the work presented here is solely based on PHIP.

1.4 Outline and Summary

This thesis begins by introducing the fundamental principles of hyperpolarization in magnetic resonance and briefly surveys the three main hyperpolarization methods. A detailed discussion of parahydrogen-induced hyperpolarization (PHIP) is presented in chapter 2, beginning with the theory of hydrogen spin isomers, leading to the generation, storage and application of parahydrogen.

Chapter 3 offers an in-depth overview of Signal amplification by reversible exchange (SABRE), explaining the underlying chemistry and physics that enable the technique. This Chapter lays the groundwork for the subsequent chapters by detailing the mechanism of catalyst-substrate exchange and spin order transfer central to SABRE.

Chapter 4 presents a previously published work describing the successful hyperpolarization of a novel MRI pH sensor, Z-4-methyl-2-oxopent-3-enedioic acid ([1,5-$^{13}C_2$] Z-OMPD). This study illustrates the potential of SABRE for enhancing the sensitivity of MRI contrast agents.

Chapter 5 focuses on the direct hyperpolarization of imidazole in aqueous media using a water-soluble catalyst. The work addresses key challenges in SABRE biocompatibility and achieves signal enhancements not previously reported for direct SABRE in water.

Finally, chapter 6 demonstrates the application of SABRE-SHEATH for real-time reaction monitoring. Using ^{15}N-labelled sodium nitrite as a hyperpolarized probe, this chapter showcases the ability to track the transformation of reactants to intermediates and products during azo dye formation, highlighting the utility of SABRE in mechanistic studies.

Chapter 2 : Parahydrogen: Theory and Applications

2.1 Parahydrogen

The hydrogen molecule has two spin isomers.[46–49] Spin isomer refers to how the hydrogen nuclear spins are oriented with respect to each other, like how electrons are paired in an atomic orbital. The hydrogen nuclei in the dihydrogen molecule can either be parallel to each other or anti-parallel. The parallel states are known as orthohydrogen. They have a total spin F=1, and thus are triply degenerate (also called triplet state: T_{+1}, T_0, T_{-1}). The anti-parallel state is known as parahydrogen. It has a total spin F=0, and therefore it is singlet. At room temperature, hydrogen gas has a 3:1 ratio of ortho to para isomers. Spin isomerism in the hydrogen molecule was first postulated by Werner Heisenberg.[46] This was confirmed experimentally by Hund and Dennison.[48] Subsequently, Bonhoeffer and Harteck isolated parahydrogen and showed the interconversion of the ortho and para isomers of hydrogen.[49]

The origin of the two distinct spin isomers of hydrogen can be explained through the Pauli exclusion principle,[50] which states that: "The total wavefunction of a homonuclear diatomic molecule made of two bosons (particle with integer spin angular momentum) is symmetric with respect to interchange of the particles, while that made of fermions (particle with half-integer spin angular momentum) is antisymmetric."

The hydrogen molecule consists of two hydrogen atoms whose nucleus each have half-integer spins. Therefore, according to the Pauli principle above, the total wavefunction of the hydrogen molecule must be antisymmetric with respect to interchange of the hydrogen nuclei. Using the Born-Oppenheimer approximation,[51] the total wavefunction of the hydrogen molecule can be expressed as a product of electronic (Ψ_E), translational (Ψ_T), vibrational (Ψ_V), rotational (Ψ_R), nuclear-spin (Ψ_{NS}) wavefunctions.[52]

$$\Psi_{tot} = \Psi_E \Psi_T \Psi_V \Psi_R \Psi_{NS}$$

Eq 2.1

The electronic, translational, and vibrational wavefunctions for the hydrogen molecule are all symmetric with respect to nuclei interchange, therefore, for the Ψ_{tot} to be antisymmetric, Either the rotational (Ψ_R) or nuclear spin state (Ψ_{NS}) must be antisymmetric. In other words, both wave functions correlate to one another.

$$\Psi_{tot}^{antisym} = \Psi_E \Psi_T \Psi_V \, (\Psi_R^{sym} \Psi_{NS}^{antisym} \; or \; \Psi_R^{antisym} \Psi_{NS}^{sym})$$

Eq 2.2

The rotational wavefunction of the hydrogen molecule is mathematically described by spherical harmonics (rotational states J = 0,1,2,3,4…). The same mathematical model used to describe the atomic orbitals (l = 0,1,2,3,4…). The even rotational states (J = 0,2,4…) are symmetric just like *s* (l = 0) and *d-orbitals* (l = 2) while the odd rotational states (J = 1,3,5…) are antisymmetric similar to *p* (l = 1) and *f -orbitals* (l = 3).[52] Importantly, the rotational states are 2J+1 degenerate and their energy is given by:

$$E_J = BJ(J+1)$$

Eq 2.3

Where B is the rotational constant which for hydrogen, B = 60.8 cm^{-1}.[52] The energy spacing between the states can be computed from equation 2.3. For example, the energy spacing between the J = 0 and J = 1 can be computed as follows:

$$\Delta E_{0,1} = E_1 - E_0 = 60.8 \; cm^{-1}[(1(1+1) - (0(0+1)] = 2 \times 60.8 = 121.6 \; cm^{-1}$$

Considering that the thermal energy (k_bT) available at 298 K is ≈ 207.1 cm^{-1}, at least the first four rotational states are accessible at standard conditions.

Moving gears to the spin wavefunction, the hydrogen molecule could only have four possible arrangements:

α(1)α(2) β(1)β(2) α(1)β(2) β(1)α(2)

Where α denotes by convention a spin aligned up (↑) or positive spin (+) and β, denotes spin aligned down (↓) or negative spin (-). The index 1 and 2 in parentheses labels the hydrogen nuclei. For example, α(1)α(2) means both hydrogen nuclei are spin up whereas β(1)β(2) means both are spin down. It is evident that in the first two scenarios, if we interchange the nuclei, nothing happens, thus both terms are symmetric with respect to exchange. However, if we interchange any of the last two terms, α(1)β(2) → β(1)α(2), we arrive at a new wavefunction different from the one we start with. In quantum mechanical terms, the last two terms are not an eigenfunction of the interchange operator (permutation operator) and thus they are neither symmetric nor antisymmetric with respect to exchange.

However, a linear combination of the two terms {α(1)β(2), β(1)α(2)} leads to two additional wavefunctions {$1/\sqrt{2}$ [α(1)β(2) - β(1)α(2)], and $1/\sqrt{2}$ [α(1)β(2) + β(1)α(2)]}. Where $1/\sqrt{2}$ is the normalization constant. It can be shown that the first of these two linear combinations is antisymmetric with respect to exchange and the other is symmetric.[32,52]

Thus, we have three symmetric spin states (T_{+1} = α(1)α(2), T_0 = $1/\sqrt{2}$ [α(1)β(2) + β(1)α(2) , and T_{-1} = β(1)β(2)) of the hydrogen molecule which we previously described as orthohydrogen. The states can only exist in the odd rotational states due to Pauli principle. The fourth spin state is the singlet state also known as parahydrogen as mentioned earlier in the chapter. parahydrogen is antisymmetric with respect to exchange and only exists in the even rotational states of the hydrogen molecule (see Table 2.1).

Table 2.1. Vector representation of the spin isomers of hydrogen and their coupled rotational states

	Even Rotational states (J = 0,2,4…) symmetric	Odd Rotational states (J = 1,3,5…) antisymmetric
Singlet Parahydrogen antisymmetric 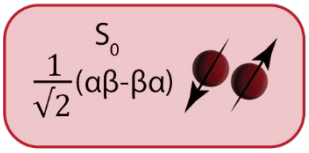	Allowed	Forbidden
Triplet orthohydrogen symmetric 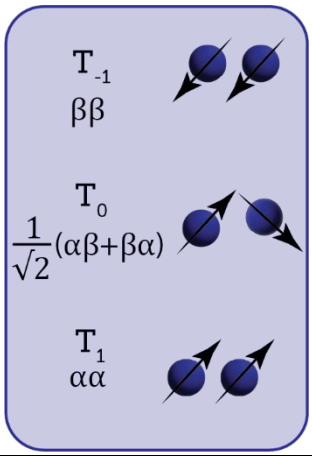	Forbidden	Allowed

In essence, the hydrogen molecule consists of two different gases (ortho and parahydrogen) each with unique physical properties. The relative population of the two gases can be calculated using the Maxwell-Boltzmann statistics[52,53] given below:

$$\frac{N_{para}}{N_{ortho}} = \frac{(2I+1)\sum_{J=even}(2J+1)e^{\left(-\frac{J(J+1)\Theta_R}{T}\right)}}{(2I+1)\sum_{J=odd}(2J+1)e^{\left(-\frac{J(J+1)\Theta_R}{T}\right)}} \qquad \text{Eq 2.4}$$

Where I is the degeneracies of the spin states. the triple states are three-fold degenerate, since I =1 from equation 1.1, and the singlet state is one-fold degenerate, I = 0, therefore, Eq 2.4 can be collapsed to:

$$\frac{N_{para}}{N_{ortho}} = \frac{\sum_{J=even}(2J+1)e^{\left(-\frac{J(J+1)\Theta_R}{T}\right)}}{3\sum_{J=odd}(2J+1)e^{\left(-\frac{J(J+1)\Theta_R}{T}\right)}} \quad \text{Eq 2.5}$$

J is the rotational quantum number, T is temperature in Kelvin, while Θ_R is the rotational temperature and is given by[52,53]:

$$\Theta_R = \frac{B}{k_b} = \frac{h^2}{8\pi^2 I k_b} \quad \text{Eq 2.6}$$

k_b is the Boltzmann constant, h is Planck's constant and I is the moment of inertia of the molecule. Using Θ_R = 87.5 K and plotting Eq 2.5 for the first four terms. It can be shown from Figure 2.1 that at or above room temperature all the rotational states are populated, therefore the ratio of para to ortho depends on only the spin state degeneracies. Thus, we expect 25% of dihydrogen will be in the para state under this condition, this is akin to normal hydrogen gas. At liquid Nitrogen temperature (77K), and in the presence of a suitable catalyst, the ratio of para to ortho in dihydrogen can be increased by 50%, a sample of hydrogen containing such composition, is said to be 50% para enriched.

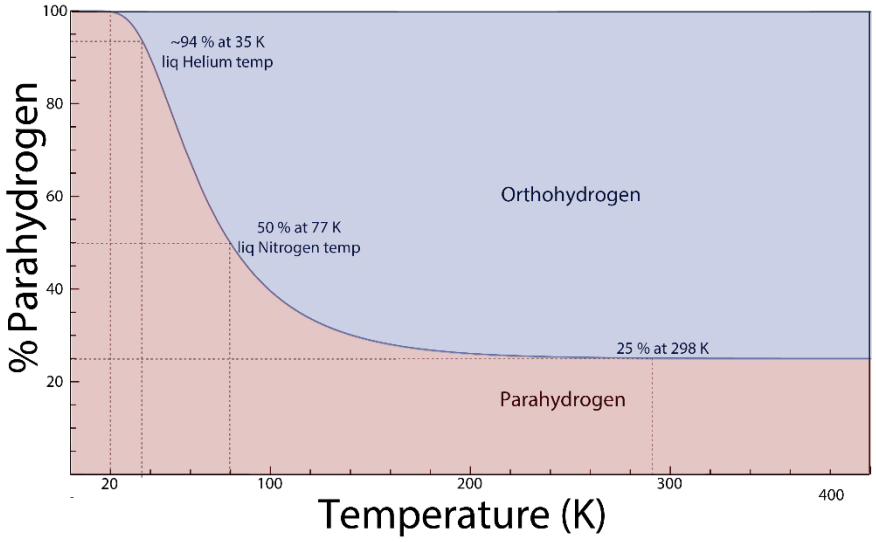

Figure 2.1. Plot of percentage parahydrogen content in normal hydrogen as a function of temperature in the presence of a suitable catalyst.

2.2 Parahydrogen generation

The spontaneous conversion from orthohydrogen to parahydrogen is very slow on the orders of days even at cryogenic temperatures. This is because the conversion involves a spin-flip which is symmetrically forbidden.[54]

There are two main ways to generate parahydrogen. The first method requires dissociation of hydrogen gas on the surface of a heterogeneous catalyst, then recombining the atoms at cryogenic temperatures where the formation of para state is thermodynamically favored, followed by desorption of the mostly pure parahydrogen gas.[54–56] The second method requires the use of inhomogeneous magnetic material such as rust (FeO(OH) or charcoal to alter the magnetic moment of the spins and thereby induce a spin flip.[55–58] The latter method has been extensively studied, and several reviews have been dedicated to the development and efficiency of the process.[59] Today, commercial products are available for in-house production of up to 100% parahydrogen such as

the one developed by Hovener et al[60] pictured in **Figure 2.2** (left). A home-built parahydrogen generator, pictured in **Figure 2.2** (right) can be assembled with little cost (~$100) to generate up to 50% parahydrogen.[61]

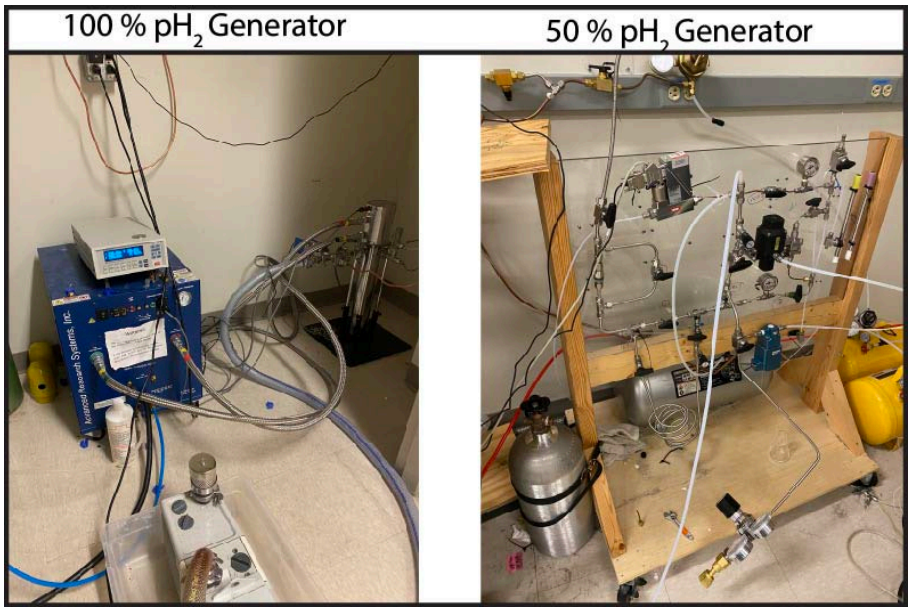

Figure 2.2. Parahydrogen generators. (Right) 100% parahydrogen generator composed of the reactor (silver cylinder), a helium compressor and cryostat (blue) for cooling the temperature down to 28K. (LEFT) A 50% parahydrogen generator mounted on a plexy glass.

2.3 Applications of parahydrogen

2.3.1 Hydrogen storage

The initial drive for parahydrogen production emanates from the rapid rise in the use of hydrogen gas as rocket fuel in post-World War II. Hydrogen gas is typically liquefied for long term storage purposes. However, at liquid hydrogen temperatures, orthohydrogen is less stable

compared to parahydrogen, thus it undergoes a process called spin-flip due to intermolecular collisions and slowly transforms to parahydrogen. Unfortunately, the enthalpy of the spin flip process is higher compared to the enthalpy of evaporation of liquid hydrogen. Therefore, liquefied hydrogen evaporates substantially resulting in loss of more than 30 % of the stored hydrogen. Converting normal hydrogen to highly enriched parahydrogen before liquefaction can significantly reduce the loss of hydrogen to about 0.3 %. Hence lots of effort was spent in finding efficient means of converting normal hydrogen to highly enriched parahydrogen.[56,59,62]

2.3.2 Parahydrogen Induced Hyperpolarization

Another event that catalyzes the research in parahydrogen generation is its use in magnetic resonance to dramatically increase signal intensities of unsaturated substrates by pairwise addition. Parahydrogen has zero spin angular momentum and therefore it is NMR silent. However, it's pairwise addition to an unsaturated substrate or metal center results in large detectable antiphase NMR signal of the corresponding protons in the product molecule, as predicted and demonstrated by Bowers and Weitekamp.[63] This technique is termed parahydrogen induced hyperpolarization (PHIP).[64] Since the work presented in this thesis is a variant of PHIP, I would like to give a brief overview about PHIP in this chapter before proceeding,

In PHIP, two conditions must be met for NMR signal to become detectable, 1) the resulting protons must be magnetically distinct. In other words, the symmetry from the initial parahydrogen molecule must be broken through chemical shift differences or distinct coupling partners. 2) the reaction must happen faster than the relaxation of the protons.[63–65] Figure 2.3 illustrates the basic principle of PHIP, the initial parahydrogen spin state ($\frac{1}{\sqrt{2}}|\alpha\beta - \beta\alpha\rangle$) corresponds only to the $|\alpha\beta\rangle$ and $|\beta\alpha\rangle$ states, thereby upon reaction, these two states are overpopulated and results in a pair of

absorption (1,3) and emission (2,4) peaks corresponding to $|\beta\alpha\rangle \rightarrow |\beta\beta\rangle$, $|\alpha\beta\rangle \rightarrow |\beta\beta\rangle$ and $|\alpha\beta\rangle \rightarrow |\alpha\alpha\rangle$, $|\beta\alpha\rangle \rightarrow |\alpha\alpha\rangle$ transitions, respectively.

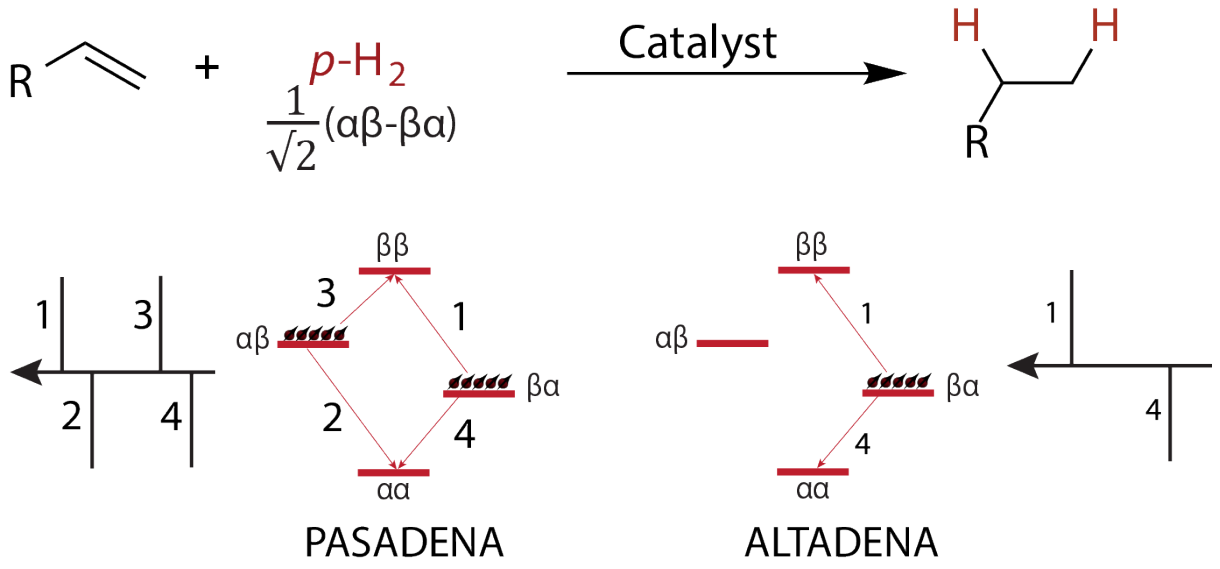

Figure 2.3. (TOP) Hydrogenation of an unsaturated compound using parahydrogen. (Bottom) A schematic diagram depicting both PASADENA and ALTADENA effect.

Historically, PHIP can be done in two ways; When the reaction and detection are carried out at high field (weak coupling regime), this process is termed PASADENA.[65] On the other hand, if the reaction is done at low field (strong coupling regime), and detected at high field, the process is termed Adiabatic Longitudinal Transport After Dissociation Engenders Nuclear Alignment (ALTADENA).[66] In this case, either $|\alpha\beta\rangle$ or $|\beta\alpha\rangle$ is overpopulated not both, resulting in only an absorption (1) and emission (4) enhanced peaks corresponding to transitions $|\beta\alpha\rangle \rightarrow |\beta\beta\rangle$ and $|\beta\alpha\rangle \rightarrow |\alpha\alpha\rangle$.[66,67]

Incorporating hydrogen directly into a target substrate, to induce hyperpolarization also known as hydrogenative PHIP has been widely used in organic and inorganic chemistry to probe hydrogenation reactions as well as trace reaction intermediates.[68–72] Magnetic field cycling

(MFC)[73,74] and specialized pulse sequences[75–77] have been employed in tandem with PHIP chemistry to allow more efficient spin order transfer into target nuclei. Heteronuclear targets, such as ^{13}C and ^{15}N, have further extended the application of PHIP to biomedical applications via the preparation of hyperpolarized contrast agents for different imaging protocols.

Furthermore, spin order transfer (SOT) through parahydrogen is not limited to h-PHIP. Pairwise replacement of hydrogen,[78] single hydrogen replacement,[79] or addition of one hydrogen[80,81] to a target substrate are all possible ways by which parahydrogen have been used to achieve SOT (see **Figure 2.4**).

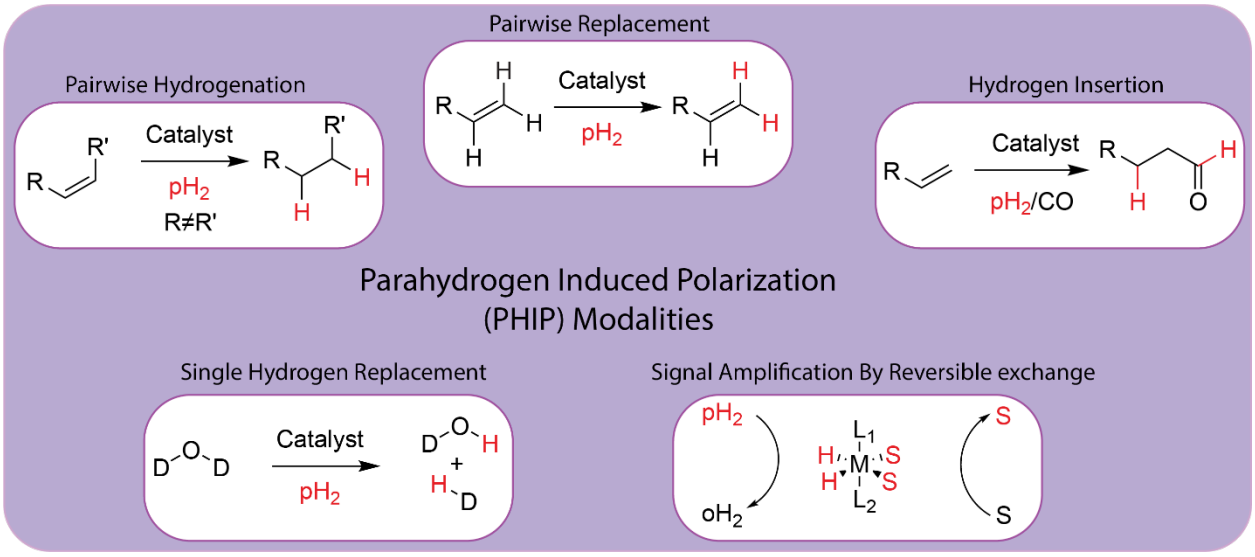

Figure 2.4. An overview of PHIP modalities

The limited substrate scope of h-PHIP and the need to expand the library of hyperpolarizable MRI contrast agents have resulted in several innovative solutions. The first of which is termed Side Arm Hydrogenation PHIP (PHIP-SAH), this method uses an unsaturated ester precursor of the target substrate for the hydrogenation process, thereafter polarization is transferred to the heteronuclear atom of interest in the substrate using either a pulse sequence or

magnetic field cycling (MFC) method. Subsequently, the hydrogenated part of the ester is cleaved off through hydrolysis, and the hyperpolarized substrate can be extracted through phase separation as shown in **Figure 2.5.** This method has been used to hyperpolarize ^{13}C-Pyruvate, an important metabolite leading current clinical trials.[82–84]

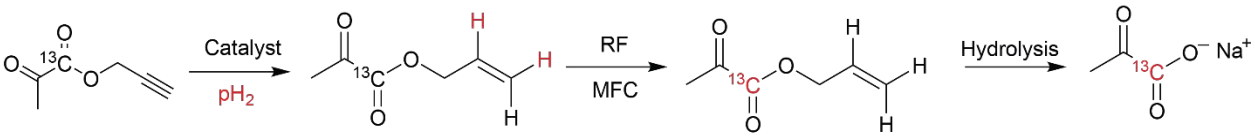

Figure 2.5. A typical PHIP-SAH procedure showing the hydrogenation of the unsaturated carboxylate with parahydrogen, followed by transfer of polarization from the added hydrogens to the 13C nuclei of the carboxylate before hydrolysis to fashion a 13C hyperpolarized pyruvate

Additionally, A novel approach was invented by Ducket et al in 2009, which does not require hydrogenation, rather, an organometallic catalyst which reversibly binds to parahydrogen and the substrate of interest is used to mediate the transfer of polarization. This method termed Signal Amplification by Reversible Exchange (SABRE), has further expanded the substrate scope of parahydrogen-based hyperpolarization methods to include, amines, alcohols, alpha-keto acids , imidazoles etc. The following chapter will be dedicated to this method as all the work presented in this document is based on the SABRE approach.

Chapter 3 : Signal Amplification by Reversible Exchange (SABRE)

3.1 Introduction

SABRE is a parahydrogen-based hyperpolarization technique that dramatically enhances the magnetic resonance signal in a target molecule without incorporating hydrogen into the molecule.[85–87] The polarization transfer in SABRE is enabled by an organometallic catalyst which facilitates the temporary contact between parahydrogen and a target molecule through a series of ligand association and dissociation steps.[67,88] This technique also termed non-hydrogenative PHIP eliminates the long-standing requirement for unsaturated substrates in parahydrogen induced hyperpolarization (PHIP) methods. Thereby expanding parahydrogen-based method to a wider array of molecules with the only limitation that the molecules must at least have a Lewis base site that can bind with the magnetization transfer catalyst.[67,89]

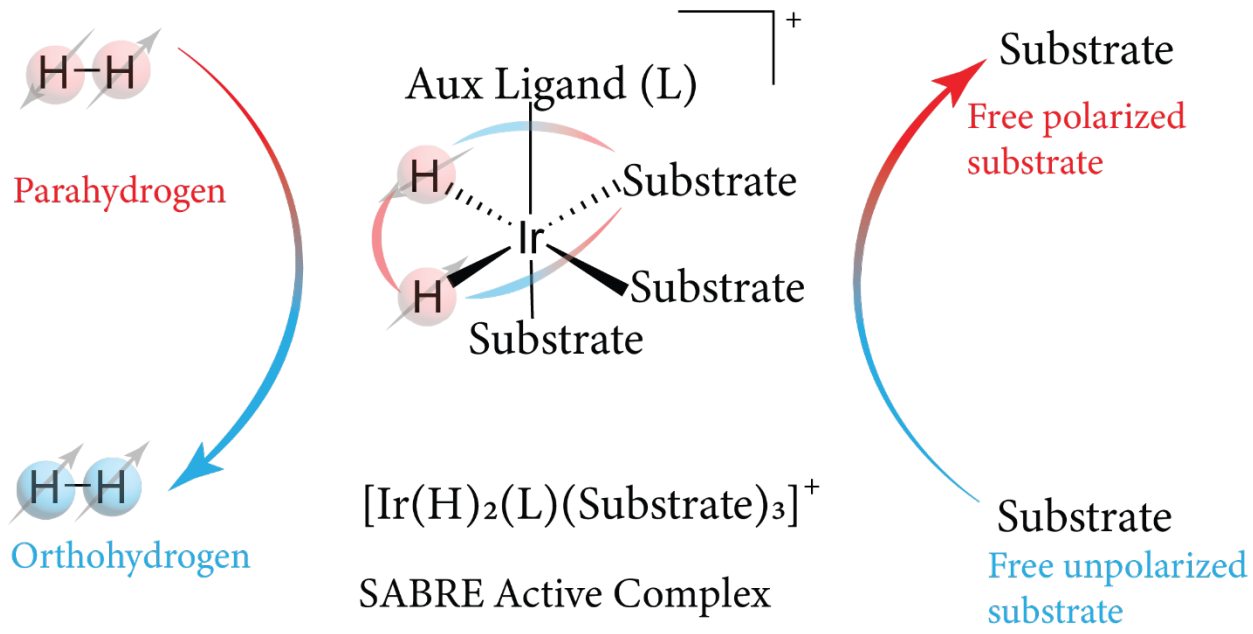

Figure 3.1. A schematic representation of SABRE showing a representative active catalyst, parahydrogen and substrate.

Ducket et al[87] reported the first successful hyperpolarization of the ^{1}H, ^{15}N and ^{13}C nuclei in pyridine via SABRE achieving greater than 100-fold enhancement. Since, SABRE has been used to hyperpolarize nuclei such as ^{13}C[90–97], ^{15}N[98–103], ^{19}F[104,105], ^{31}P[106,107], ^{29}Si[108] and ^{119}Sn[108] in different molecules with varying functionalities.

3.2 Mechanism

Central to SABRE hyperpolarization is the organometallic catalyst that serves as a template for polarization transfer between parahydrogen and the target substrate.[87,109] The active catalyst is generally an octahedral 18-electron complex of the form $[Ir(H)_2(L)(Substrate)_3]X$ shown in **Figure 3.1**, where Iridium is at the middle of complex and bounded equatorially to two hydrides which are trans to two target substrate molecules bounded also to the iridium center. Axially, Iridium is bound to an auxiliary ligand (L) which initially are phosphine based but N-heterocyclic carbenes (NHC) are more routinely used, for reasons that would be discussed later. A third substrate molecule bounds axially to the iridium center trans to the auxiliary ligand (L) to complete the complex. The active catalyst in SABRE is usually air and moisture sensitive, therefore it is usually prepared in situ from a precursor with a labile ligand.[110–113] Such precursor is usually of the form [Ir(L)(COD)Cl] where COD is 1,5-cyclooctadiene. When the solution of the precursor catalyst in a suitable organic solvent is introduced into an atmosphere of hydrogen in the presence of the target substrate, COD undergoes hydrogenation to cyclooctane and becomes irreversibly labile thus opening the coordination site at the iridium center for substrate molecules to bind. This process of forming the 18-electron active complex ($[Ir(H)_2(L)(Substrate)_3]X$) is known as **activation** and is the most significant step in SABRE hyperpolarization process.[110]

To hyperpolarize any substrate via SABRE, it must be able to form a stable active complex of the form above or a variant thereof.

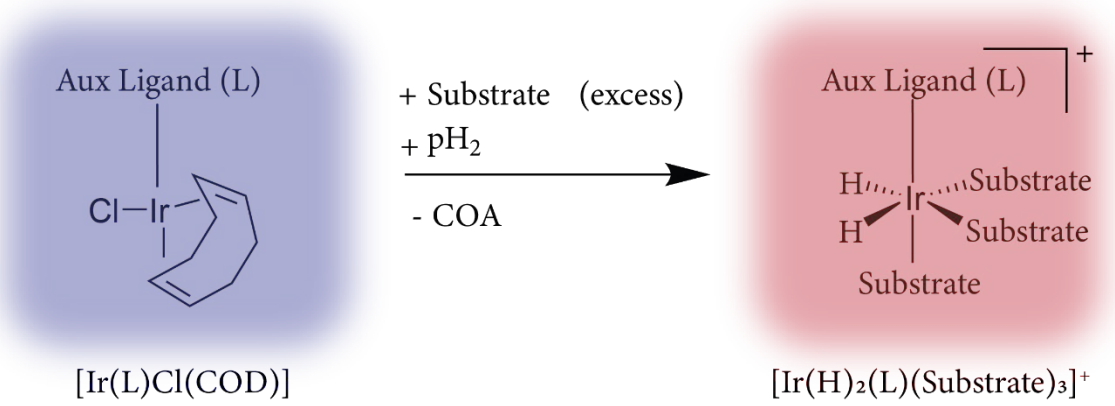

Figure 3.2. Generic reaction scheme showing the formation of the activated SABRE catalyst.

The second important process in SABRE is the reversible binding of parahydrogen and the target substrate. In general, this process involves first the dissociation of a substrate molecule to form a 16-electron square pyramidal complex $[Ir(H)_2(L)(substrate)_2]$. This complex can either isomerize into a trigonal bipyramidal complex or bind directly to a molecule of hydrogen to form a non-classical hydride complex $[Ir(H)_2(\eta\text{-}H_2)(L)(substrate)_2]$. A simultaneous oxidative addition of the fresh parahydrogen molecule and reductive elimination of the initial hydrides allows the constant refreshing of parahydrogen in the complex. Besides hydrogen binding, the free substrates in solution can bind to any of the possible complexes formed after initial ligand dissociation. Studies have shown that both parahydrogen and substrates exchange have a common pathway, and they competitively bind to any of the 16-electron intermediates.[110,112] While it is possible to assume the possibility of hydrogen dissociation from the active 18-electron catalyst ($[Ir(H)_2(L)(Substrate)_3]$), this pathway has been shown to be highly unlikely due to the higher

energy barrier associated with forming complex [Ir(L)(Substrate)$_3$] compared to [Ir(H)$_2$(L)(substrate)$_2$].[110,112,114–116]

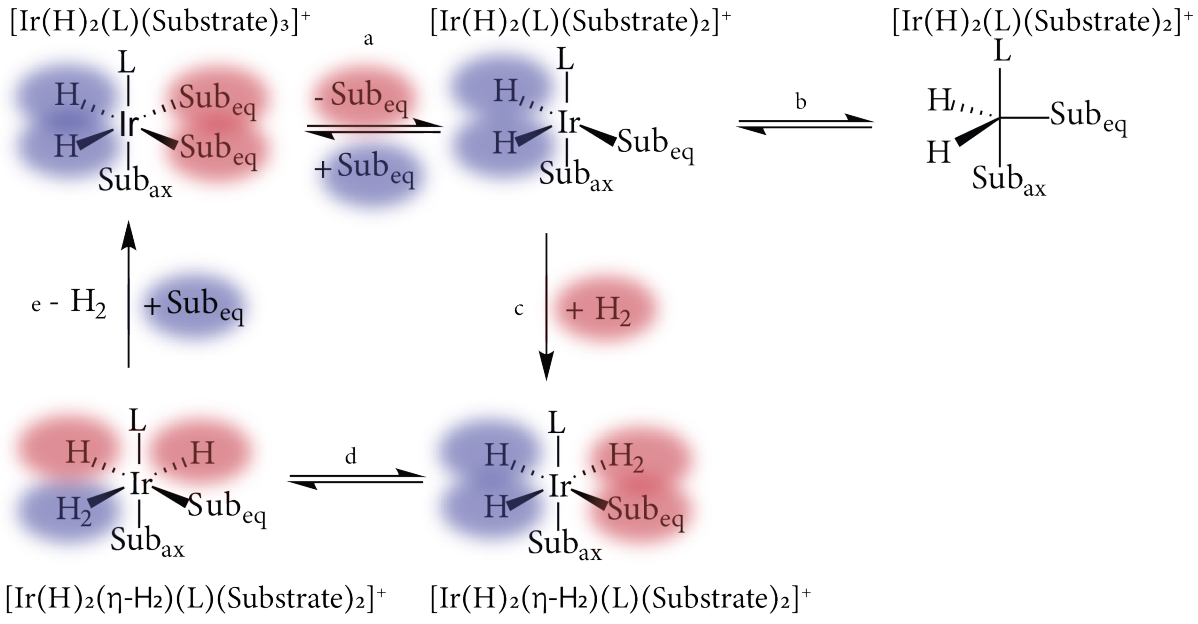

Figure 3.3. SABRE exchange pathway showing [A] the dissociation of an equitorial substrate. [B] isomerization of the 16-electron complex [C] binding of parahydrogen to form a non-classical hydride complex. [D] simultaneous oxidative addition parahydrogen and reductive elimination of orthohydrogen. [E] dissociation of ortho-hydrogen and binding of a new substrate.

The efficiency of SABRE is inevitably linked to the lifetime of the active catalyst complex and therefore substrate dissociation. Very short lifetimes mean there is not enough time for polarization transfer before substrate dissociation. Whereas very long lifetimes enable relaxation of the substrates through either coherent transfer to hydrides or distribution of polarization to other NMR active nuclei on the catalyst which serves as polarization sink.[110,117] Several factors that affect the optimal performance of SABRE are tightly linked to the lifetime of the catalyst as well as ease of substrate dissociation. Identity of auxiliary ligand, temperature, solvent, concentration,

polarization transfer field and secondary co-ligands are factors that can influence the lifetime of the active catalyst and its exchange dynamics.

3.3 Role of Catalyst Identity in SABRE

The identity of the catalyst is majorly dependent on the type of auxiliary ligand (L) that is used. Substrate exchange on the active catalyst complex can be altered significantly through the choice of the auxiliary ligand.[110] The first example of ligand used in SABRE processes are the phosphine-based ligands.[86,87,118] It was quickly discovered that the steric and electronic properties of these ligands play a major role in substrate dissociation.[86]

To understand how the steric and the electronic properties of the ligands affect the overall properties of the catalyst, it is important to examine the parameters used in measuring both properties.

3.3.1 Steric properties of Auxiliary Ligands

The efficiency of a SABRE catalyst is tightly linked to the steric properties or bulkiness of its auxiliary ligand. The bulkiness of a ligand centered on a metal is more commonly measured by its percentage buried volume ($\%V_{Bur}$). This measure proposed by Hillier et al.[119] in 2003 is defined by the percentage of the total volume of a sphere occupied by a ligand. The volume of the sphere represents the space around the metal center that can be possibly occupied by ligands or ligand fragments. Thus, the bulkier the ligand the larger the amount of that sphere occupied by the ligand. The sphere has a defined radius centered around the metal and is usually determined by crystallographic data.[119]

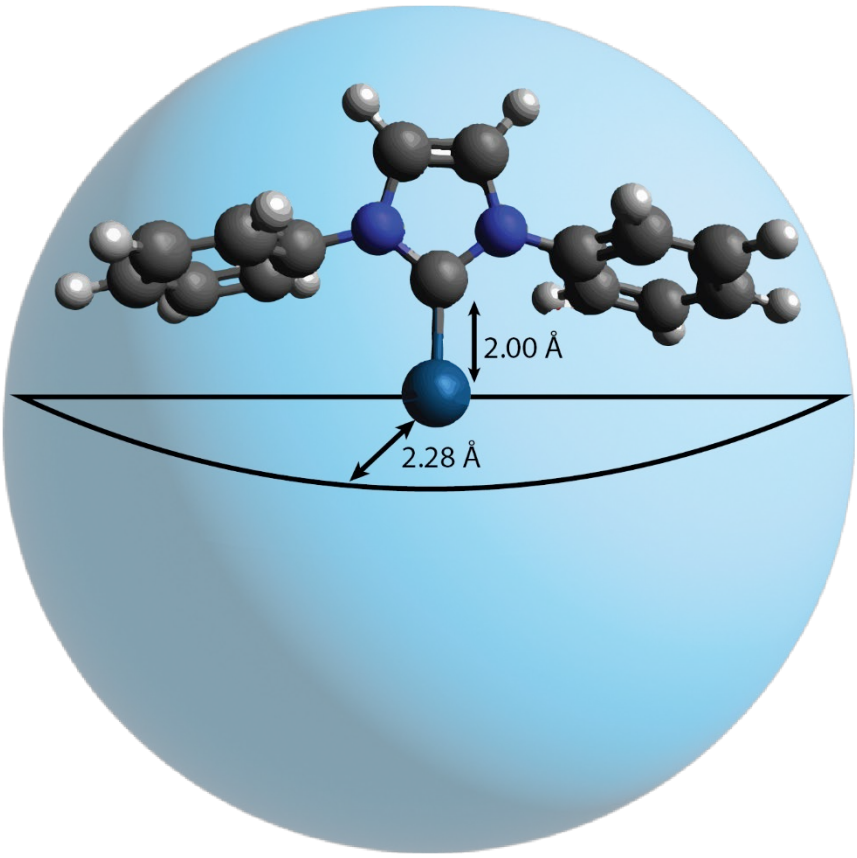

Figure 3.4. Illustration depicting the definition of % buried volume. Using the IMes ligand (1,3-bis(2,4,6-trimethylphenyl)imidazole-ylidene) as an example.

Comparing phosphine and NHC ligands, it was observed that there is little difference between the steric properties of phosphine compared to NHC's. Using a sphere of radius 2.28 Å and a [LAuCl] complex, Cavier and Nolan in a comprehensive review article[120] reported that For L=NHC, The $\%V_{Bur}$ ranges between 20 % for IDM (1,3-dimethylimidazole-y-lidine) to 42 % for SIPr (1,3-bis(2,6-diiso-propylphenyl)-4,5-dihydroimidazole-2-ylidine). Similarly, the $\%V_{Bur}$ for L= phosphine ligands ranges between 22 % for TPA (1,3,5-triaza-7-phosphaadamantane) and 45 % for $PMes_3$ (tris(2,4,6-trimethylphenyl) phosphine). In the context of SABRE, one of the first phosphine-based ligand PCy_3 (tricyclohexylphosphine) has a $\%V_{Bur}$ of 33.4 % while the most used

NHC ligand till date IMes (1,3-Bis(2,4,6-trimethylphenyl)imidazole-ylidene) has a $\%V_{Bur}$ of 31.2 %.

Table 3.1. % Buried volume for selected phosphine and NHC ligands based on [LAuCl] complex[120]

Ligand Structure	IUPAC name and abbreviation	% Buried volume
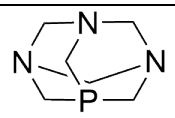	1,3,5-triaza-7-phosphaadamantane (TPA)	22.1
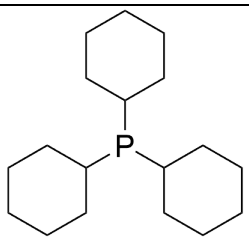	Tricyclohexylphosphine (PCy_3)	33.4
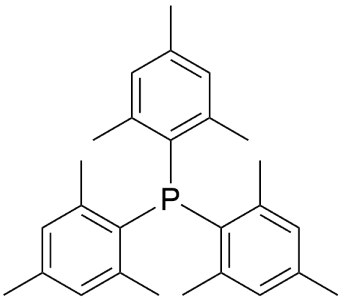	tris(2,4,6-trimethylphenyl) phosphine ($PMes_3$)	45.0
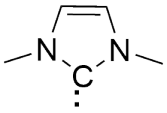	1,3-dimethylimidazole-y-lidine (IDM)	22.7
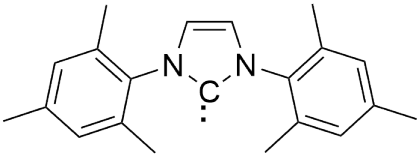	1,3-Bis(2,4,6-trimethylphenyl)imidazole-ylidene (IMes)	31.2

Table 3.1 (Continued)

Ligand Structure	IUPAC name and abbreviation	% Buried volume
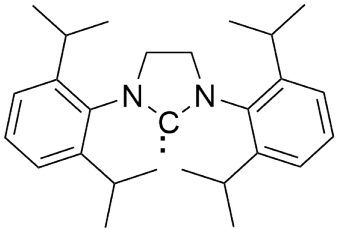	1,3-bis(2,6-diiso-propylphenyl)-4,5-dihydroimidazole-2-ylidine (SIPr)	41.5

3.3.2 Electronic properties of Auxiliary Ligands

The electronic properties of auxiliary ligands used commonly in SABRE catalysis can be measured using the Tolman's electronic parameter (TEP, ν_{co} (A_1)).[121] This measure is based on the effect of the ligands on the frequency of the A_1 carbonyl mode of $Ni(CO_3)L$ complex via infra-red spectroscopy. This method is preferred because it isolates electronic effects from steric. The test complex is also easily formed for any ligand L regardless of its size. Also, the carbonyl A_1 stretching frequency is sharp and well resolved. The higher the electron donating ability of a ligand, the more it facilitates back bonding of the metal to the carbonyl. This results in the elongation of C-O bond which in turn leads to decreased ν_{co} (A_1). In contrast, the less the electron donating properties the higher the ν_{co} (A_1). In general, NHC ligands are excellent electron donators in comparison to their phosphine ligands therefore their TEP are generally lower.[121] The IMes ligand has a TEP of 2050.7 cm^{-1} while PCy_3 has a TEP of 2056.4 cm^{-1} according to literature.[122]

Table 3.2. Tolman electronic properties (TEP) of selected phosphine and NHC ligands in $[Ni(CO)_3(L)]$ complex[122]

Ligand (L)	Solvent	TEP (cm^{-1})
Triphenylphosphine (PPh_3)	$CHCl_3$	2068.9
Diphenylmethylphosphine ($PMePh_2$)	$CHCl_3$	2067.0
Tricyclohexylphosphine (PCy_3)	CH_2Cl_2	2056.4
1,3-bis(2,6-diiso-propylphenyl)-4,5-dihydroimidazole-2-ylidine (SIPr)	CH_2Cl_2	2052.2
1,3-bis(2,6-diiso-propylphenyl)imidazole-2-ylidine (IPr)	CH_2Cl_2	2051.5
1,3-Bis(2,4,6-trimethylphenyl)-4,5-dihydroimidazole-ylidene (IMes)	CH_2Cl_2	2051.5
1,3-Bis(2,4,6-trimethylphenyl)imidazole-ylidene (IMes)	CH_2Cl_2	2050.7

3.3.3 Effect of stereo-electronic properties of Auxiliary Ligands on Substrate Dissociation

Studies have shown that sterically large electron rich ligands favor substrate dissociation and thus facilitates the reversible exchange necessary to build up polarization in SABRE. In 2009, Ducket et al. compared a series of phosphine-based ligands (PCy_3, PCy_2Ph, $PCyPh_2$, PEt_3, P^iPr_3, P^nBu_3, P^tBu_3, and P(1-naphthyl)$_3$ for their effect on the polarization of the ortho, meta and para protons of pyridine. They observed that the electron rich and sterically demanding phosphine (PCy_2Ph) was the most efficient in achieving polarization transfer to pyridine.[86]

Furthermore, it was discovered that the use of N-heterocyclic carbene ligands (NHC) as opposed to phosphines could significantly improve signal enhancements in SABRE as they typically have lower TEP values compared to their phosphine counterparts.[116,122] The improved enhancements can be explained in terms of optimized substrate exchange in the SABRE catalytic cycle. In 2011, Cowley et. al. achieved an 8100-fold ^{1}H NMR signal enhancement for pyridine in methanol-d_4 using an $[Ir(H)_2(IMes)(Py)_3]Cl$ active catalyst which is *ca.* > 80 times higher than the enhancements achieved using $[Ir(H)_2(PCy_3)(Py)_3]BF_4$. This significant enhancement was attributed to the faster rate of pyridine dissociation in $[Ir(H)_2(IMes)(Py)_3]Cl$ which was measured to be 23 s^{-1}, *ca.* > 50 times faster than the rate of pyridine dissociation in $[Ir(H)_2(PCy_3)(Py)_3]BF_4$.[116]

This development marked a significant turning point in SABRE catalysis as NHC carbenes are not just better compared to phosphines, they are also easily modified sterically and electronically. Thus, a wide range of SABRE catalysts with different NHC ligands have been reported and their effect on SABRE efficiency has been described. Evidently, it is the NHC carbenes based on the IMes ligand that has shown great SABRE efficiency.[116,118,123–128]

In a systematic study,[126] A library of 22 iridium NHC catalysts where the substituent on the IMes ligand were altered on the aryl arm and the imidazole backbone. It was observed that

introducing bulky groups in the ortho position of the aryl group increased substrate dissociation rates, while altering substituents in the para position and the imidazole backbone significantly affects the electronic properties and SABRE efficiency. Electron donating groups tend to increase the rate of dissociation while electron withdrawing groups such as halogens tend to decrease rate of dissociation. The most significant electronic effects were observed with substitution on the imidazole backbone of the IMes ligand. Addition of methyl or other electron donating groups tends to significantly improve the rate of pyridine dissociation while electron withdrawing groups does the opposite.

In contrast to previous studies with phosphine ligands, electron deficient NHC's were shown to give higher polarization values when a pyridine derivative (methyl-2,5-d_2-nicotinate) is used as the substrate. This is because the substrate dissociation rate in these catalysts is closer to the frequency at which polarization is transferred (ω_{LAC}) (see **Figure 3.5**). Thus, while NHC's are more electron donating compared to phosphine ligands, favoring fast substrate dissociation, they can be fine-tuned by introducing electron deficient groups to achieve optimal performance. This is especially true, as different substrates would have different spin-coupling interactions and require slightly faster or slower dissociation from the catalyst.[126]

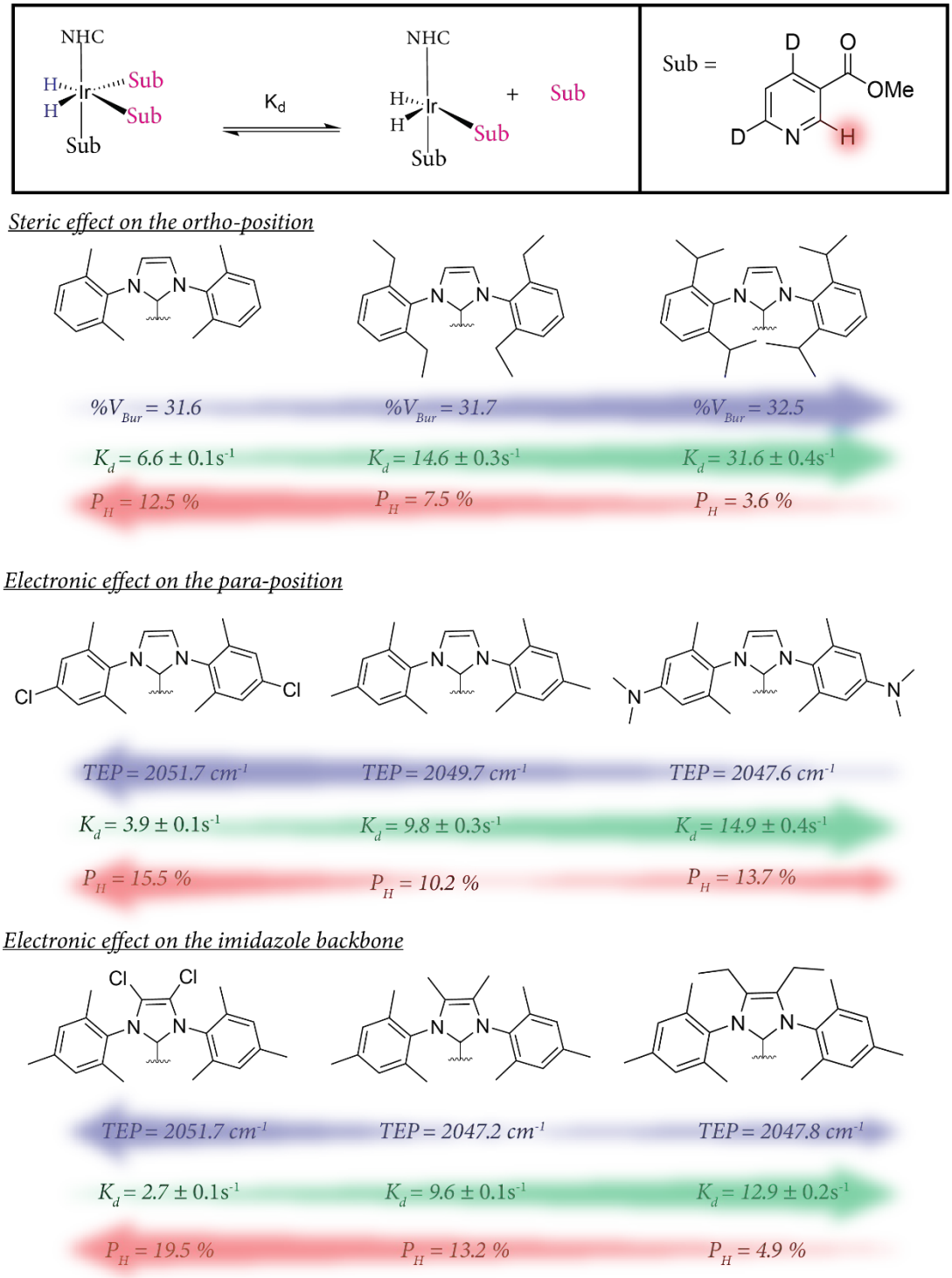

Figure 3.5. Steric and electronic effect of auxiliary ligand based on Ir-IMes on the polarization of 4,6-d_2-methylnicotinate

3.4 Role of Co-Ligand

Not all substrates can bind to the Iridium center to form an active magnetization catalyst such as the form $[Ir(H)_2(L)(Substrate)_3]X$. Bulky substrates such as ortho substituted pyridine derivatives[129–132] and bidentate substrates such as alpha-keto acids[90,95,97,133–137] are among such examples. Using Co-Ligands like pyridine, sulfoxides,[137–139] nitriles[132,140,141] and amines,[142,143] It is possible to form an active magnetization catalyst of the form $[Ir(H)_2(L)(Substrate)_2(Co\text{-}L)]X$ or $[Ir(H)_2(L)(Substrate)(Co\text{-}L)_2]X$ for monodentate substrate or $[Ir(H)_2(L)(Substrate)(Co\text{-}L)]X$ for bidentate substrates. The addition of co-ligand presents another layer of complexity to the chemical species in a SABRE system. Nevertheless, they have proven very effective in achieving polarization transfer in substrates that are otherwise unamenable to SABRE or increasing the efficiency of polarization in samples that bind poorly to the SABRE catalyst.[110]

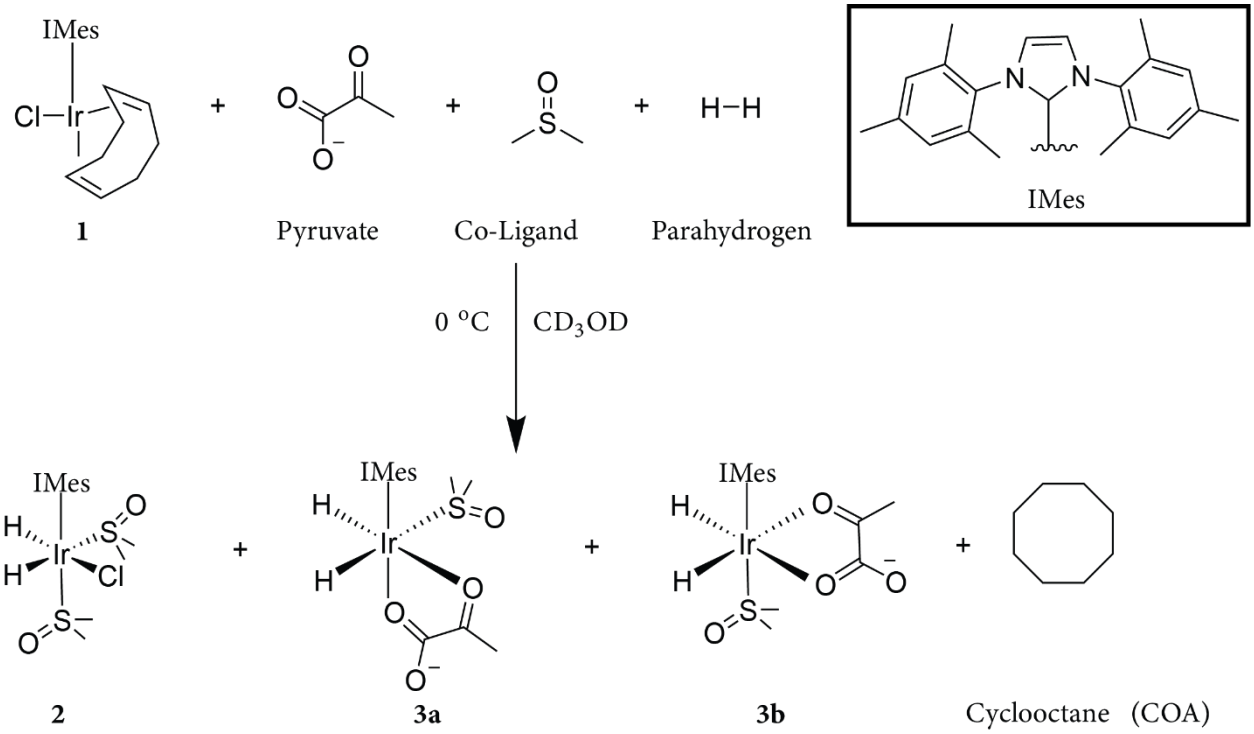

Figure 3.6. Formation of activated SABRE catalyst using DMSO as a co-ligand for pyruvate hyperpolarization.

A good example of the importance of co-ligand is in the hyperpolarization of pyruvate, an important biomarker for cancer diagnosis. Pyruvate being an alpha-keto acid is an *O*-donor (binds to the iridium center through the lone pairs on an oxygen atom) and bidentate (2 binding sites). Thus, it is unable to form a SABRE active catalyst by itself. However, with the help of sulfoxide ligands such as DMSO, it was able to form two active catalysts (**3a** and **3b** in **Figure 3.6**) of the form $[Ir(H)_2(IMes)(\eta^2\text{-pyruvate})\ (DMSO)]X$. In catalyst **3a** the two pyruvate binding sites is equatorial and trans to the hydride ligands and the DMSO ligand occupies the axial position. In **3b**, one of the two binding sites of pyruvate occurs axially while the other equatorial site is occupied by DMSO. Aside from these two active species, there is a third active species (catalyst **2**) of the form $[Ir(H)_2(IMes)(Cl)\ (DMSO)_2]$. This complex is believed to help in improving hydrogen exchange in the catalytic cycle.[133–135,139]

The successful use of a co-ligand to enable ^{13}C pyruvate polarization via SABRE marks an important milestone in the application of SABRE for biomedical applications. Further optimization of this work led to achieving 1.7% polarization on [1-^{13}C] Pyruvate.[95,133,134] In 2021, we published an article, that shows 10 % polarization on [1-^{13}C] Pyruvate by careful optimization of temperature and sample composition.[90] Recently, up to 17% polarization has been reported with efficient purification steps, retaining up to 74 % of the initial polarization, to achieve biocompatible hyperpolarized pyruvate solutions. Such solution was used for in vivo spectroscopy and imaging for metabolic tracking in a hepatocellular carcinoma (HCC) tumor.[144]

The use of co-ligand has been extended to other alpha-ketoacids with biomedical relevance. Isaiah et al[97] recently hyperpolarized alpha-ketoglutarate, a Tricarboxylic cycle intermediate and obtained ~ 9% 1-^{13}C polarization level in 1 minute. Similarly, Stephen et al[145] hyperpolarized

several alpha-keto acids and reported extensive information about their exchange dynamics and binding patterns. In chapter 4 of this document, I report on the use of DMSO as a co-ligand to hyperpolarize a novel MRI pH sensor with an alpha-keto acid moiety, Z-4-oxo-2-methylpent-2-ene-dioic acid (Z-OMPD).

Furthermore, the effect of co-ligand on the hyperpolarization of ^{15}N sodium nitrite was recently investigated.[146] In contrast to pyruvate, the nitrite ion is an *N*-donor (binds to the iridium center through the lone pairs on a nitrogen atom) and monodentate so it forms two active magnetization catalysts, $[Ir(H)_2(IMes)(NO_2)_2(Co\text{-}L)]X$ (**4**) and $[Ir(H)_2(IMes)(NO_2)(Co\text{-}L)_2]X$.(**5**) as shown in **Figure 3.7**. The latter was observed to be the most stable catalyst and promotes efficient polarization transfer. It was shown that the higher the ratio of the latter, the higher the polarization achieved on nitrite. In this study, DMAP (*N*,N-dimethylaminopyridine) was reported to give the highest polarization among other co-ligands used. Interestingly, in terms of catalyst identity, the more sterically hindered catalyst $[Ir(H)_2(IPr)(NO_2)(Co\text{-}L)_2]X$. gives the highest level of polarization. Here it seems the polarization build up on nitrite is very fast thus requires a catalyst with very fast substrate dissociation rate. In chapter 6 of this document, I report on the use of hyperpolarized nitrite for reaction monitoring.

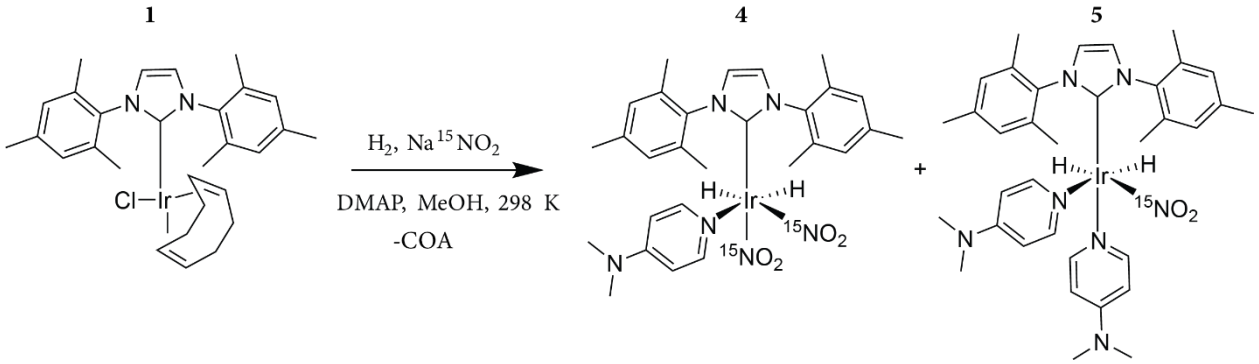

Figure 3.7. Formation of the active SABRE catalyst in the hyperpolarization of nitrite ion using DMAP as co-ligand

3.5 Role of Solvent

SABRE has been most effective in organic solvents such as methanol, ethanol, chloroform and dichloromethane.[147–149] The need to prepare hyperpolarized contrast agents that can be injected into patients for imaging studies has led to the investigation of water as solvent. The main limitation to this approach is that the catalyst precursor is not water soluble and likewise hydrogen being a non-polar gas has limited solubility in water. Designing a water-soluble catalyst precursor has been identified as a viable method to tackle this challenge.[150–153] Chapter 5 of this document will be dedicated to this approach. Other approaches include extraction of the HP substrate into aqueous solution,[144,154] evaporation of organic solvent after activation and introducing water,[155] and the use of heterogeneous catalysts that can be easily filtered off. The later method has been used to hyperpolarize water itself, albeit very low levels of polarization.[156]

3.6 Polarization transfer in SABRE and the role of level anti-crossing

The pure singlet state order in parahydrogen can be transferred to a target substrate spontaneously or driven by RF pulses. Spontaneous transfer occurs when both parahydrogen and substrate are bound to the catalyst such that the symmetry of the nascent parahydrogen-derived hydride is broken. Symmetry can be broken through chemical shift difference (chemical inequivalence) of the hydrides or through difference in their J-coupling pattern (magnetic inequivalence). When SABRE is done at low field, the chemical shift difference is small. Thus the J-coupling of the hydrides to the target substrates has to be different for efficient spin order transfer (SOT). This requirement is usually fulfilled in SABRE complexes as shown in **Figure 3.8**

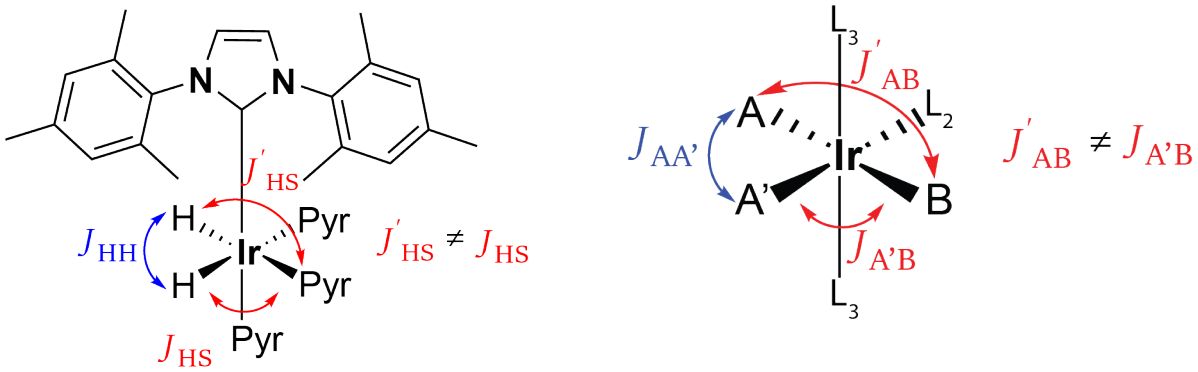

Figure 3.8. A typical active SABRE complex showing the difference in cis and trans J-coupling of the hydrides to the target substrate

The spontaneous SOT in SABRE have been explained by Ivanov et al. via the Level Anti-Crossing (LAC) theory. LAC can be pictured, as shown in **Figure 3.9**, by considering two states |A⟩ and |B⟩ of different energy levels where |B⟩ is higher than |A⟩. Assuming these two states can be perturbed by certain parameters (e.g Magnetic Field, B0) such that |B⟩ is lowered based on B0 and |A⟩ vice versa. At certain values of B0, the two states are expected to cross, however, if they are coupled, they would never meet, instead they would tend to avoid each other at the level where they are expected to cross, this encounter is termed LAC.

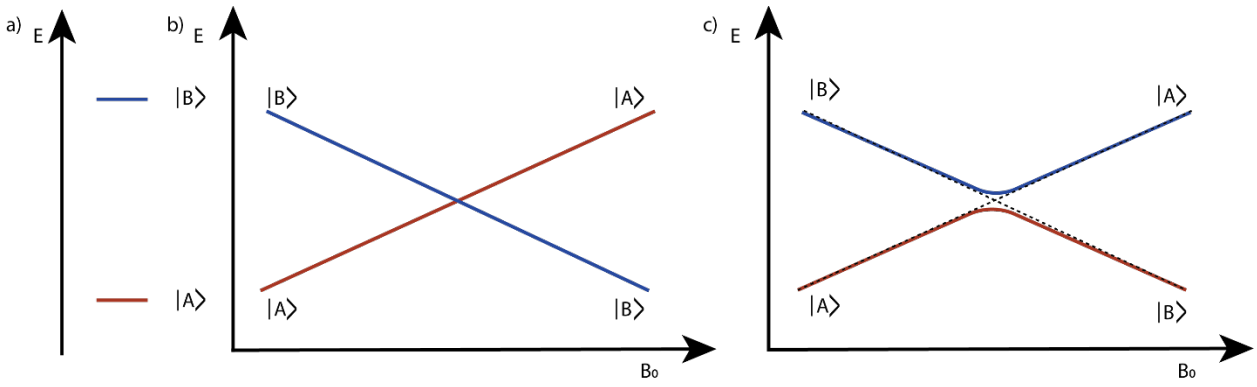

Figure 3.9. An illustration of level anti-crossing a) two states A and B with different energy level b) perturbated by B_0 and crosses each other if they are uncoupled c) exhibit a level anti-crossing if A and B is coupled.

At the LAC, the two states can transfer population or mix, the efficiency of this mixing or transfer Q, is dependent on the strength of the *J*-coupling and the rate of change of the precision frequencies of the spins according to equation 3.1.[157]

$$Q_{A,B} = exp\left(-\frac{(2\pi J)^2}{\partial(\delta\nu)/\partial t}\right) \qquad \text{Eq 3.1}$$

Furthermore, it is quite helpful to picture LAC from a SABRE perspective, considering **Figure 3.8**, notice two hydrides occupy the equatorial plane and two pyridines are opposite in the same plane. For simplicity, let's consider one of the pyridines and note that both hydrides are coupled with the ortho protons of pyridine. This gives a classical AA'B system where A and A' represents the hydrides formed from parahydrogen and B is the ortho protons of pyridine.

It is safe to assume that the hydride spins are strongly coupled ($J_{AA'} \gg J_{AB}, J_{A'B}$) relative to spin B so can be expressed in the singlet-triplet basis while B can be treated in the Zeeman basis (α or β). Therefore, we arrive at 8 possible spin states for the AA'B system:

$$\begin{array}{ll} |S_0\alpha\rangle & |S_0\beta\rangle \\ |T_0\alpha\rangle & |T_0\beta\rangle \\ |T_+\alpha\rangle & |T_+\beta\rangle \\ |T_-\alpha\rangle & |T_-\beta\rangle \end{array}$$

The initial state of the system will be the $|S_0\alpha\rangle$ and $|S_0\beta\rangle$ states since the hydrides are derived from parahydrogen. due to quantum selection rules only states that have the same total symmetry can efficiently mix, therefore, the only transitions that is allowed are $|S_0\alpha\rangle$ to $|T_+\beta\rangle$ or $|S_0\beta\rangle$ to $|T\_\alpha\rangle$. These two transitions have an LAC that depends on the sign and magnitude of the J-coupling between the two hydrides and their chemical shift difference relative to the substrate proton according to equation 3.2.

$$|\nu_A - \nu_B| = |J_{AA'}|$$

Eq 3.2

The field at which this LAC occurs can be computed from the above equation using:

$$\nu_i = \gamma_i(1 - \delta_i)B/2\pi$$

Eq 3.3

Where ν_i, γ_i, and δ_i are the Larmor frequency, gyromagnetic ratio and chemical shift of ith nuclei respectively, therefore:

$$B_{LAC} = \frac{2\pi|J_{AA'}|}{\gamma|\delta_A - \delta_B|}$$

Eq 3.4

For transferring polarization to the proton of a target substrate the difference in chemical shift (Δδ) is small, therefore B_{LAC} or the Polarization transfer field (PTF) is in the orders of milli-Tesla (mT). To transfer polarization to heteronuclei such as ^{13}C and ^{15}N, the large difference in gyromagnetic ratio of the target nuclei and the parahydrogen derived hydrides makes B_{LAC} very small and ranges in the micro-Tesla (μT) field. The earth's magnetic field is 4 orders of magnitude larger than a typical μT field, therefore a mu-metal shield is generally employed to screen it from the earths field in order to transfer magnetization to heteronuclear targets. This method of polarization transfer is termed SABRE-SHEAT (SABRE in SHield Enables Alignment Transfer to Heteronuclei).[158,159]

Chapter 4 : SABRE-SHEATH Hyperpolarization of [1,5-$^{13}C_2$]Z-OMPD for Non-invasive pH sensing.

From:

Mustapha B., Abdulmojeed, et al. "SABRE-SHEATH Hyperpolarization of [1,5-$^{13}C_2$]Z OMPD for Non-invasive pH sensing." ACS Sens. 2024, 9, 12, 6372–6381.

Abstract: Hyperpolarized (HP) ^{13}C-labelled probes are emerging as promising agents to non-invasively image pH in vivo. HP [1,5-$^{13}C_2$]Z-OMPD (Z-4-methyl-2-oxopent-3-enedioic acid) in particular, has recently been used to simultaneously report on kidney perfusion, filtration and pH homeostasis, in addition HP Z-OMPD has the ability to detect local tumor acidification. In previous studies, dynamic nuclear polarization(d-DNP) was used to hyperpolarize Z-OMPD. Here, we pioneered the hyperpolarization of [1,5-$^{13}C_2$]Z-OMPD via SABRE-SHEATH (Signal Amplification By Reversible Exchange Shield Enabling Alignment to Heteronuclei), which is relatively simple, fast, and promises to be highly scalable. With SA-BRE-SHEATH we achieve enhancement values of ~3950 and ~2400 at 1.1 T (P_{13C} = 0.4 % and 0.25 %) on the labelled C-1 and C-5 positions of Z-OMPD. Density functional theory (DFT) calculations at the B3LYP level of theory were used to investigate possible binding modes of Z-OMPD on the iridium-based polarization transfer catalyst. The experimental and theoretical results suggest that the equatorial binding mode to the catalyst, where Z-OMPD binds to the catalyst at both C-1 and C-5 carboxylate positions, is the most stable complex. The HP signals were used to measure Z-OMPD chemical shift as a function of pH showing ~3 ppm shift across pH 4-7. This work lays a foundation for the development of a simple, low-cost hyperpolarization technique to image pH.

Chapter 4: Preface

The material introduced in this chapter is a previously published work in ACS Sensors. The work lays the foundation for deployment of SABRE technique in the hyperpolarization of Z-4-methyl-2-oxopent-3-enedioic acid (Z-OMPD) for extracellular pH sensing. In this work, all experiments were completed by Mustapha Abdulmojeed, Erica Curran and Atli Davidsson; Computational work was done by Seth Dilday and Mustapha Abdulmojeed; pure doubly labelled [1,5-$^{13}C_2$] Z-OMPD was synthesized by Pascal Wodtke; Results were analyzed by Mustapha Abdulmojeed, Martin Grashei, Franz Schilling and Thomas Theis; the manuscript was written by Mustapha Abdulmojeed and Thomas Theis; and the manuscript was edited by Mustapha Abdulmojeed, Martin Grashei, Stephen McBride, Austin Browning, Keilian MacCulloch, Patrick TomHon, Andreas B. Schmidt, Eduard Y. Chekmenev, Franz Schilling and Thomas Theis.

4.1 Introduction

Extracellular pH is a tissue characteristics which is altered in multiple pathological states such as in cancer,[160–166] ischemia,[167–169] chronic obstructive pulmonary disease,[170] and renal tubular acidosis.[169,171] Here, acidification is not only a disease hallmark, but also has a significant impact on treatment outcome, e.g., of tumors.[172] Modern treatments, such chemotherapeutics[173] or engineered T cells,[174] are highly susceptible to the pH of the target tissue. It has been shown that treatment efficacy can be enhanced, when pH-conditioning adjuvant therapies are employed prior to the main therapy.[175–178] In order to timely adjust these treatment steps, non-invasive monitoring of the tissue pH is key. Magnetic resonance (MR) methods can provide accurate and precise non-invasive measurement of pH in vivo with reasonable spatial resolution.[179–183] A promising MR-based method takes advantage of changes in chemical shifts due to changes in the local electronic environment, induced by pH-driven proton exchange. An ideal MR pH sensor should have the

following properties: (1) large pH sensitivity, (2) a pKa in the physiological range, (3) no toxicity at concentrations obtained in vivo after injection, (4) metabolic stability, and (5) high sensitivity (high signal-to-noise ratio).[184] Common MR pH sensors such as 3-aminopropylphosphonate (3-APP),[185] and 2-imidazole-1-yl-3-ethoxycarbonylpropionic acid (IEPA)[186] satisfy most of these conditions but are limited due to low sensitivity and overlapping background signals.[185–188] The challenge of background signals can be mitigated using carbon-13 labeled MR pH sensors. Unfortunately, ^{13}C nuclei have low natural abundance (1.1 %) and low gyromagnetic ratio (four times lower than ^{1}H). Additionally, MR methods are generally less sensitive compared to other techniques such as optical and electrochemical methods. This low sensitivity is due to the intrinsically low net magnetization of the nuclear spins even at high magnetic field.[189,190] The sensitivity issue can be tackled by using isotopically enriched ^{13}C pH sensors in combination with hyperpolarization, which increases the net magnetization of the spins by several orders of magnitude.[191–194]

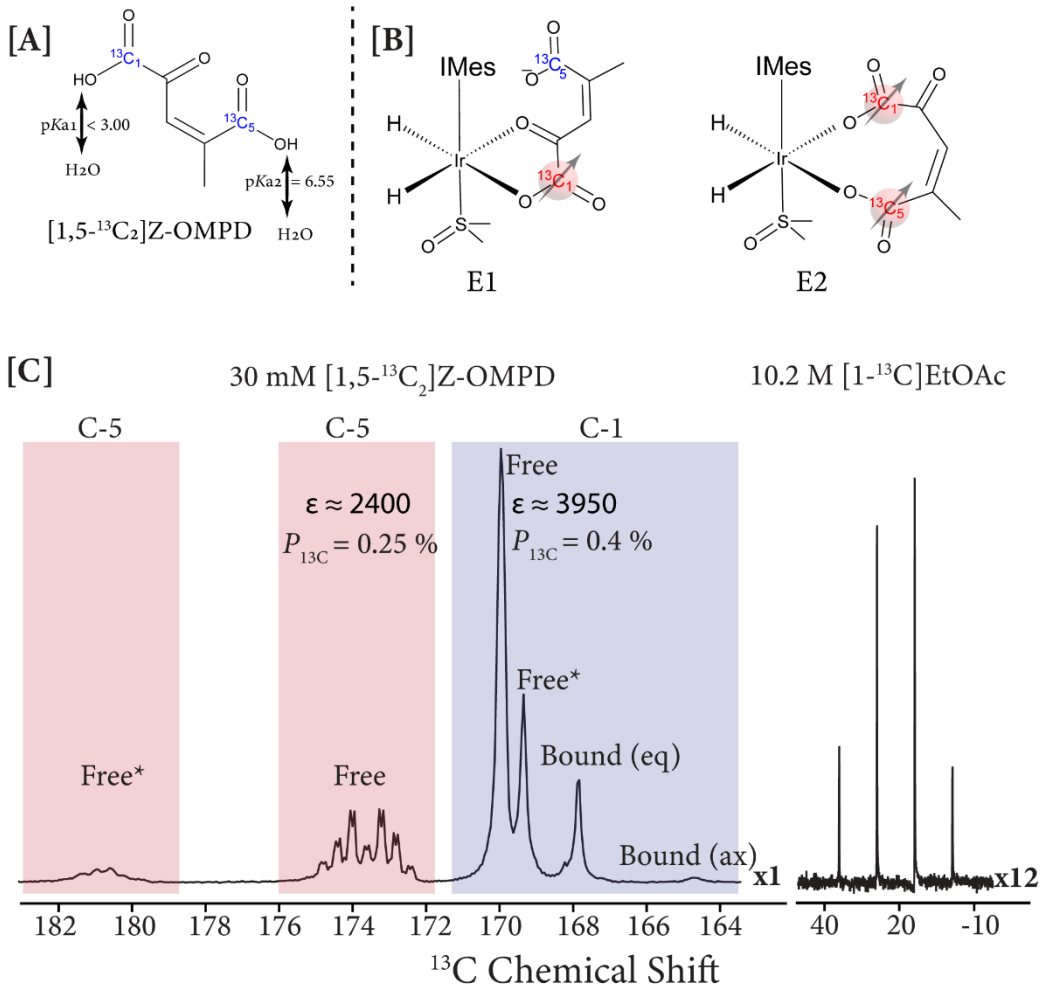

Figure 4.1. [A] 2D structure of Z-OMPD indicating the labelling of the hyperpolarized carbons. [B] Dominant binding modes of Z-OMPD to Ir-IMes catalyst. In E1, Z-OMPD binds equatorially via oxo groups at C-1 and C-2 (**E1**). In E2, Z-OMPD binds via the oxo groups at C-1 and C-5 (**E2**) [C] LEFT: ^{13}C NMR spectra of hyperpolarized [1,5-^{13}C$_2$] Z-OMPD peaks showing both Free C-1 and C-5 peaks and equatorial and axial bound C-1 peaks (peaks in asterisk are not fully identified). RIGHT: ^{13}C NMR spectrum of thermally polarized 10.2 M [1-^{13}C]ethyl acetate. Both spectra were detected at 1.1 T benchtop NMR spectrometer (Spinsolve Carbon, Magritek). The enhancements, ε, are relative to thermal measurements at 1.1 T.

[1,5-$^{13}C_2$] Z-OMPD, hereafter referred to as Z-OMPD, has been introduced as a promising HP MR-based pH probe as its C-1 and C-5 chemical shifts have strong sensitivity to pH.[195] Furthermore, Z-OMPD (structure shown in **Figure 4.1A**) appears to be non-toxic and metabolically stable. The p*K*a of the C-5 carboxylate is 6.55 (in water), which is in the physiological range, thereby making it a well-suited MR pH sensor. In addition, both labels exhibited long T1 in vivo (~30 s at 7 T) and the C-1 resonance serves as an internal chemical shift reference for pH determination. Recent work used Z-OMPD hyperpolarized with dissolution Dynamic Nuclear Polarization (d-DNP) to measure extracellular pH and perfusion. That previous study provided multiparametric fingerprints of renal disease and allowed detection of local tumor acidification for the present contribution, we show for the first time that Signal Amplification by Reversible Exchange in SHield Enabling Alignment Transfer to Heteronuclei (SABRE-SHEATH)[158,196] can hyperpolarize [1,5-$^{13}C_2$] Z-OMPD, as illustrated in **Figure. 4.1**.

Signal amplification by reversible exchange (SABRE) is a parahydrogen-based HP method that relies on the reversible exchange of parahydrogen and a target substrate[87] on an organometallic catalyst ([Ir(H_2)(IMes)(Substrate)$_3$]).[116] Polarization transfer from parahydrogen to the target nuclei is achieved when the frequency differences between source and target nuclei match the spin-spin J-coupling interaction between the parahydrogen derived hydrides on the catalyst and the nuclei of the target substrate.[157,158,196] Accordingly, polarization transfer to heteronuclei such as ^{13}C, ^{15}N and ^{31}P is best accomplished at microtesla fields.[159,197,198] To establish microtesla fields we use mu-metal to shield the system from the earth's magnetic field. This SABRE-SHEATH approach allows the polarization of a wide range of biologically relevant molecules and directly hyperpolarizes the long-lived heteronuclear sites, associated with long T_1, enabling longer

metabolic tracking. Though SABRE-SHEATH is slightly more limited in terms of substrate scope, and achieving high polarization levels requires more optimization, when compared to more widely used d-DNP methods, the technology package required for SABRE-SHEATH is compact, fast, and easy to set up in contrast to other hyperpolarization methods.[87,89,117,199,200] In recent years, the hyperpolarization of the central HP MRI agent, pyruvate, by SABRE has also attracted significant attention.[41,42,82]

Here, we demonstrate the use of SABRE-SHEATH to hyperpolarize both the C-1 and C-5 resonances of the pH sensing molecule [1,5-$^{13}C_2$] Z-OMPD. We find that multiple binding modes are responsible for polarization transfer (**Figure. 4.1B**) detailed in our Results and Discussion. This work highlights the versatility of SABRE-SHEATH in polarizing multiple nuclei in one molecule simultaneously (**Figure. 4.1C**), showing enhancements of >2,000 fold over thermal reference measurements at 1.1 T (P_{13C} > 0.25%). Even though this polarization does not reach levels favorable for in vivo application (> 10 %), further optimization is likely to significantly improve hyperpolarization levels in the future. One example is the use of SLIC-SABRE,[96,201,202] which in some cases outperforms SABRE-SHEATH. In this work, we also used ab initio Density Functional Theory (DFT) calculations to examine the binding mechanisms of Z OMPD to the catalyst, rationalizing experimental observations. Finally, we experimentally verify the pH sensing ability of SABRE-HP Z OMPD by measuring the chemical shifts of C-1 and C-5 as a function of pH across the physiological pH range.

4.2 Materials and Methods

Standard SABRE pre-catalyst [Ir(IMes)(COD)Cl] (IMes = 1,3 bis(2,4,6-trimethylphenyl)imidazole-2-ylidene, COD=cyclooctadiene) was synthesized according to

previously established procedures.[116] Z-OMPD was synthesized by aldol reaction of [1-^{13}C]ethyl pyruvate in a methanolic sodium hydroxide solution followed by acid hydrolysis and prep-HPLC purification as reported by Grashei et al.[195,203] CD_3OD was purchased from Cambridge Isotopes Laboratories, Inc., degassed with three freeze pump thaw cycles, and stored under argon. All other chemicals were purchased from Millipore Sigma and used without further purification.

Each experiment in this manuscript was conducted with a standard sample of 0.7 mL methanol solution containing 6 mM pre-catalyst ([Ir(IMes)(COD)Cl]), 20 mM DMSO, and 30 mM Z-OMPD adjusted to pH 8.42 by adding up to 35 mM solution of NaOD in D_2O as measured with a pH meter (pH measurements were performed using a SevenDirect SD23 pH/conductivity meter with InLab Micro ProISM (51344163)). This solution was degassed with argon before transfer to a 5mm medium-walled NMR tube fitted with a 1/4" outer-diameter (OD) Teflon tube extension and connected to a parahydrogen (parahydrogen) bubbling set up through a Wye 1/8" to 1/4" push to connect as described previously.[91]

The sample was activated for 10 minutes at 0 ºC by bubbling ~98 % parahydrogen at 100 psi. For each experiment, the temperature cycling method was adopted.[90] The solution is first pre-cooled to 0 ºC for a minute, placed in a polarization transfer field (PTF) of 0.4 μT and bubbled at room temperature (~20 °C) with a flow rate of 120 sccm. After 30 s, the bubbling was stopped, and the sample was quickly transported (2-3 s) to a 1.1 T benchtop spectrometer (Spinsolve Carbon, Magritek) for detection. All experiments were carried out with this protocol except when stated otherwise. The ^{13}C polarization (P_{13C}) was calculated using a thermally polarized sample of neat (~10.2 M) [1-^{13}C] ethylacetate as a reference (see SI).

All DFT calculations of the SABRE complexes were conducted using Gaussian 16 package[204] installed on the NCSU high performance computer. DFT geometry optimization was

performed at the B3LYP[205–208] level of theory with a D3 dispersion correction, and 6 311g (d) basis set for C, O, N and S atoms. Iridium was modelled with the Stuttgart-Dresden effective core potential and its associated basis from the GENECP key word within Gaussian with an f-polarization function derived from Ehlers et al.[209,210]

4.3 Results and Discussions

In the experiments presented we employed the temperature cycling procedure described above. The underlying principle of this approach is to allow maximum initial polarization buildup on the catalyst bound substrate by taking advantage of the relatively slow exchange of Z-OMPD compared to the hydrides at low temperature (0 °C. Bubbling at room temperature (20 °C) allows the gradual release of the bound species into its free form as the temperature of the sample slowly increases. **Figure. 4.1C** shows a spectrum of HP Z-OMPD obtained using this approach. C-1 (~170 ppm) and C-5 (175 ppm) show enhancements (ε) of ~3950 and ~2400, respectively, corresponding to P_{13C} of 0.4 % for C-1 and 0.25 % for C-5. The splitting on the C-5 peaks is because of coupling to nearby protons. The observed splitting could be removed either through decoupling or deuteration. (For pH sensing presented below we used decoupling.) The peaks marked with asterisks are not fully identified. We believe that they correspond to a free Z-OMPD variant in solution because the temperature dependent data shows increasing intensity of these peaks with increasing temperature. (**Figure 4.7**)

As illustrated in **Figure 4.2A**, Z-OMPD has an alpha-keto acid functional moiety and could be expected to exhibit similar SABRE chemistry as pyruvate, a well-studied alpha-keto carboxylate substrate in SABRE hyperpolarization.[90,95,96,133,134,211] Based on the known pyruvate binding modes, we first expected that, upon activation of the pre-catalyst in the presence of DMSO, Z-OMPD and parahydrogen, at least two activated SABRE complexes are formed.[133] The first

complex is the equatorial complex E1 (**Figure 4.2A**) in which Z-OMPD coordinates equatorially to the iridium center through the carboxylate and keto groups in positions 1 and 2, respectively.

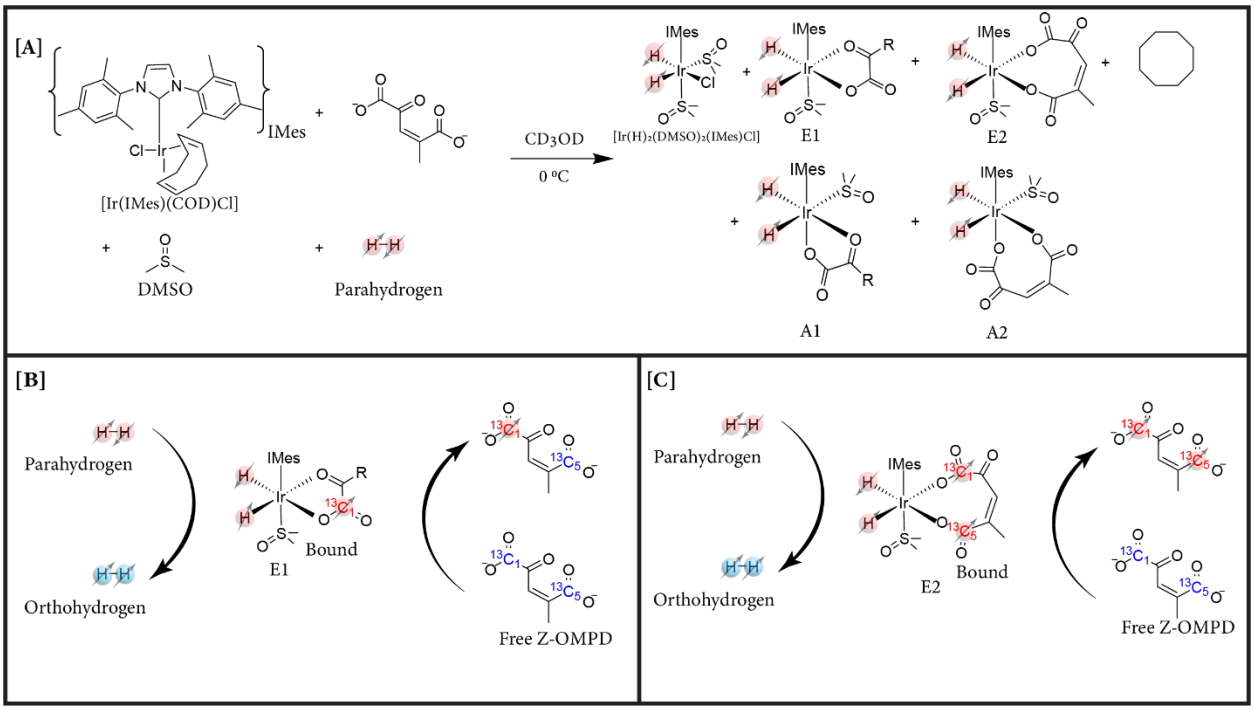

Figure 4.2. [A] Activation of [Ir(IMes)(COD)Cl] in the presence of DMSO, parahydrogen and Z-OMPD to form the SABRE active equatorial complexes E1 and E2 and axial complexes A1 and A2. The DMSO complex ([Ir(IMES)Cl(H)$_2$(DMSO)$_2$]), which enhances parahydrogen ex-change, is also formed in the process. [B] Reversible exchange of parahydrogen and Z-OMPD via the SABRE active complex E1. [C] Reversible exchange of parahydrogen and Z-OMPD via the SABRE-active complex E2

The second is the axial complex A1 (**Figure 4.2A**), in which the coordination occurs axially. For comparison with previous works [133,134] (pyruvate as the substrate), A1 and E1 correspond to 3a and 3b, respectively in reference.[133] Assuming only A1 and E1 complexes are formed, the labelled C-1 position is expected to be the main target of polarization since C-5 is not

directly bound to the iridium complex in these configurations, as illustrated in Scheme 1b. However, our experimental observations with Z-OMPD show significant polarization on both C-1 and C-5 (though P_{13C} for C-1 is 1.6× higher) as shown in **Figure. 4.1B**. This result implies that Z OMPD also exhibits other coordination modes such as A2 and E2 in contrast to pyruvate or other alpha-keto carboxylates.[93,97]

We hypothesize that the **E2** complex in which both C-1 and C-5 coordinate with the iridium center of the catalyst is responsible for C-1 and C-5 hyperpolarization, as illustrated in Scheme 1c. To determine which complexes are most energetically favored, we carried out DFT calculations on nine possible binding modes of Z-OMPD to the catalyst (**Figure. 4.3**) to compare their relative energies. The optimized geometries of six complexes are presented in **Figure 4.3A** (See **Figure 4.8** for the full set).The axial complexes **A1** to **A3** (and their inverse A1' to A3') are formed when Z-OMPD binds axially via the oxo groups at positions C-1 and C-2 (**A1** and **A1'**); Axial C-1 and C-5 binding is represented in **A2** and **A2'**; Axial C-2 and C-5 binding is represented in **A3** and **A3'**, respectively. Complexes **E1** to **E3** are the equatorial analogues of the axial complexes. The relative energy of each complex is presented in **Figure 4.2B**. Each complex was optimized for both the fully deprotonated and singly deprotonated carboxylate on C-1 of Z-OMPD. In computing the relative Gibbs free energies, we set the lowest energy for each protonation state to be zero, because a direct comparison between these two sets of complexes is challenging given that they have different numbers of atoms. It should be noted that at high pH (8.42) where the hyperpolarization is performed, Z-OMPD exists as the dianion (fully deprotonated), and at lower pH (between 3 and 6), Z-OMPD exists as monoanion (singly deprotonated). In this lower pH range, only the carboxylate at C-1 is deprotonated.

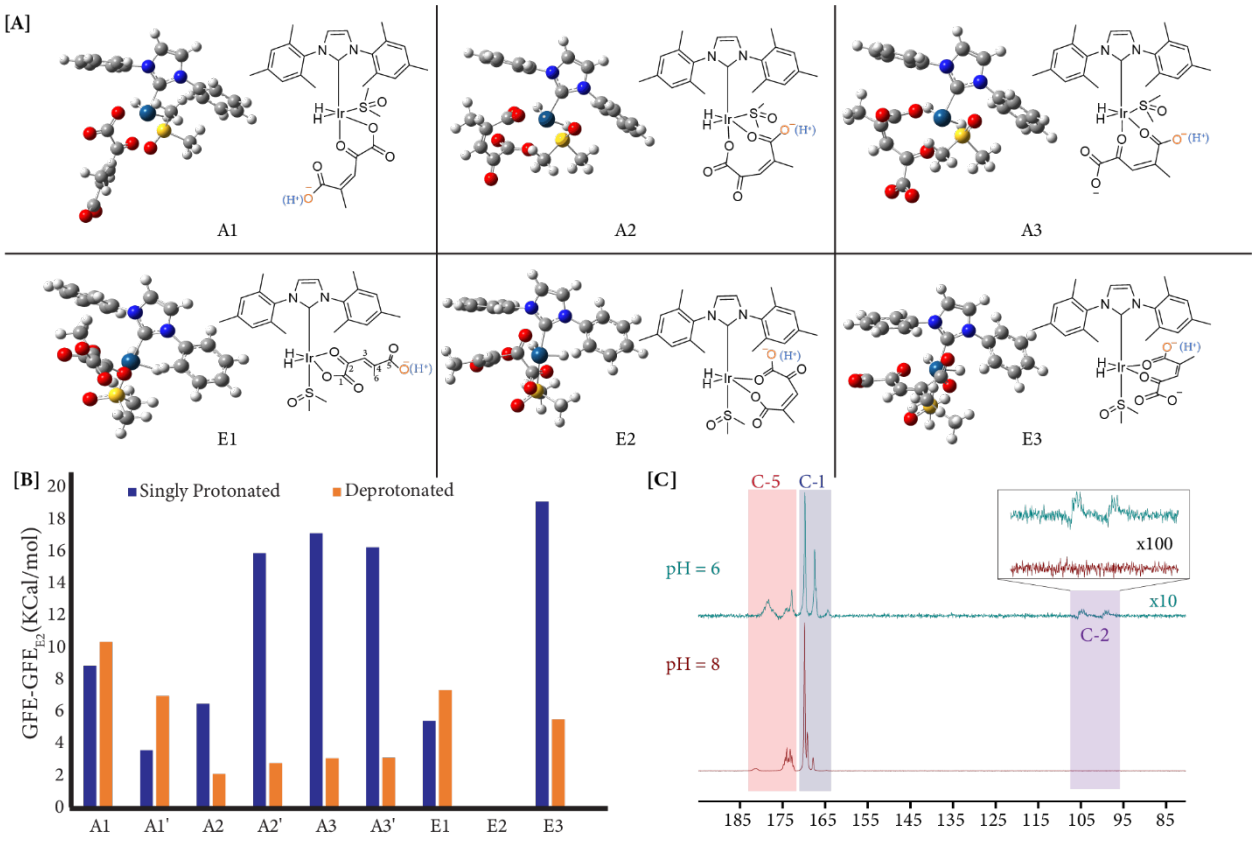

Figure 4.3. [A] 3D structures of optimized geometry of axial complexes **A1** to **A3** and equatorial complexes E1 to E3. [B] Plot of relative energies of structures **A1-A3** and **E1** to **E3** with respect to **E2** for both the deprotonated and singly protonated state of Z-OMPD. [C] Table of relative energies of structures **A1-A3** and **E1** to **E3** with respect to **E2** for both the deprotonated and singly protonated state of Z-OMPD. [D] Hyperpolarized spectra of Z-OMPD at pH 6 and pH 8, showing unlabeled C-2 is polarized at lower pH (single protonated state), therefore suggesting the **E1** complex is significantly present at lower pH

Interestingly, complex **E2** has the lowest relative energy for both the dianion (pH>6.5) and monoanion (pH<6.5) derived complexes. The **A2** complex is also relatively stable for the dianion complex. The relative stability of the **E2** and **A2** complex indicate a direct binding of the

carboxylate groups at positions C-1 and C-5, consistent with the experimental results. This finding can also be rationalized by the fact that C-1 and C-5 are the most electro-negative groups where electron density is the highest, enabling more favorable interactions with the Iridium center. Furthermore, when the experiment was performed at pH 6, where Z-OMPD is singly deprotonated at the C-1 position, we observed an overall reduction in signal intensity at both C-1 and C-5. This observation is consistent with the assumption that **E2** is the primary driver of polarization transfer, which becomes destabilized at pH<6.5, when the electron density is reduced at C-5 due to proton binding.

Relative to E2, the E1 and A1' complexes are slightly favored in the singly protonated state compared to the fully deprotonated state as shown in **Figure 4.3B** and **Figure 4.8A** (relative energy of E1 and A1' is 5.458 and 3.624 kcal/mol for singly deprotonated compared to 7.372 and 7.011 kcal/mol for fully deprotonated). The slight increase in stability of E1 and A1' at pH 6, explains our observation of polarization at the unlabeled C-2 position, which is unlike pH 8 where C-2 is not detected, since E2 is the dominant binding mode, as shown in **Figure. 4.3C**. It should be noted that though A1' is energetically more favored compared to E1 for singly deprotonated Z-OMPD, axial complexes contain spin topology that does not allow efficient polarization transfer.[134,139] Though, more studies are still necessary to determine the identity of all the active SABRE complexes in Z-OMPD, the evidence above suggests E2 and E1 as the primary active SABRE complexes with E2 driving the SABRE process at high pH (~8) and a combination of **E2** and **E1** at lower pH (~6).

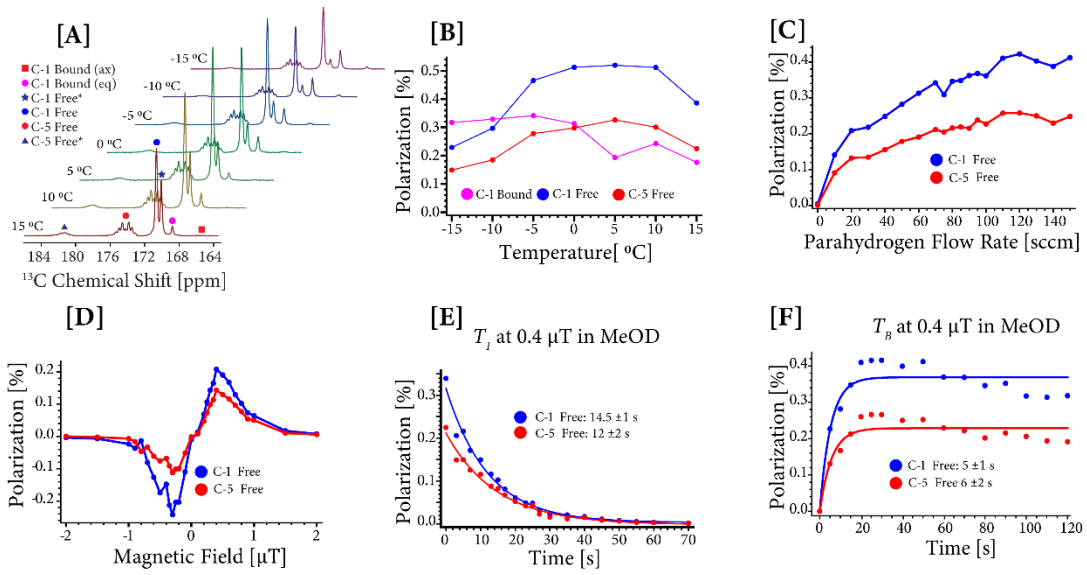

Figure 4.4. Optimization study [A] 13C HP spectra of [1,5 13C2]Z-OMPD at initial temperatures ranging from -15 to 15˚C. [B] Plot of percent polarization against initial temperature for free C-1 (blue), bound C-1 (magenta) and free C-5 (red). [C] parahydrogen flow rate dependence of Z-OMPD polarization, varied from 0-15 sccm at 100 psi. [D]. Field dependence of Z-OMPD polariza-tion. [E] T1 relaxation study of HP Z-OMPD at 0.4 μT fitted with a simple exponential decay curve. The data was collected by bubbling the sample for 30 seconds at 0.4 μT and varying the delay time. [F] polarization buildup on free Z-OMPD for both C-1 and C-5. Data acquired by varying the parahydrogen bubbling time.

Furthermore, to understand the SABRE dynamics of Z-OMPD, the temperature dependence of the C-1 and C-5 polarizations were examined in a series of temperature cycling experiments by varying the initial temperature of the sample. (Details about the temperature of the sample as a function of initial temperature and bubbling time was published previously[90]). The results are presented in **Figure. 4.4A** and **4.4B**. At the lowest temperature investigated (-15 °C), the catalyst bound C-1 peak dominates the spectrum as the exchange rate between catalyst bound and free Z-OMPD is limited, however at higher temperatures (15 °C), exchange is too fast to allow

effective SOT and consequently both free and bound species have considerably lower polarization.[90,97,116,137,212] The optimum initial temperature was found to be between 0-5 °C.

At this optimal pre-cooling temperature, efficient polarization of the bound species occurs at appropriate hydride exchange rates, while the Z-OMPD remains bound. Then, as the sample warms, Z-OMPD exchanges into the free form more efficiently, while continuing to build polarization on the catalyst, therefore we observed a high level of polarization for both the free C-1 and C-5 carbons. It should be noted that we do not observe the bound C-5 peak, likely due to the faster dissociation rates of the carboxylate group at C-5, as compared to the carboxylate group at C-1. This is consistent with the idea that the alpha-keto carboxylates alternate between the bidentate form (coordination with both carboxylates at C-1 and C-5) and monodentate form (coordination with carboxylate at C-1 alone) to promote parahydrogen exchange.[96]

This hopping mechanism between the two forms likely explains why only the peak corresponding to bound C-1 is observed. For future advances of Z-OMPD hyperpolarization, it will be crucial to precisely determine the exchange rate of Z-OMPD and the hydrides, which we were not able to quantify at this time.[96] To further improve the polarization on Z-OMPD with SABRE-SHEATH, the dependance on parahydrogen flow rate was examined. Polarization build-up is dependent on the amount of fresh parahydrogen in solution, which is regulated by the pressure and flow rate of parahydrogen. Our current experimental set up is limited to 100 psi, therefore, we investigated polarization as a function of flow rate at that pressure. As presented in **Figure. 4.4C**, we note an increase in polarization with increasing flow rate, consistent with previous studies using the pyruvate system. The highest P_{13C} for both free C-1 and C-5 Z-OMPD was achieved at a flow rate of 120 sccm. Above 120 sccm, we note a slight drop in the polarization due to the sample experiencing a wider range of magnetic fields in the SABRE-SHEATH setup as it moves up the

NMR tube, in turn decreasing magnetic field homogeneity and consequently spin order transfer efficiency.

Furthermore, to transfer polarization to Z-OMPD using SABRE-SHEATH, the frequency difference between the hydrides and the C-1 and C-5 carbons of Z-OMPD must match their J-coupling interaction.[73,117,157,158,196] This matching is achieved through careful optimization of the magnetic field sensed by the nuclei in the μT range (measured using a Twinleaf magnetometer). **Figure. 4.3D** shows the polarization of C-1 and C-5 as a function of polarization transfer field (PTF). The negative fields correspond to magnetic fields that are inverted relative to the spectrometer field. The inverse field also produces inverted HP magnetization. (**See Figure 4.9**) The maximum P_{13C} for both free C-1 and C-5 is observed at ~0.4 μT. The slight asymmetry between positive and negative fields is due to altered magnetic field paths during transport when polarizing and detection fields are anti-aligned.

Another important parameter of HP substrates is the T_1 relaxation time. Accordingly, we conducted a T1 relaxation study at 0.4 μT shown in **Figure. 4.3E**. This study was conducted by bubbling through the sample for 30 seconds, followed by a variable time delay (0-70 s) with the sample placed in the 0.4 μT field before detection. As seen from **Figure 4.3E**, Z-OMPD exhibits fast relaxation at microtesla fields due to intra and intermolecular interactions with the other NMR active nuclei in Z-OMPD and on the catalyst.[91,94] Specifically, at 0.4 μT, the J-coupling network that is responsible for building up of hyperpolarization in the first place, will also be responsible for relaxation when bubbling is halted. In contrast, at intermediate fields where these interactions are less dominant, Z-OMPD shows significantly longer T_1 relaxation times (1T in D2O: C-1 T_1 =, 138±26 s; C-5 T_1 = 119±1 s) as reported by Grashei et al.,[195] which is very promising for future applications.

Characterization of the polarization buildup on Z-OMPD was studied by varying the bubbling time (0-120 s) at 0.4 μT (**Figure 4.3F**). Again, the experiments were conducted as temperature cycling experiments where the sample was pre-cooled to 5 ºC and bubbling was performed at RT such that the sample experienced a temperature gradient during the bubbling time. The buildup data presented in **Figure 4.3F** was fit by a simple exponential buildup curve. Consequently, we observed a decay in polarization at later bubbling times. Under the present conditions, Z-OMPD has a surprisingly rapid polarization build up (C-1 T_B = 5.31 ± 1 s; C-5 T_B = 5.67 ± 2 s). The fast buildup and relatively quick relaxation of Z-OMPD at 0.4 μT explain the limited level of polarization achieved on both C-1 and C-5 carbons of Z-OMPD in this study. Further optimization would require the mitigation of the factors that leads to fast relaxation, this may be achieved in the future through deuteration of both Z-OMPD and the catalyst, in conjunction with polarization transfer methods that also work at elevated fields such as alt-SABRE,[213] LIGHT-SABRE,[96] SLIC-SABRE[101] etc.

4.4 pH Sensing

To showcase the pH sensing ability of HP Z-OMPD following polarization by SABRE-SHEATH, the compound was hyperpolarized as described above, transferred to a storage field of 0.5 T (using a permanent Halbach array) where the sample was depressurized, and 0.5 mL buffer (citrate-phosphate buffer was used for pH 3.08 to 7.6, and sodium carbonate-bicarbonate buffer was used for pH 8.30 to 11.14) was added to adjust pH before detection in a 1.1 T benchtop NMR instrument. As seen in **Figure. 4.5A**, we note an increasing chemical shift difference between C-1 and C-5 as pH increases. Specifically, with increasing pH, the chemical shift of C-5 increases, whereas the chemical shift of C-1 slightly decreases.

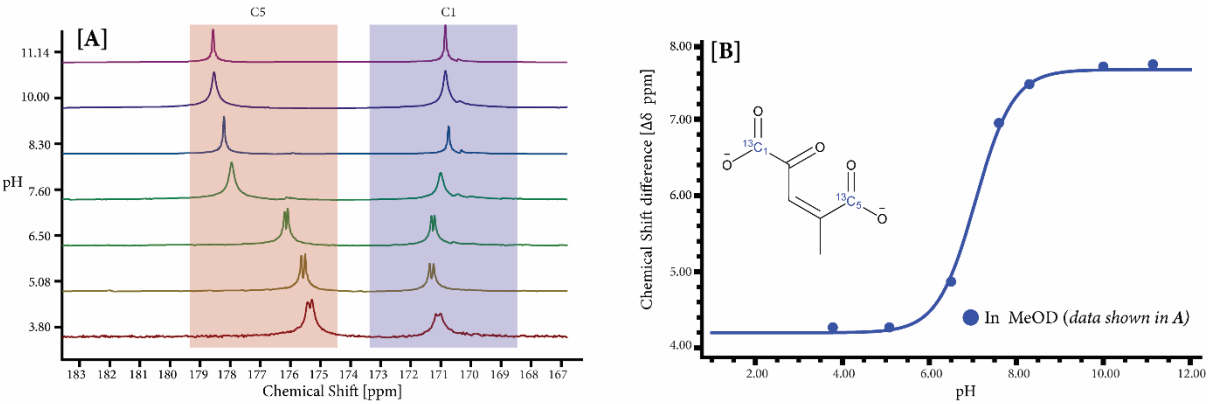

Figure 4.5. Chemical Shift difference between C-5 and C-1 of Z-OMPD dianion as a function of pH. [A] 13C NMR decoupled spectra of HP Z-OMPD at pH range between 3.80 to 11.14. The hyperpolarization step was always performed at pH 8. [B] Plot of chemical shift difference between C-1 and C-5 as a function of pH.

C-5 is more sensitive to pH changes compared to C-1 because C-5 is closer to the site which exhibits a change in protonation across this pH regime.[195,214] The difference between chemical shifts of C-1 and C-5 ($\Delta\delta_{C\text{-}5,\ C\text{-}1}$) as a function of pH shows approximately ~3 ppm shift across the examined pH range (3.80 to 11.14). In **Figure 4.5B** $\Delta\delta_{C\text{-}5,\ C\text{-}1}$, is plotted against pH.[195] The data was fit to the modified Henderson-Hasselbalch equation below:

$$pH = pKa + log\left(\frac{\Delta\delta_{c5,c1\ (observed)} - \Delta\delta_{c5,c1(protonated)}}{\Delta\delta_{c5,c1(deprotonated)} - \Delta\delta_{c5,c1\ (observed)}}\right) \quad (1)$$

In the fitting routine using Eq.1, the pKa is a fitting parameter and a value of p*K*a = 7.05 is extracted. This is different from the previously reported value of p*K*a = 6.55 in D_2O.38 The difference is likely a result of using methanolic solvent as opposed to water. The use of a chemical shift difference, $\Delta\delta_{C\text{-}5,\ C\text{-}1}$, as opposed to a single chemical shift, is particularly significant as it eliminates the need for an external standard for pH sensing, positioning HP Z-OMPD as a unique pH sensor. The data displayed in **Figure 4.5A** also reveals a pH dependent ^{13}C-^{13}C J-coupling. At pH values above 6.5, the decoupled ^{13}C peaks appear as singlets, whereas at pH values below 6.5,

doublets are recognizable, which are split by ^{13}C-^{13}C J-couplings on the order of 1.5 Hz. Interestingly, close examination of the splitting shows slightly increasing J-coupling values with decreasing pH.

4.5 Conclusion

In conclusion, we have demonstrated the feasibility of hyperpolarizing Z-OMPD at both C-1 and C-5 positions simultaneously with SABRE-SHEATH. We have studied the likely binding modes of Z-OMPD with the metal center of the hyperpolarization catalyst by experiment and DFT calculations. The work revealed that there is more than one possible binding mode of Z-OMPD to the catalyst. Particularly, at elevated pH (>6.5) the equatorial complex E2 is mostly responsible for hyperpolarization, whereas at lower pH (<6.5) a combination of E1 and E2 are found to contribute to the polarization. This study highlights the role of bidentate binding in the form of five-membered (E1) and eight-membered (E2) rings, which presents unique research opportunities in SABRE dynamics and chemistry, widening the utilization of SABRE to substrates with similar moieties, which were previously unamenable to SABRE hyperpolarization.

We also showed the important role that temperature, flow rate and polarization-transfer field play in optimization of polarization levels. One important finding is that the relaxation rates at 0.4 μT are relatively fast (~12 s at C-1 and 14.5 s at C-5) as compared to relaxation rates at higher fields (138 s and 119 s at 1 T), which indicates that polarization levels can likely be improved significantly with polarization transfer methods that work at higher fields.[96,202,213]

Finally, the enhanced signal was used to demonstrate the utility of Z-OMPD as a pH sensor. Over the pH range from pH 3.08 to pH 11.14, the chemical shift difference between C-1 and C-5 changes by 3 ppm and we used a pH dependent fitting model to extract the p*K*a. Compared to other hyperpolarization methods, the technology package of SABRE offers fast, scalable, and

inexpensive production of HP agents. The possibility of preparing HP Z-OMPD with SABRE provides a new opportunity in the development of non-invasive assessment of extracellular pH by HP MRI. In this first study, the polarization levels remained modest, below 1%. This is similar to the first hyperpolarization levels for pyruvate when first established as a SABRE substrate, which subsequently was optimized to exceed 20%.[90,94,101,133,134,215]Accordingly, we are hopeful that similarly high polarization levels will be enabled on Z-OMPD in the future.

Further studies directed towards HP ^{13}C imaging of in vivo and in vitro metabolism can also take advantage of emerging purification protocols[94,200,215,216] to ensure high signal-to-noise and full biocompatibility of the injectable solutions.

Chapter 4 Acknowledgements

Research reported in this publication was supported by the National Institute of Biomedical Imaging and Bioengineering of the National Institutes of Health under award nos. NIH R21EB025313, NIH R01EB029829, and R21EB033872. The content is solely the responsibility of the authors and does not necessarily represent the official views of the National Institutes of Health. In addition, we acknowledge funding from the Mallinckrodt Foundation, the National Science Foundation under award no. NSF CHE-1904780, the North Carolina Biotechnology Center in the form of a Translational Research Grant, and. ABS & FS would like to thank the German Cancer Consortium, ABS also thanks German Research Foundation (SCHM 3694/1-1, SCHM 3694/2-1, SFB1479), and the German Federal Ministry of Education and Research (BMBF) in the funding program “Quantum Technologies-from Basic Research to Market” under the project “QuE-MRT” (contract number: 13N16448). Finally, we would like to acknowledge the support from NCSU’s METRIC providing access to NMR instrumentation. This material is based upon work supported by the U.S. Department of Energy, Office of Biological and Environmental

Research (BER) under award number(s) DE-SC0023334.

Chapter 4 Supporting Information

S4.1 Polarization calculation

The ^{13}C polarization reported in the main paper is calculated using a thermal reference spectrum of neat [1-^{13}C]ethyl acetate (10.2 M) thermalized at 1.1 T (**Figure 4.6A**)

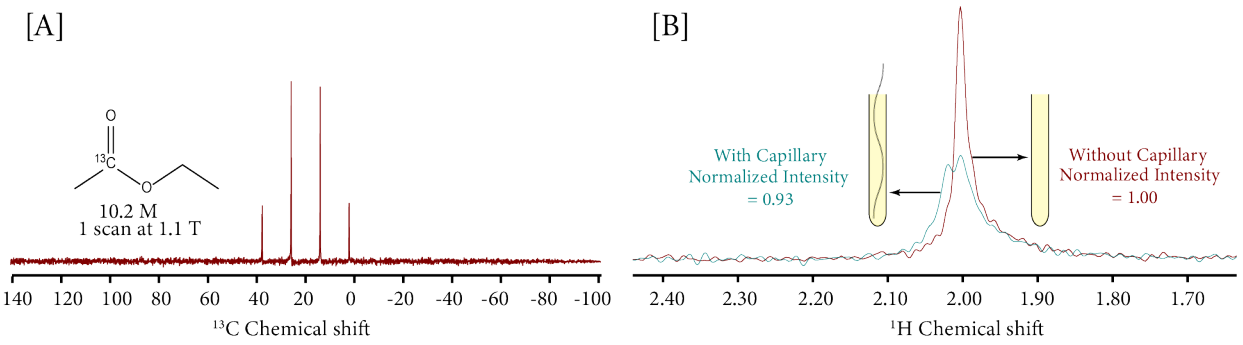

Figure 4.6. [A] A single ^{13}C NMR scan of neat [1-^{13}C] ethyl acetate thermalized at 1.1T used for polarization calculation [B] A single ^{1}H NMR scan of 60 mM CH_3CN in chloroform ($CDCl_3$) in a 5 mM NMR tube with or without capillary tube. The reference [1-^{13}C] ethyl acetate is stored in a 5 mM NMR tube without capillary while the hyperpolarized sample are measured in an identical NMR tube but with capillary for the introduction of parahydrogen.

The following equation was used to calculate polarization:

$$P_{13C} = \tanh\left(\frac{\hbar\gamma_{13C}B_0}{2k_bT}\right) \times \left(\frac{S_{HP}}{S_{REF}}\right) \times \left(\frac{Conc_{REF}}{Conc_{HP}}\right) \times \left(\frac{A_{REF}}{A_{HP}}\right)$$

Where the first term computes the thermal polarization of a ^{13}C nuclei, $\hbar$ is the reduced Planck's constant, γ_{13C} is the gyromagnetic ratio of a ^{13}C nuclei (67.2828×10^6 rads^{-1}T^{-1}), B_0 is 1.1 T, k_b is the Boltzmann's constant and T is the temperature of the detection coil which is 298 K. S_{HP} and S_{REF} are the signal intensities of the hyperpolarized and reference spectra respectively. $Conc_{REF}$ and $Conc_{HP}$ are the concentrations of the reference and hyperpolarized sample. The

initial concentration of Z-OMPD sample used is 30 mM, given that 6 mM catalyst was used for all experiment, we estimated the concentration of free and bound substrate is 24 mM and 6 mM respectively assuming a 1:1 binding of Z-OMPD to the catalyst. A_{REF} and A_{HP} are the cross-sectional area of the reference and hyperpolarized sample respectively. The difference in the cross-sectional area is due to the presence of the capillary tube used for bubbling in the hyperpolarized sample, this ratio was found to be approximately 1.07. This was measured using the ^{1}H NMR spectra of a 60 mM acetonitrile solution in chloroform in a 5 mM NMR tube with or without capillary tube as shown in Figure S 1B.[90,102]

S4.2 Expanded Temperature Sweep Data

We have expanded the temperature sweep spectra in **Figure 4.4A** in the main paper to show clearly the effects of temperature on the intensities of each peak in the hyperpolarized Z-OMPD spectra. In general, the bound C-1 peaks as shown in **Figure 4.7** (In blue) increase as temperature is decreased except at 5˚ C when optimum exchange with the free C-1 peak is observed. It is worth noting that the peaks described with asterisks (In Red) in **Figure 4.7** show decreasing intensities as the temperature is cooled to -15 °C indicating they are likely peaks of free OMPD species in solution. The peaks are likely associated with an isomer or tautomer of Z-OMPD whose specific identity is yet to be ascertained with the current available information. In the future, we aim to conduct further characterization studies to assign the peaks. It is necessary to note that the peaks marked with asterisks were not included in the calculation of the polarization levels for the C-1 and C-5 peaks of Z-OMPD, as reported in the main paper

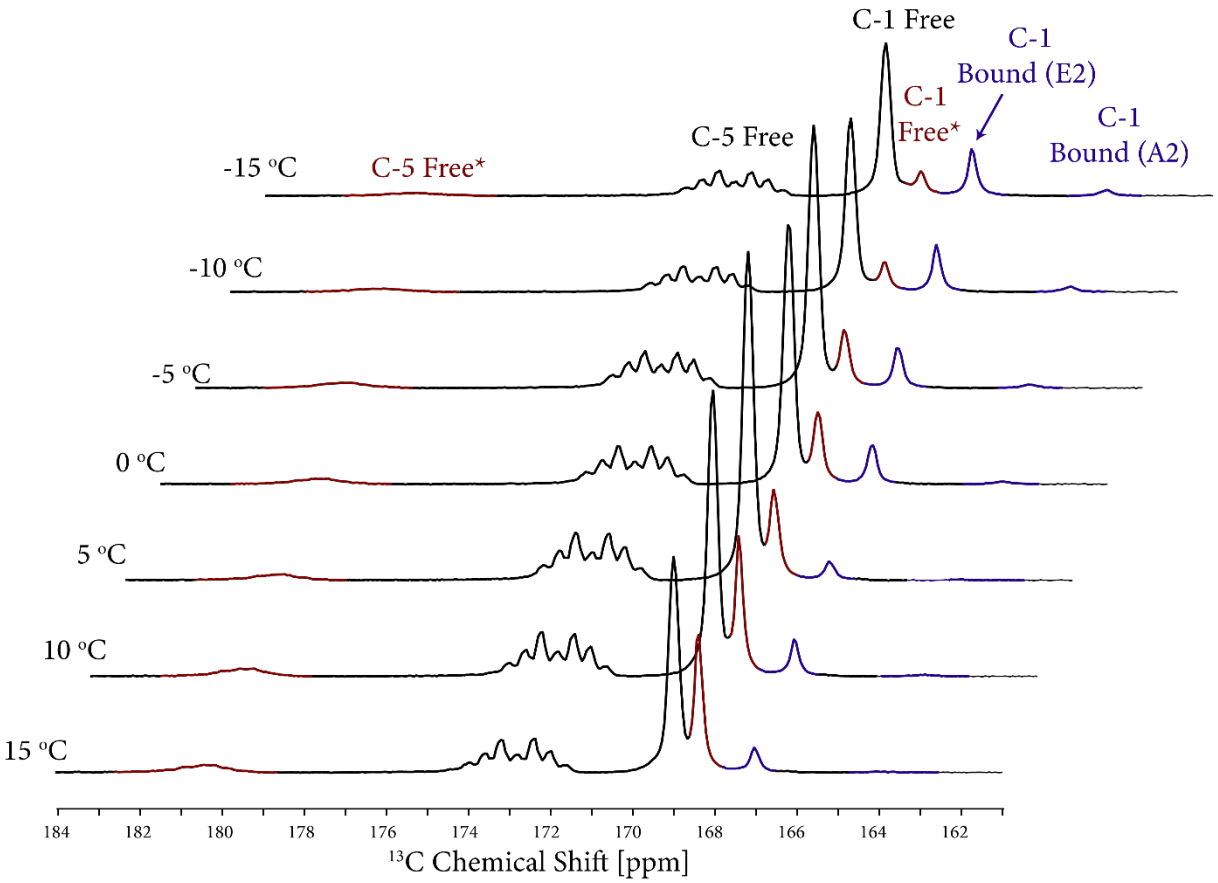

Figure 4.7. Expanded 13C NMR Spectra of hyperpolarized Z-OMPD at different initial temperatures ranging from (-15 to 15 °C). Showing the Free C1 and C5 peaks (black), Bound C1 peaks (blue), and Free (asterisks) C1 and C5 peaks (red).

S4.3 Gibbs Free Energies and Boltzmann Probabilities of Z-OMPD-Catalyst Complexes.

A table of the relative Gibbs free energies of all the nine complexes are shown below (**Figure 4.8A**) including the probability (Boltzmann Factor) of each of them relative to the most stable E2 complex for both deprotonated (**Figure 4.8B**) and protonated (**Figure 4.8C**) states of Z-OMPD. We note that in the deprotonated states of Z-OMPD, **A2** and **A2'** have the highest

probability of existence relative to **E2** at 273 K. Interestingly, In the singly protonated states, the A1' complex and E1 complex appear to have the highest probabilities relative to **E2**. The Boltzmann factor was calculated using the equation below.

$$\frac{P_i}{P_{E2}} = exp\left(-\frac{(\varepsilon_i - \varepsilon_{E2})}{K_b T}\right)$$

$$\frac{P_i}{P_{E2}} = probabilty\ of\ complex\ i\ with\ respect\ to\ complex\ E2$$

$$(\varepsilon_i - \varepsilon_{E2}) = Relative\ Gibbs\ Free\ Energy\ of\ complex\ i\ as\ listed\ in\ Fig\ S3\ A$$

$$K_b = Boltzmann\ constant$$

$$T = Temperature\ in\ kelvin$$

Furthermore, in addition to the nine complexes shown in **Figure 4.8D**, It is also possible to imagine that one of the carboxylates (C1 or C5) of Z-OMPD bind with both oxygens (**Figure 4.8E**), however in our experience, we have not observed hyperpolarization with simple carboxylic acids, therefore these complexes were excluded.

[A]

Complex	Relative Gibbs Free Energy (kcal/mol)	
	Singly Protonated	Deprotonated
A1	8.899	10.383
A2	6.524	2.155
A3	17.925	3.129
A1'	3.624	7.011
A2'	15.924	2.811
A3'	16.294	3.154
E1	5.458	7.372
E2	0	0
E3	19.143	5.549

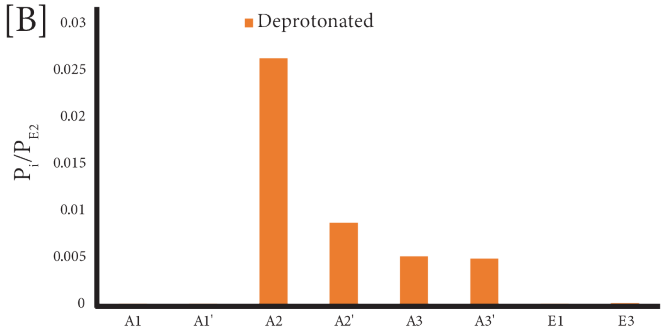

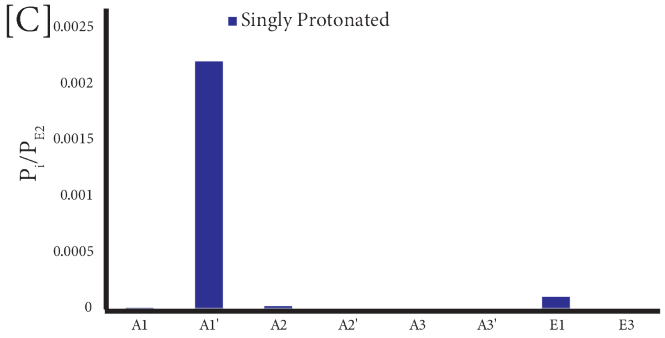

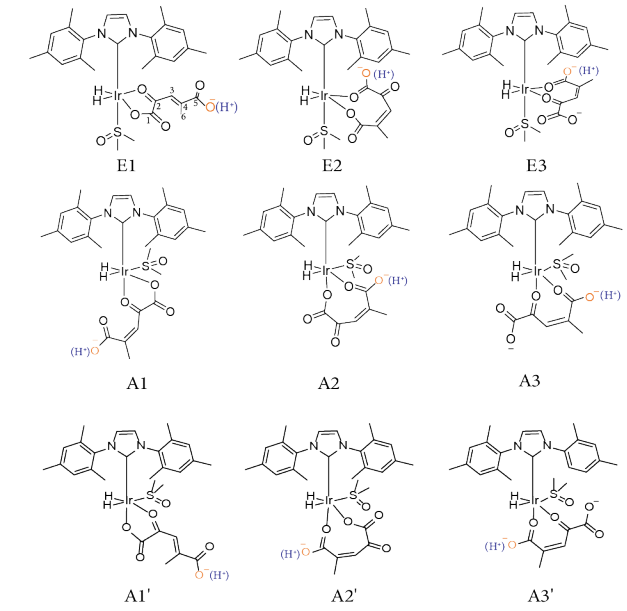

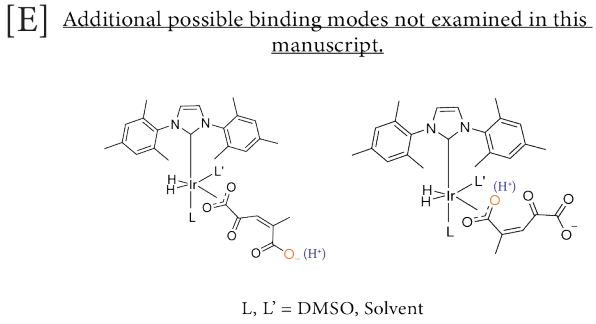

Figure 4.8. [A] Table of relative Gibbs Free Energies of all nine optimized complexes. [B] Ratio of Probabilities of complex-es **A1** to **A3**, **A1'** to **A3'**, **E1** and **E3** relative to **E2** for the Deprotonated states and [C] the singly protonated states of Z-OMPD at 273K [D] 2D structures of all nine complexes examined. [E] Possible binding modes through carboxylates of C-1 and C-5.

S4.4 Polarization Transfer Field Spectra.

Hyperpolarized spectra of Z-OMPD at each field ranging from 2 µT to - 1.5 µT is shown to emphasize the effect of inverse field which results in inverted and lowered hyperpolarization.

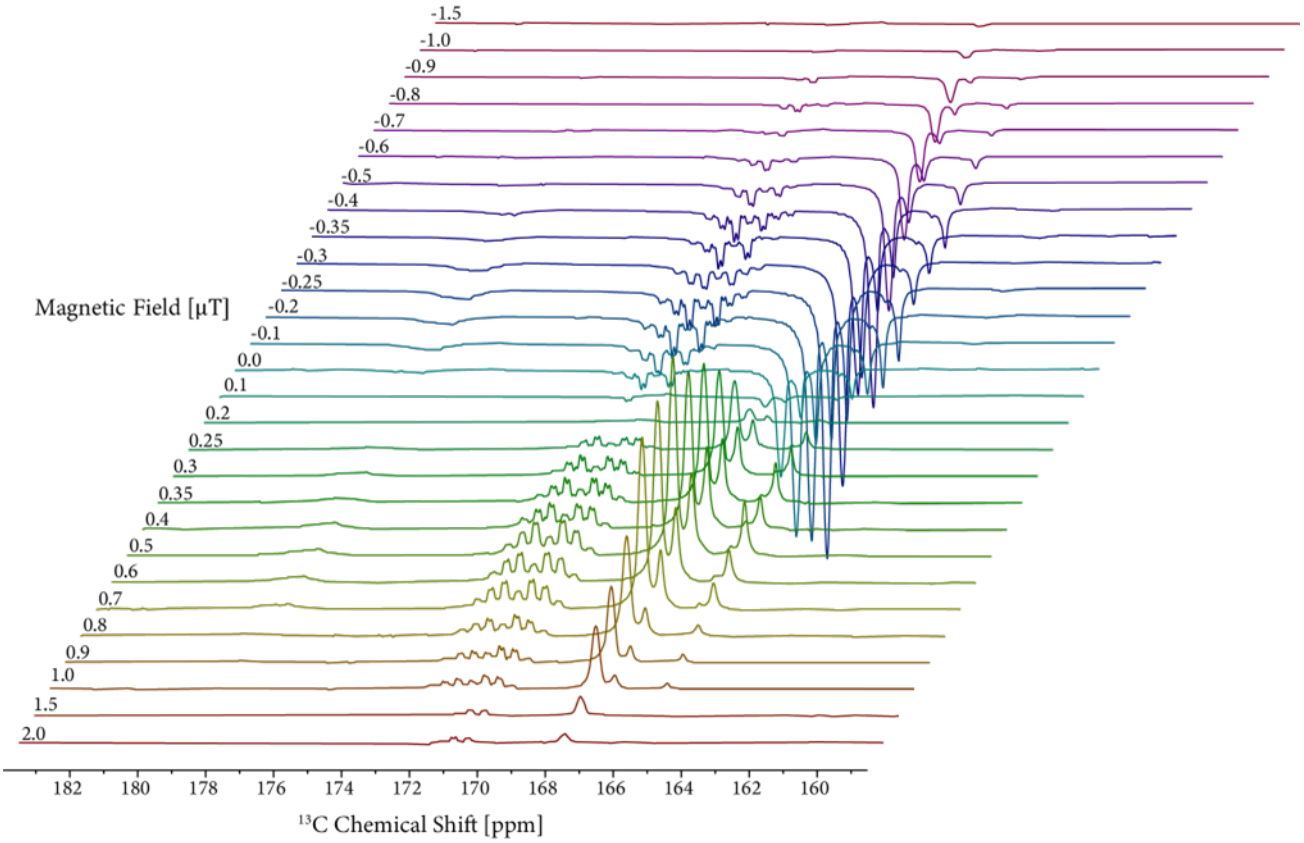

Figure 4.9. ^{13}C NMR spectra of hyperpolarized Z-OMPD at polarization transfer fields between 2.0 µT to -1.5 µT

S4.5 pH Dependence without Decoupling.

The effect of pH on the chemical shift of C-1 and C-5 of Z-OMPD was initially examined by hyperpolarizing Z-OMPD at pH ~8.4, followed by addition of appropriate amount of citrate-phosphate buffer to adjust the pH before acquiring the coupled spectra which is shown below. **Figure 4.10** shows similar trends to **Figure 4.5A** in the main document, albeit lower signal-to-noise ratio.

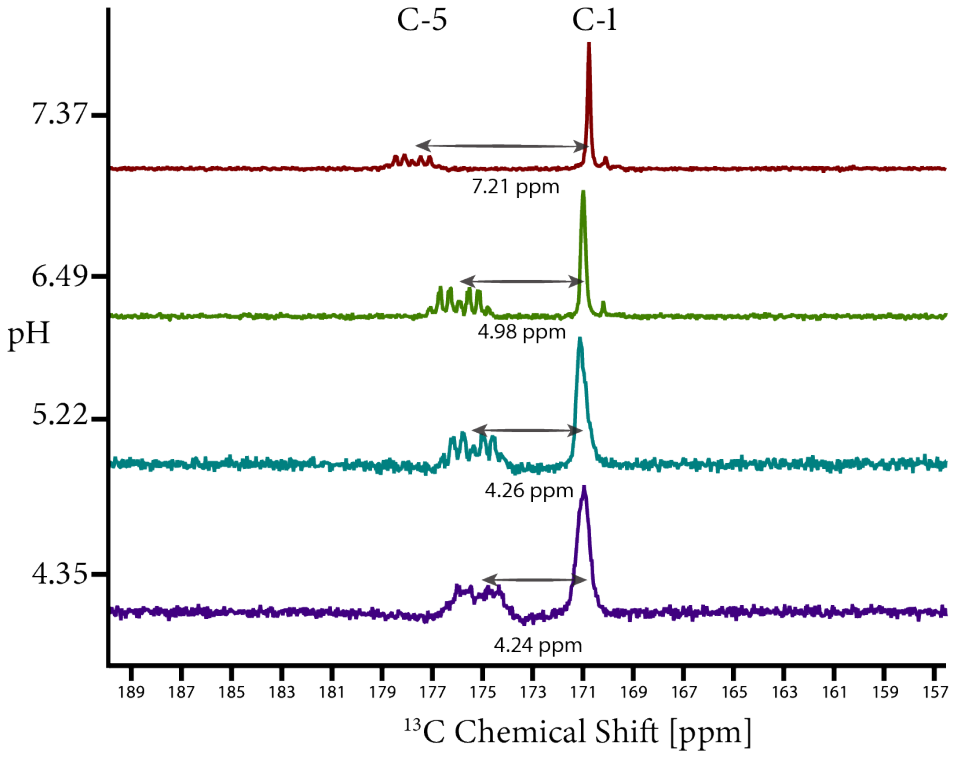

Figure 4.10. ^{13}C NMR coupled spectra of HP Z-OMPD at pH range between 4.35 to 7.37.

Chapter 5 : Hyperpolarization of imidazole in pure water via signal amplification by reversible exchange (SABRE).

5.1 Introduction

Signal amplification by reversible exchange (SABRE) has emerged as an important hyperpolarization technique for mitigating the inherent sensitivity limitations in magnetic resonance.[87,109,112,117] SABER is particularly appealing as it is fast and delivers continuous hyperpolarization of substrate without any chemical modification necessary.[89] However, SABRE is yet to be established as a viable clinical hyperpolarization technique for biomedical applications—the main driving force for most hyperpolarization methods.[191,197,217] This limitation arises from the nature of SABRE being more effective in organic solvents thereby raising concerns about toxicity.[87,110,117,147,218] The effectiveness of SABRE exclusively in organic solvents compared to biocompatible solvents, such as water, arises from the insolubility in water of the organometallic catalysts used for polarization transfer.[110] Additionally, hydrogen is less soluble in water and SABRE efficiency is directly linked to the concentration of fresh parahydrogen in solution.[110,112,116,126] Thus, current SABRE methods require purification of the substrate after hyperpolarization by removal of both the organometallic catalyst and organic solvents. This is done through extraction, phase separation and gas stripping mechanisms.[144] Due to the limited lifetime of the hyperpolarized substrate, the signal loss during the purification process is significant.

However, it might be possible to shorten the purification process by using a water-soluble catalyst that allows the polarization of the target substrate directly in water. This effectively removes the extraction and gas stripping step, thus leading to improved signal to noise ratio of

purified substrate solution. Water soluble catalysts are generally designed by functionalizing the magnetization transfer catalyst with solubilizing groups.[110] This has been achieved in three different ways; addition of an axial co-Ligand with polar groups (A),[153] adding polar groups to the mesityl moiety of [Ir(NHC)(COD)Cl] (B),[219] substituting the mesityl group with more water-soluble groups [Ir(NHC)(COD)Cl] (C).[151,152] Another alternative approach is using polar substrates to activate the standard [Ir(IMes)(COD)Cl] catalyst such that upon activation (D), it becomes water soluble. This is done by dissolving the catalyst and the substrate in a suitable organic solvent. Upon activation, the solvent is evaporated, and the mixture is redissolved in water.[155] **Figure 5.1** summarizes the different approaches to designing active water-soluble SABRE catalyst.

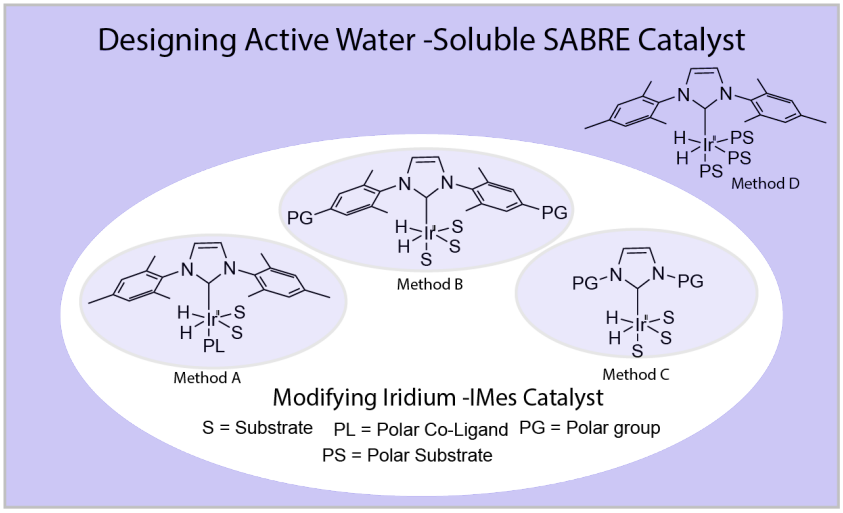

Figure 5.1. Summary of approaches towards designing active water-soluble SABRE catalyst

Till date, water-soluble catalysts are considerably less effective in transferring polarization. The highest level of enhancement achieved using any of the method is 42-fold ^{1}H enhancement.[110]

This low efficiency has been attributed to the low solubility of hydrogen in water and their below optimal spin-spin coupling.[110,153] Nevertheless, careful optimization of relevant polarization parameters can result in highly enhanced signal in water.

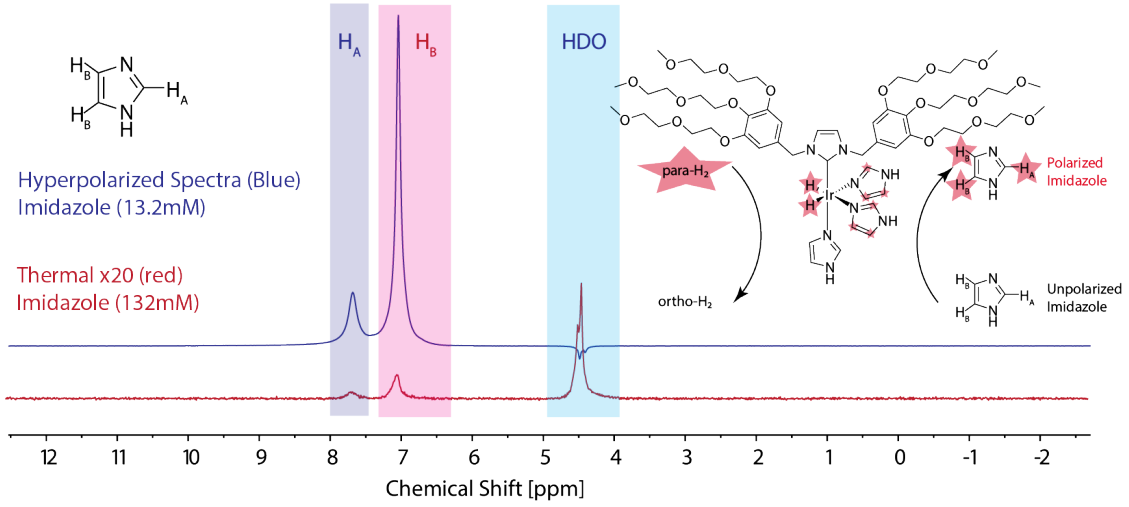

Figure 5.2: Hyperpolarized 1H NMR spectra (Blue) of 13.2 mM Imidazole in the presence of 0.66 mM [Ir(IDEG)(COD)Cl] catalyst prepared in 0.75 ml of 99.9 % D_2O, obtained after bubbling para-hydrogen in the solution for 30 seconds at 100 psi and 75 sccm flow rate. Thermal ^1H NMR Spectra (Red) of 132 mM Imidazole scaled 20 times. Schematic diagram (In set) of Imidazole and parahydrogen binding reversibly to the activated water-soluble catalyst [Ir(IDEG)(H_2)(Imidazole)$_3$].

Here, we report a significant improvement in direct hyperpolarization of imidazole in pure water using the water-soluble catalyst [Ir(H)$_2$(IDEG)(imidazole)$_3$] (**Figure 5.2**). The signal enhancements achieved on both proton resonances of imidazole are ~2000-fold compared to thermal signal. This was achieved through careful optimization of temperature, flow rate, catalyst to substrate ratio, polarization transfer field and pH. Imidazole is a particularly interesting molecule as it is a key component in histidine and its' amine derivative, histamine. Imidazole plays

a major role in enzyme catalysis,[220] metal-protein binding,[221] drug development,[222] protein purification and biochemical assays.[223] Furthermore, imidazole is the main component in the common extracellular MR pH sensor, 2-imidazole-1-yl-3-ethoxycarbonylpropionic acid (IEPA).[188,224] Specifically, the chemical shift of the H_A proton of the imidazole ring is highly sensitive to changes in local tissue and organ pH. Thus, the chemical shift changes of both H_A and H_B of imidazole as a function of pH was verified and reported here. Finally, we also observed a significant enhancement on the HDO signal in the neutral pH range (6 to 8).

5.2 Materials and methods

Imidazole was purchased from VWR and was used as received. 99% D_2O/H_2O was purchased through Cambridge Isotope Laboratories and freeze-pump-thawed before use. Pre-catalyst [Ir(IDEG)(COD)Cl] was synthesized from methyl gallate in 5 steps according to literature.[152]

The standard sample used in most of the experiments in this study composes 13.2 mM imidazole and 0.66 mM [Ir(IDEG)(COD)Cl] pre-activated catalyst prepared in 0.75 ml 99.9% D_2O/H_2O. Each sample was prepared by transferring 75 μL of 132 mM imidazole, 150 μL of 3.3 mM pre-activated catalyst solutions in D_2O into a scintillation vial followed by addition of the right amount of D_2O. This solution was degassed with argon before transfer to a 5mm medium-walled NMR tube (Wilmad WG-1003, 5 mm OD, 0.43 wall thickness) fitted with a 1/4” outer-diameter (OD) Teflon tube extension and connected to a parahydrogen bubbling set up through a Wye 1/8” to 1/4" push to connect as described previously.

5.3 Results and discussion

In the presented work, a standard sample of imidazole and pre-catalyst in aqueous solution was bubbled with parahydrogen at 60℃ (temperature of water-bath) for 30 min to form the activated complex, [$Ir(H)_2$(IDEG)$(imidazole)_3$]. SABRE experiments were performed by bubbling parahydrogen through the sample for 30 seconds at 6.5 mT and 60℃. The sample was immediately transferred to a 1.1 T benchtop NMR magnet for detection. The resulting single scan ^{1}H NMR spectrum of imidazole is shown in **Figure 5.2**. The hyperpolarized spectrum (blue stroke) is stacked over the thermally polarized spectrum (red stroke) obtained using 132 mM imidazole sample (10-fold compared to hyperpolarized sample). The thermal spectrum is scaled twenty times for ease of visualization. The two imidazole hydrogens H_A and H_B at 7.93 and 7.30 ppm (relative to 4.74 HDO peak) show polarization levels of 0.7% and 0.82% which amount to ~2000 and 2500-fold enhancements respectively.

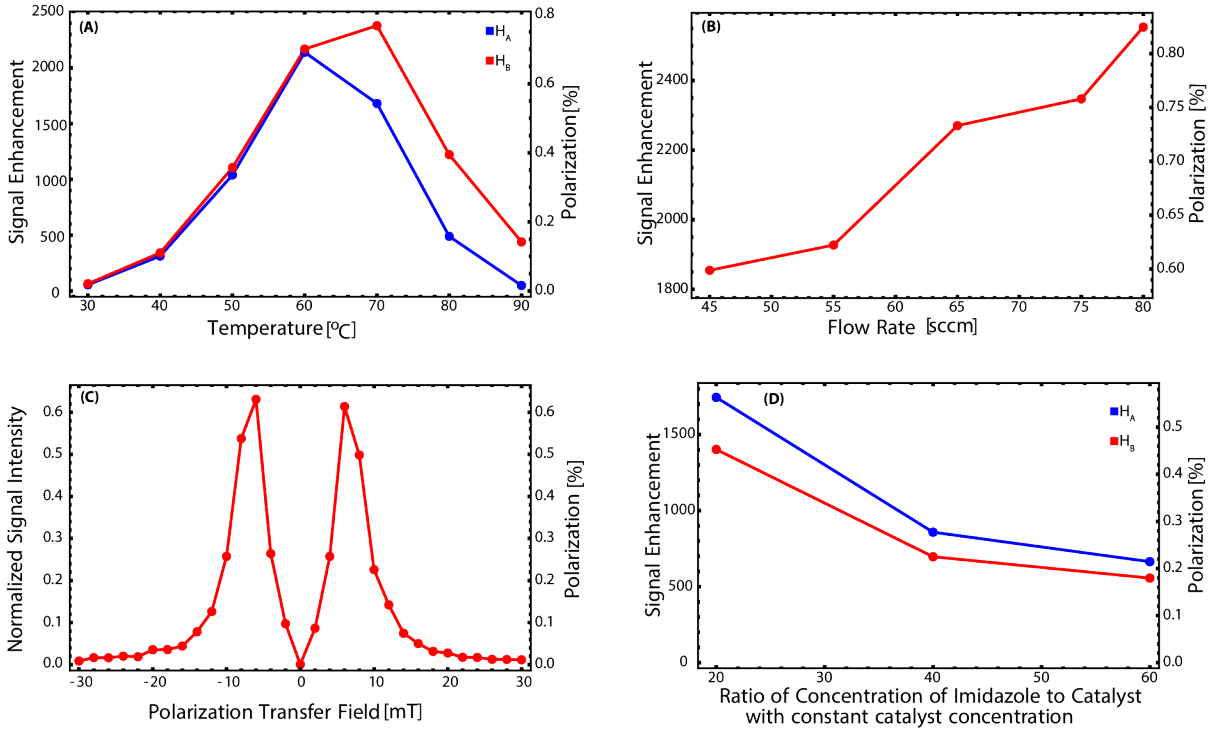

Figure 5.3. [A] Temperature dependence plot of H_A and H_B of imidazole showing signal enhancement relative to thermal at various temperatures. [B] Flow rate dependence plot of H_B of imidazole showing signal enhancement at different para-hydrogen flow rate. [C] polarization transfer field dependence of imidazole H_B signal enhancement. The PTF was varied from -30 mT to 30 mT. [D] Sample concentration dependence for imidazole signal enhancement, catalyst concentration remained constant while imidazole concentration was varied to achieve 20:1, 40:1 and 60:1 ratio of imidazole to catalyst.

The effect of temperature on hyperpolarization of imidazole in water was studied to get an insight into the dynamics of the system. As shown in **Figure 5.2A**, low polarization was observed at low temperatures (below 30 degrees). However, as the temperature increased, the polarization level increased drastically reaching a plateau at 60 degrees for both hydrogens before dropping off beyond 70 degrees. At low temperatures, the concentration of hydrogen in the solution is reduced. The high viscosity and surface tension of water prevents efficient diffusion of hydrogen in

solution; this limits the formation of the non-classical hydrogen complex [$Ir(H)_2(\eta$-$H_2)$(IDEG)$(imidazole)_2$] responsible for refreshing parahydrogen into the activated complex.[110,116,153]

Interestingly at higher temperatures, we recorded more enhancements on the H_B protons compared to the H_A proton, this is due to the latter's rapid exchange with the deuterium of D_2O as the temperature is increased or the longer the sample is kept at an elevated temperature.[225,226] This deuterium-hydrogen exchange at H_A explains the increase HDO signal at neutral pH. This mechanism will be explored further in the pH study section. Meanwhile, for experiments such as flow rate, polarization transfer field, relaxation and build up studies that require more time to acquire data, only the H_B protons were used to study these effects.

The amount of parahydrogen in solution is directly proportional to efficient polarization transfer in SABRE.[110,112,117] Thus, increasing parahydrogen flow rate has a significant effect on the polarization levels achieved on the imidazole. **Figure 5.2B** shows a maximum polarization levels on H_B of imidazole at 80 standard cubic centimeter (sccm) which is the experimental limit of our current set up. We believe that the polarization levels can be pushed higher with a thick walled, wider inner diameter NMR tube. The efficiency of SABRE hyperpolarization is highly dependent on the applied magnetic field during polarization transfer, as optimal polarization occurs near specific polarization transfer fields where level anti-crossings (LACs) facilitate efficient spin order transfer from parahydrogen to the substrate.[73,117,157,227] Thus, polarization transfer field varied from +30mT to -30mT using a solenoid coil powered by a DC supply. The coil is equipped with a cylindrical water bath to maintain constant temperature for the duration of polarization which is typically 30s. As shown in **Figure 5.2C**, the highest polarization was achieved at +/- 6.5 mT in agreement with previous studies on ^1H SABRE.[86,87,228]

The ratio of Imidazole concentration to catalyst was also studied by keeping the catalyst concentration constant and varying imidazole concentrations to give 20:1, 40:1 and 60:1 ratios of Imidazole to catalyst, the polarization levels achieved in each sample were plotted against their ratios as shown in **Figure 5.2D**. The highest enhancement was achieved at 20:1 ratio. This is consistent with previous study and analytical SABRE models. Increasing substrate concentration limits parahydrogen exchange since both hydrogen and substrate exchange occur through similar pathways.[110,112,117,229]

The relaxation on the H_B proton of imidazole was studied at low field (6.5 mT) by bubbling for 30s in the solenoid coil, followed by waiting for a variable time before transferring to a 1.1 T benchtop NMR magnet for detection. The same procedure was followed for monitoring relaxation at high field (1.1 T) except that the sample was transferred to the detection field and then stored for a variable period before detection.

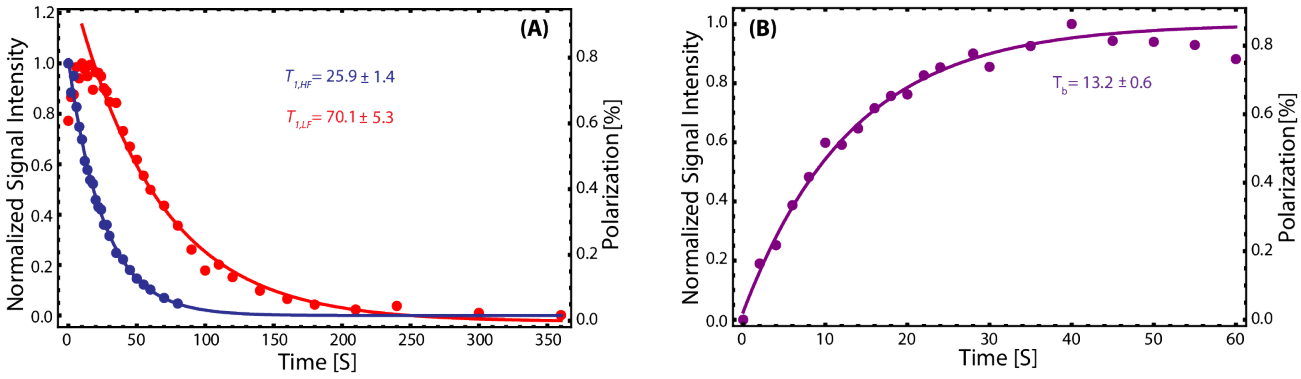

Figure 5.4. [A] Relaxation data of hyperpolarized H_B frequency of imidazole at 1.1 T (blue) and 6.5 mT (red). Each data collected after bubbling parahydrogen for 30 seconds through the standard sample composition (13.2/0.66 Imi/Cat in 0.75 mL 99.9% D_2O) [B] Build up data of hyperpolarized H_B frequency of imidazole at 6.5 mT. each data point collected by bubbling parahydrogen through the standard sample at variable time T.

Both data were fitted with a single exponential decay and showed long T_1 times unusual for a 1H nucleus (**Figure 5.4A**). We observed that lifetime at 6.5 mT is more than double the lifetime at 1.1 T.

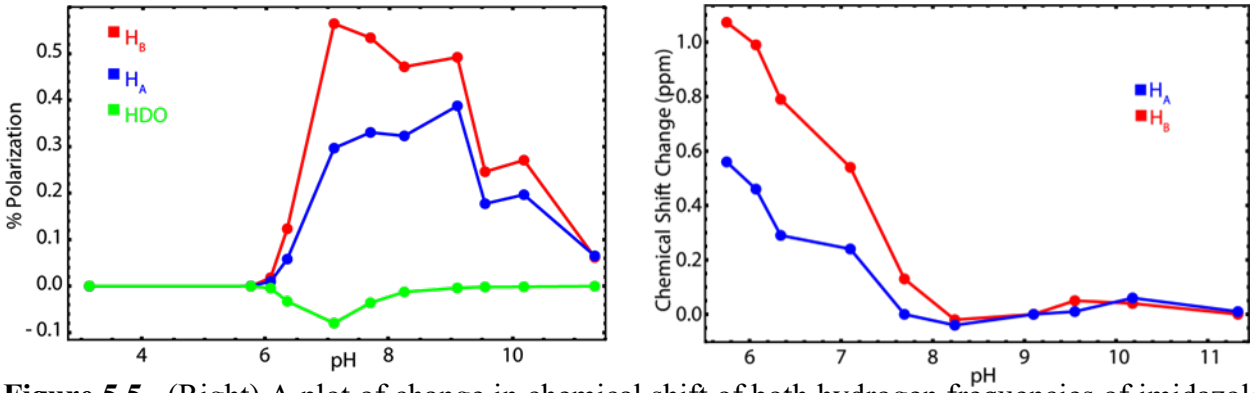

Figure 5.5. (Right) A plot of change in chemical shift of both hydrogen frequencies of imidazole as a function of pH. The chemical shift at pH 9.10 (13.2 mM/0.66 mM Imidazole: Catalyst) was used as reference chemical shift. pH adjusted by adding appropriate amount of HCl or NaOH. (Left) Efficiency of SABRE hyperpolarization of the two proton frequencies of imidazole and the single proton frequency of HDO as a function of pH.

The rate of SABRE polarization build-up was measured by varying the duration of parahydrogen bubbling, as continuous delivery of parahydrogen enhances the efficiency of spin exchange event. We observed a characteristic polarization build up curve (**Figure 5.4B**) for H_B of imidazole at 6.5 mT that approaches saturation at 13.2 seconds. The unusually long lifetime is attributed to the fast build-up of polarization on the free imidazole specie. At low field (6.5 mT), even after stopping parahydrogen bubbling, there exists a competition between polarization build up and relaxation until finally the latter dominates as shown in **Figure 5.4A**. In contrast, at high field (1.1T), transfer of polarization is halted as the level anti-crossing condition is no longer met. At this field, relaxation is the only dominant effect.

5.4 pH dependence study

The effect of pH on ^{1}H SABRE hyperpolarization of imidazole was investigated by varying the pH of the standard sample from 3.13 to 11.33 by appropriate amount of HCl or NaOH. **Figure 5.5A** shows a plot of polarization as a function of pH. At acidic pH (3.13 to 6), Imidazole is in a fully protonated state and therefore unable to bind with the catalyst thus no significant levels of polarization were observed, between pH 6.07 and 7.10, a steep increase in polarization occurs since imidazole gradually moves to its neutral state and therefore has enough electron density to bind with the iridium center of the catalyst. The highest level of polarization on H_B was recorded at pH 7.1. Interestingly, at this pH, HDO peak was also significantly enhanced indicating an optimum proton/deuterium exchange between D_2O and polarized free imidazole. Beyond pH 9.10, imidazole is fully deprotonated, therefore binds more strongly to the catalyst resulting in less polarization on the free imidazole pool due to inefficient exchange.

Furthermore, Imidazole protons, especially H_A, is known to show sharp chemical shift changes between physiologically important pH ranges 6 to 8 making it a potential candidate for extracellular pH sensing.[188,224] **Figure 5.4B** shows a change in chemical shift as a function of pH referenced to the chemical shift of imidazole at 9.10 which is the pH of pure imidazole solution in D_2O. As the pH is reduced chemical shift of both H_A and H_B moves downfield as imidazole moves from partially protonated to the fully protonated species at lower pH.

5.5 Conclusion

In this chapter, we demonstrated the successful direct SABRE hyperpolarization of imidazole in water using the water-soluble iridium catalyst, $[Ir(H)_2(IDEG)(imidazole)_3]$. Remarkably, we achieved signal enhancements of up to ~2000-fold, substantially surpassing previously reported values for aqueous SABRE, where the maximum enhancement has been ~42-

fold. Through systematic optimization, we identified key conditions that maximize polarization efficiency: a substrate-to-catalyst ratio of 20:1, a polarization transfer field of 6.5 mT, and an optimal temperature of 60 °C. Higher parahydrogen flow rates also led to improved enhancements, and polarization buildup was rapid, reaching saturation within ~13 seconds. Additionally, we observed unusually long longitudinal relaxation times (T_1) for H_B of imidazole (~71 seconds at 6.5 mT and ~26 seconds at 1.1 T). further supporting the stability of the hyperpolarized state.

We also investigated the influence of pH on SABRE efficiency and found that polarization was maximized near neutral pH (7.1). In this pH range (6-7), we observed evidence of hydrogen/deuterium exchange at the H_A position of imidazole, as well as hyperpolarized HDO signals. Lastly, we characterized the pH-dependent chemical shift behavior of imidazole protons H_A and H_B, noting a sharp transition in chemical shift between pH 6 and 8. Proton H_A was particularly sensitive to pH changes, aligning with previous reports[188,224] and highlighting its potential as a pH sensor under physiological conditions.

Together, these findings establish a robust framework for SABRE hyperpolarization of biologically relevant molecules in aqueous media and support the development of hyperpolarized imidazole-based molecular probes for chemical and biomedical applications.

Chapter 6 : Reaction monitoring using SABRE-SHEATH hyperpolarized ^{15}N sodium nitrite.

6.1 Introduction

Hyperpolarization significantly enhances the sensitivity of nuclear magnetic resonance (NMR) spectroscopy, enabling real-time reaction monitoring by boosting signal intensities by several orders of magnitude.[230–233] Among the various hyperpolarization methods, parahydrogen-based techniques have proven particularly effective for detecting and characterizing transient reaction intermediates, such as rhodium and platinum dihydride complexes formed during hydrogenation reactions.[234,235]

While ^{1}H NMR is relatively sensitive, it often suffers from spectral crowding and relatively short longitudinal relaxation times (T_1), which can limit its applicability for tracking dynamic chemical transformations. In contrast, hyperpolarized ^{13}C and ^{15}N nuclei offer longer T_1 relaxation times and sparsely populated chemical shift regions, making them well-suited for monitoring reaction pathways with high temporal resolution.[236] Of particular interest is ^{15}N NMR, which benefits from a broad chemical shift range of over 1350 ppm, allowing for enhanced resolution and selectivity.[237]

Recent advances in SABRE-SHEATH (Signal Amplification by Reversible Exchange in Shield Enables Alignment Transfer to Heteronuclei) have enabled efficient hyperpolarization of ^{15}N-labeled compounds under low magnetic field conditions. This technique has been successfully applied to monitor the reactivity of ^{15}N-labeled synthons, with hyperpolarized signals enabling the detection of reactive intermediates and products such as phenyldiazonium salts, phenyl azides, pentazoles, and molecular nitrogen, even at high magnetic fields such as 9.4 T.[146]

In this work, we extend the application of SABRE-SHEATH to the hyperpolarization of ^{15}N sodium nitrite and demonstrate its utility for monitoring azo coupling reactions on a low-field 1.4 T benchtop NMR spectrometer. This setup allows for real-time tracking of key chemical transformations using a cost-effective and portable platform.

Azo coupling reaction is a well-established and versatile transformation widely employed in the synthesis of azo dyes and pigments.[238,239] Beyond industrial applications, it plays an important role in chemo-selective bioconjugation strategies for protein labeling,[240] as well as in analytical chemistry where it is used to derivatize non-ionizable analytes for improved detection.[241]

Here, we describe the use of hyperpolarized ^{15}N sodium nitrite to monitor the formation of azo dyes through diazotization of aniline and subsequent coupling with electron-rich phenolic partners. Specifically, we investigated the reactions of phenyldiazonium salt with cresol and phenol. The diazonium salt was generated in situ via the reaction of hyperpolarized ^{15}N sodium nitrite with aniline. Thus, we demonstrated that hyperpolarized ^{15}N NMR enables real-time observation of intermediate and product formation with enhanced spectral resolution.

6.2 Materials and methods

^{15}N sodium nitrite was purchased from Cambridge Isotope Laboratories, [Ir(IMes)(COD)Cl] was synthesized from $[Ir(COD)Cl]_2$ dimer and IMes (1,3-bis(2,4,6-trimethylphenyl) imidazolinium chloride) according to literature procedure. $[Ir(COD)Cl]_2$, IMes and *N*,*N*-dimethylaminopyridine (DMAP) were purchased from Millipore Sigma Aldrich.

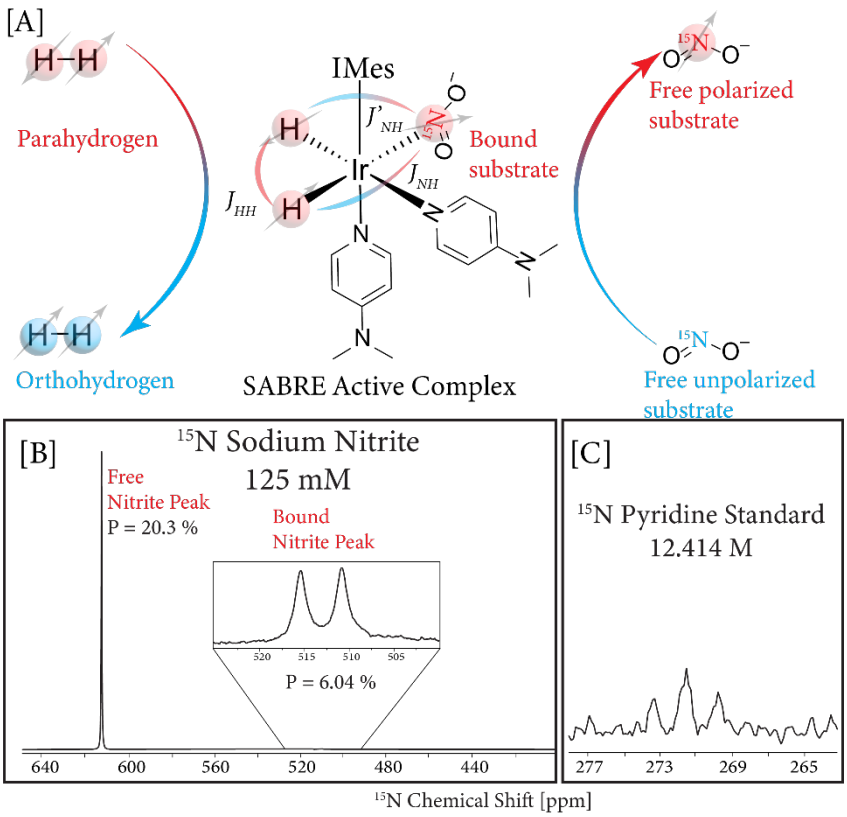

Figure 6.1. [A] Activated SABRE complex $[Ir(H)_2(IMes)(DMAP)_2(NO_2)]$ with bound nitrite and 2 eq of DMAP, showing reversible exchange of parahydrogen and nitrite. [B] Hyperpolarized ^{15}N Spectra of Sodium nitrite showing bound and free nitrite peak. [C] Thermal ^{15}N Spectra of neat pyridine.

Standard hyperpolarized sample was prepared using 125 mM ^{15}N sodium nitrite, 5 mM [Ir(IMes)(COD)Cl] catalyst, and 30 mM DMAP in normal reagent methanol. The sample was not degassed nor was the solvent dried before use. 0.6 to 0.4 ml of solution was transfer to a 5mm medium-walled NMR tube (Wilmad WG-1003, 5 mm OD, 0.43 wall thickness) fitted with a 1/4" outer-diameter (OD) Teflon tube extension and connected to a parahydrogen bubbling set up through a Wye 1/8" to 1/4" push to connect as described previously.

6.3 Results and discussion

In this work, the bubbling method was used to introduce fresh parahydrogen into the SABRE sample. The time it takes for the sample to activate was investigated by bubbling parahydrogen for a specific time and checking the polarization level. The polarization level is checked by bubbling parahydrogen through the sample while it resides in a mu metal shield at 0.5 μT for 30 seconds and immediate detection in a 1.5 T NMR magnet. The single scan signal recorded was referenced to a thermal signal of 12.4 M neat pyridine. The polarization level was calculated using the equation below:

$$P_{15N} = P_{thermal} \times \frac{S_{Hp}}{S_{ref}} \times \frac{C_{ref}}{C_{Hp}} \times \frac{A_{Hp}}{A_{ref}}$$

Where P_{15N} is the polarization level of the hyperpolarized signal. $P_{thermal}$ is the thermal polarization of a ^{15}N nuclei using the Boltzmann distribution statistics given as $P_{thermal} = tanh\left(\frac{\gamma\hbar B_0}{2k_B T}\right)$. S_{HP} is the signal from the hyperpolarized sample, S_{ref} is the signal from the pyridine reference sample. C_{HP} is the concentration of the hyperpolarized sample and C_{ref} is the concentration of the pyridine reference sample. A_{HP} is the surface area of the NMR tube housing the hyperpolarized sample while A_{ref} is the surface area of the NMR tube containing the reference sample.

As described in section 3.4 of chapter 3, nitrite reacts with the [Ir(IMes)(COD)Cl] in the presence of DMAP to form two active catalytic species: complexes **4** and **5.**[146] However, only complex **5** was observed in the NMR spectra. **Figure 6.1A** illustrates the reversible exchange of parahydrogen and nitrite ion on complex **5,** $[Ir(H)_2(IMes)(DMAP)_2(NO_2)]$. The corresponding hyperpolarized spectra (**Figure 6.1B**) display two peaks: free nitrite signal at 611 ppm and a bound nitrite signal at 513 ppm. Using the thermal spectrum of neat ^{15}N-labelled pyridine (**Figure 6.1C**)

as a reference, we calculated polarization levels of approximately 20 % for the free nitrite and 6% for the bound species.

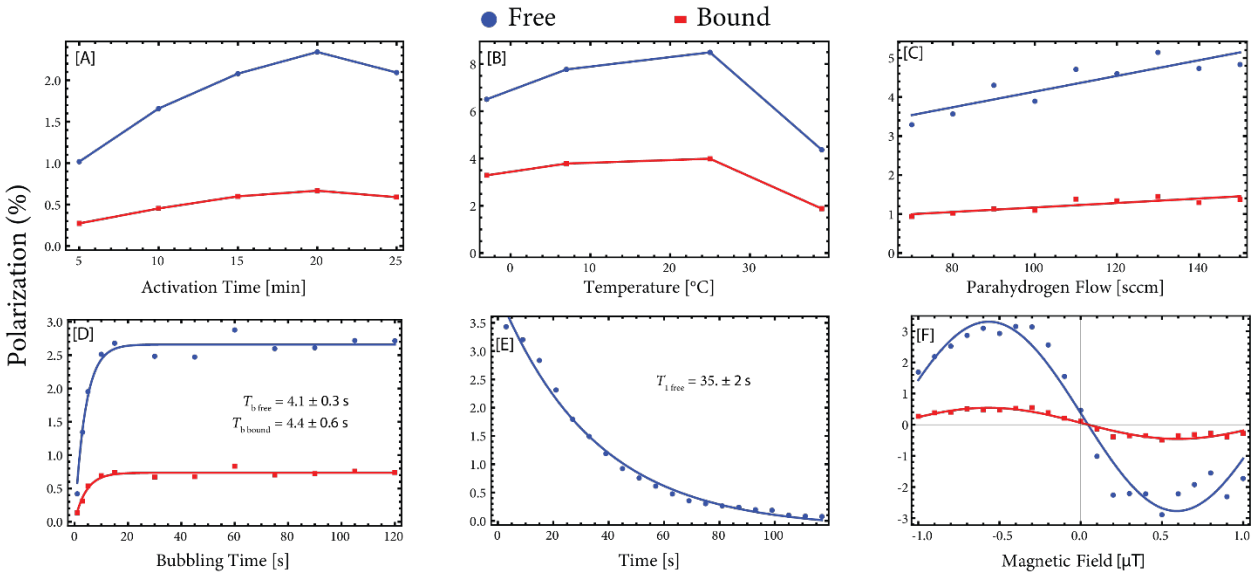

Figure 6.2 Plot of [A] activation time of Hp sample. [B] sample temperature [C] parahydrogen flow rate [D] parahydrogen bubbling time [E] spin-lattice lifetime (T_1) [F] magnetic field, showing their effects on polarization.

Firstly, to optimize the SABRE process for nitrite hyperpolarization, it is essential to determine the activation time to achieve efficient polarization transfer. Thus, we measured the polarization level during catalyst activation and plot polarization level against time. As shown in **Figure 6.2A**, the sample is completely activated in methanol after 20 minutes. The slight reduction in polarization above 20 minutes is attributable to sample degradation.

Temperature is a critical parameter in SABRE hyperpolarization, as it influences the exchange process.[90,117] To assess its role in optimizing SABRE efficiency for nitrite, the effect of temperature was investigated at four different temperatures. The highest polarization was recorded at room temperature for both the free and bound species as shown in **Figure 6.2B**. At all

temperatures examined, the free polarization is consistently higher than the bound polarization. This is indicative of both a fast buildup of polarization on the bound species and fast exchange.

The efficiency of polarization is tightly linked to the availability of parahydrogen in solutions. The higher the concentration of parahydrogen, the higher the polarization achieved.[110,112,117] The rate of flow of parahydrogen was varied to examine its effect on polarization. We observed that while polarization increases with increasing parahydrogen flow rate, we note that this effect is not as pronounced within the range examined in the study (see **Figure 6.2C**).

Furthermore, the rate at which polarization builds up on the free and bound substrate was studied by varying the parahydrogen bubbling time. It can be seen from **Figure 6.2D** that polarization on both free and bound substrate reaches its maximum after 4 secs. The result suggests a very fast exchange rate between the bound and free substrate validating the temperature data in **Figure 6.2B**.

Since the primary objective of this study is to demonstrate the use of hyperpolarized ^{15}N-labeled sodium nitrite as a tool for reaction monitoring, the longitudinal relaxation time (T_1) of the free substrate at the detection field is a critical parameter. A longer T_1 enables extended observation windows for tracking chemical transformations. To assess this, the T_1 of the free substrate was measured at 1.4 T. The experiment began by bubbling parahydrogen through the sample for 30 seconds at 0.5 μT, followed by immediate transfer to a 1.4 T benchtop NMR magnet. A series of 15° flip-angle acquisitions was then performed, with a 3-second delay between each measurement. The resulting relaxation data fitted with an exponential decay ($Ae^{-t/T_1} + B$) function is shown in **Figure 6.2E**. The measured T_1 was approximately 35 ± 2 seconds. Although this is relatively short for ^{15}N nuclei, which typically exhibit relaxation times on the order of minutes, it is consistent with

previously reported values for nitrite.[146,242] Importantly, the observed lifetime is sufficient to enable effective monitoring of chemical reactions over practical timeframes.

Finally, the effect of magnetic field on polarization transfer was examined by varying the voltage applied to the solenoid coil housed in a mu metal shield. The sample was bubbled for 30 seconds in each field and the hyperpolarized signal was acquired at 1.4 T. The data, fitted with a sine function ($A\sin(Bx + C) + D$), is shown in **Figure 6.2F**. The highest polarization was observed between 0.4 to 0.6 μT. The broad profile of the plot agrees with the conclusion from both the temperature and build up data that the nitrite system exhibits a very fast exchange dynamic.

6.4 Monitoring azo coupling reaction

Hyperpolarized ^{15}N-labeled sodium nitrite presents a promising tool for real-time monitoring of organic transformations.[146] Following initial optimization of nitrite hyperpolarization via the SABRE technique, the resulting hyperpolarized signal was employed to track the formation of azo dyes through diazotization coupling reactions. Two representative azo compounds were synthesized using phenol and ortho-cresol as diazo coupling partners.

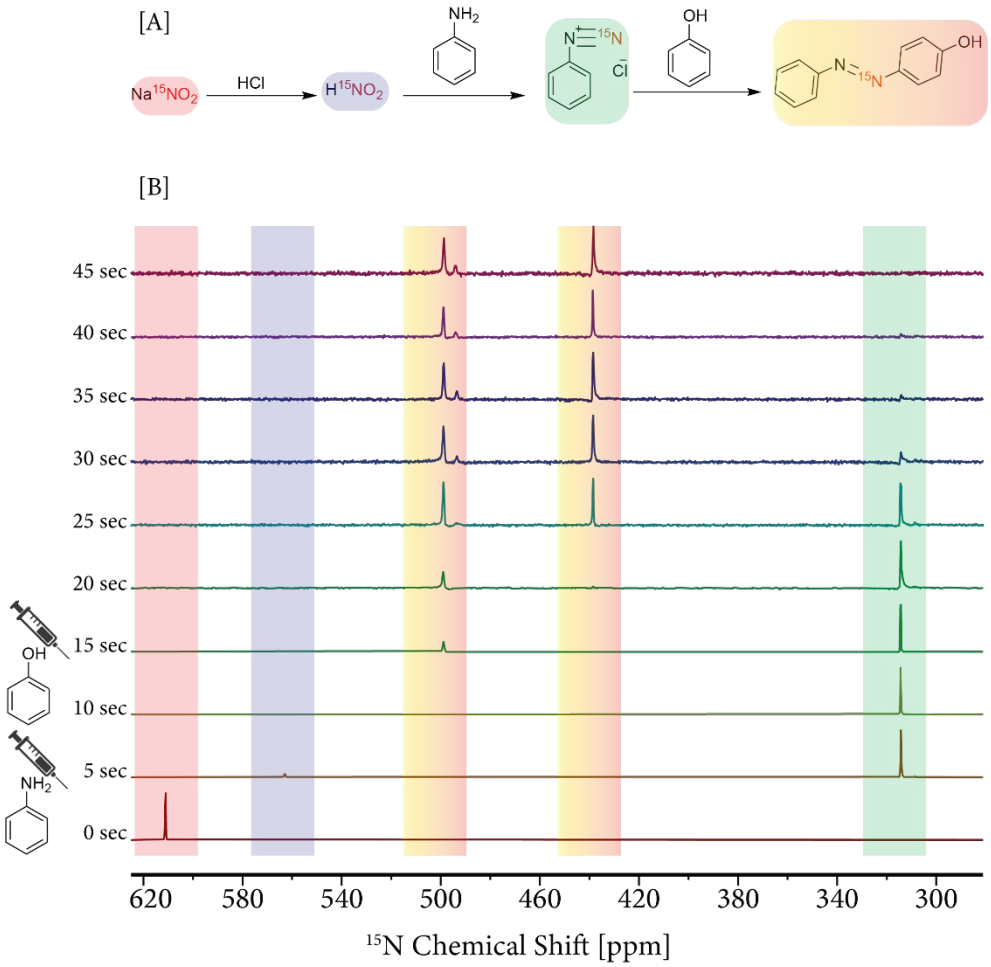

Figure 6.3. [A] Reaction scheme showing the reaction of hyperpolarized nitrite with acidified aniline solution, followed by the reaction of phenol with the diazo salt product. [B] Real time ^{15}N Spectra of the diazo coupling reaction before and after addition of aniline and phenol.

The experiment began with the hyperpolarization of 0.4 mL of the standard sample using the optimized SABRE procedure. The hyperpolarized sample was then transferred to a 1.4 T NMR magnet, depressurized, and subjected to a series of 15° flip-angle acquisitions. Following the first scan, an acidified aniline solution was added to initiate the reaction. This was subsequently followed by the addition of a basic phenol solution. **Figure 6.3A** presents the reaction scheme for the formation of 4-hydroxyphenylazobenzene.

At time zero, prior to the addition of any reagents, a single resonance at $\delta^{15}N$ 611 ppm was observed, corresponding to hyperpolarized nitrite (**Figure 6.3B**). Immediately after the addition of acidified aniline, two new peaks appeared: one at $\delta_{^{15}N}$ 563 ppm, assigned to nitrous acid, and another at $\delta_{^{15}N}$ 314 ppm, attributed to the phenyl diazonium ion. A minor peak at $\delta_{^{15}N}$ 308 ppm was also observed, likely corresponding to ortho-N_2. Within approximately 10 seconds, the nitrous acid peak at $\delta_{^{15}N}$ 563 ppm completely disappeared, indicating full conversion of nitrite to the diazonium ion.

Subsequent addition of the basic phenol solution led to the gradual appearance of a new peak at $\delta_{^{15}N}$ 498 ppm, assigned to the resulting azo dye. As the reaction progressed (around 25 seconds), an additional peak at $\delta_{^{15}N}$ 438 ppm emerged, attributed to a geometric isomer of the azo product. A minor resonance near $\delta_{^{15}N}$ 493 ppm was also detected, potentially corresponding to a tautomeric form of the peak at $\delta_{^{15}N}$ 498 ppm. The reaction appeared to reach completion after approximately 40 seconds, as the phenyl diazonium peak at $\delta_{^{15}N}$ 314 ppm disappeared from the spectrum.

The reaction of ortho-cresol followed a similar pattern as shown in **Figure 6.4A**. The spectra in **Figure 6.4B** shows a lower signal to noise ratio compared to the phenol reaction. The reaction also appears to occur slower relative to the phenol reaction. However, the two azo product peaks can be observed at δ_{15N} 495 and δ_{15N} 435 respectively showing a 3-ppm shift compared to the phenol product. The peaks also appear to be broader. It should be noted that in both reactions, the product crashes out of solution resulting in rapid loss of signal.

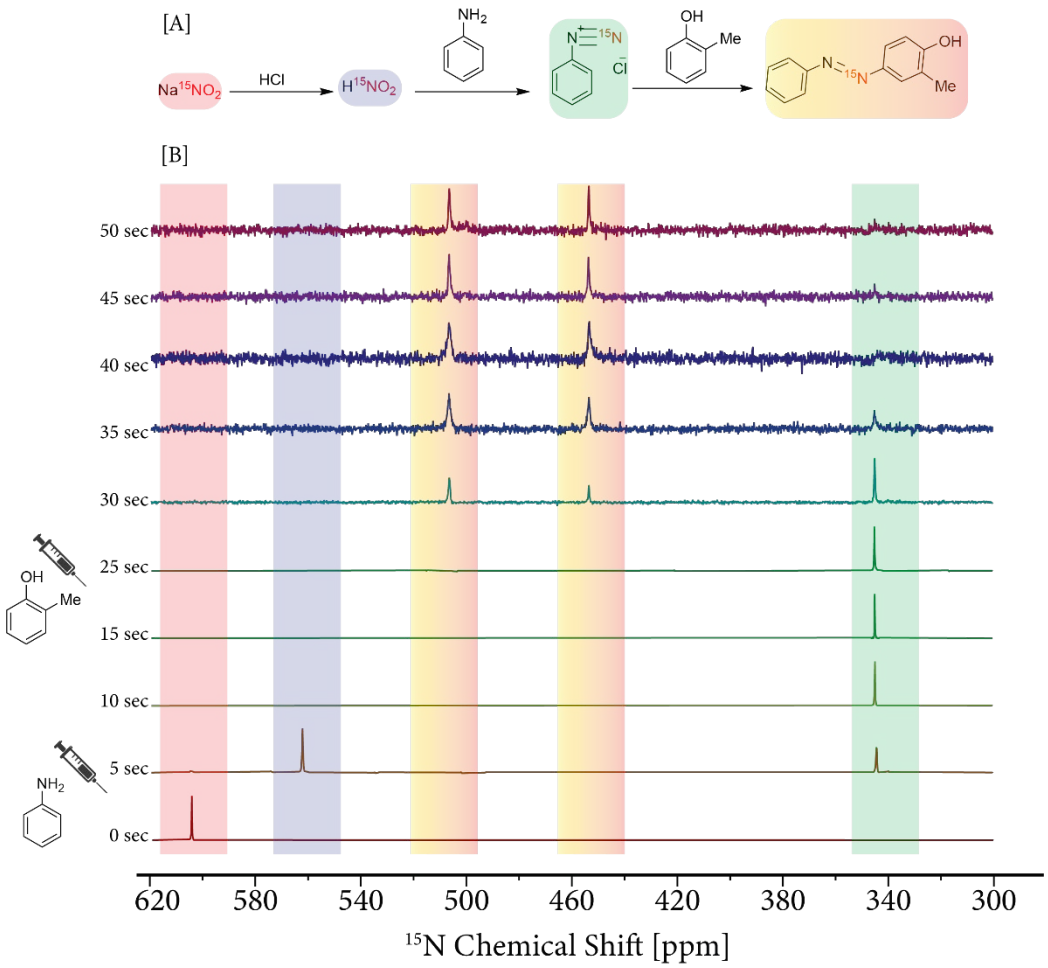

Figure 6.4. [A] Reaction scheme showing the reaction of hyperpolarized nitrite with acidified aniline solution, followed by the reaction of cresol with the diazo salt product. [B] Real time ^{15}N Spectra of the diazo coupling reaction before and after addition of aniline and cresol.

6.5 Conclusion

In this chapter, we demonstrated the successful hyperpolarization of ^{15}N-labeled nitrite using SABRE for real-time reaction monitoring applications. A series of experimental parameters were systematically optimized to maximize polarization efficiency, including catalyst activation time, temperature, parahydrogen flow rate, bubbling duration, polarization transfer field, and signal lifetime. We found that full catalyst activation was achieved after 20 minutes, with the

highest polarization observed at room temperature. While increased parahydrogen flow rate slightly improved polarization, the effect was not pronounced within the range examined. Polarization buildup was rapid, reaching saturation within approximately 4 seconds, and the signal lifetime at 1.4 T was measured to be ~35 seconds. The optimal polarization transfer field was determined to be between 0.4 and 0.6 μT, consistent with efficient SABRE-SHEATH transfer conditions.

Following optimization, the hyperpolarized nitrite was employed to monitor a representative azo coupling reaction in real time. Using phenol and cresol as coupling partners, we tracked the transformation of the reactant nitrite to the intermediate diazonium salt and ultimately to the final azo dye product. This work highlights the utility of hyperpolarized ^{15}N nitrite as a molecular probe for tracking chemical transformations with high temporal resolution, particularly in low-field NMR systems.

REFERENCES

(1) Becker, E. D. A Brief History of Nuclear Magnetic Resonance. *Anal Chem* **1993**, *65* (6), 295–302.

(2) Purcell, E. M.; Torrey, H. C.; Pound, R. V. Resonance Absorption by Nuclear Magnetic Moments in a Solid. *Phys. Rev* **1946**, *69* (681), 681.

(3) Bloch, F.; Hanse, W. W.; Packard, M. The Nuclear Experiment. *Physical Review* **1946**, *70* (5), 474–485.

(4) Lauterbur, P. C. Image Formation by Induced Local Interactions: Examples Employing Nuclear Magnetic Resonance. *Nature* **1973**, *242*.

(5) Mansfield, P. Multi-Planar Image Formation Using NMR Spin. *J. Phys. C: Solid State Phys* **1977**, *10*, 55.

(6) Pykett, I. L. NMR Imaging in Medicine. **1982**, *246* (5), 78–91. https://doi.org/10.2307/24966592.

(7) Becker, E. D.; Liddel, T.; Shoolery, J. N. *Nuclear Magnetic Resonance Studies of Hydrogen Bonding in Ethanol*; Vol. 2.

(8) Arnold, J. T.; Dharmatti, S. S.; Packard, M. E. Chemical Effects on Nuclear Induction Signals from Organic Compounds. *The Journal of Chemical Physics*. **1951**, p 507. https://doi.org/10.1063/1.1748264.

(9) Jackman, L. M.; Sternhell. S.; Barton, D. H. R. Application of Nuclear Magnetic Resonance Spectroscopy in Organic Chemistry.

(10) Shoolery, J. N.; Rogers, Max. T. Nuclear Magnetic Resonance Spectra of Steroids. *J Am Chem Soc* **1958**, *80* (19), 5121–5135.

(11) Sattler, M.; Schleucher, J.; Griesinger, C. *Heteronuclear Multidimensional NMR Experiments for the Structure Determination of Proteins in Solution Employing Pulsed Field Gradients*.

(12) Kumar, A.; Ernst, R. R.; Wfithrich, K. *Biochemical And Biophysical Research Communications Pages L-6 A Two-Dimensional Nuclear Overhauser Enhancement (2d Noe) Experiment For The Elucidation Of Complete Proton-Proton Cross-Relaxation Networks In Biological Macromolecules*; **1980**; Vol. 95.

(13) Cavalli, A.; Salvatella, X.; Dobson, C. M.; Vendruscolo, M. Protein Structure Determination from NMR Chemical Shifts. *Proc Natl Acad Sci U S A* **2007**, *104* (23), 9615–9620. https://doi.org/10.1073/pnas.0610313104.

(14) Wuthrich, K. Protein Structure Determination in Solution by NMR Spectroscopy. *Journal of Biological Chemistry* **1990**, *265* (36), 22059–22062. https://doi.org/10.1016/s0021-9258(18)45665-7.

(15) Torchia, D. A. Protein Dynamics from NMR Relaxation. *eMagRes* **2007**, *2007*. https://doi.org/10.1002/9780470034590.emrstm0419.

(16) Kumar, A.; Welti, D.; T~rust, R. R. *Kurze Originalmitteilungen Ft~r Die Tqurzen Originalmitteilungen Sind AusschlieBlich Die Verfasser Verantworttich Imaging of Macroscopic Objects by NMR Fourier Zeugmatography*.

(17) W Moonen, C. T.; M van Zijl, P. C.; Frank, J. A.; Le Bihan, D.; Becker, E. D. *Functional Magnetic Resonance Imaging in Medicine and Physiology*; **1990**; Vol. 250.

(18) Stehling, M. K.; Turner, R.; Mansfield, P. *Echo-Planar Imaging: Magnetic Resonance Imaging in a Fraction of a Second*; **1991**; Vol. 254.

(19) Gerlach, W., & Stern, O. Der experimentelle Nachweis des magnetischen Moments des Silberatoms. Zeitschrift für Physik; **1922**; 8(1), 110-111.

(20) Wang, T.; Hong, M. Solid-State NMR Investigations of Cellulose Structure and Interactions with Matrix Polysaccharides in Plant Primary Cell Walls. *Journal of Experimental Botany*. Oxford University Press January 1, **2016**, pp 503–514. https://doi.org/10.1093/jxb/erv416.

(21) Gutowsky, H. S.; McCall, D. W.; Slichter, C. P. Coupling among Nuclear Magnetic Dipoles in Molecules. *Phys. Rev.* **1951**.

(22) Carver, T. R.; Slichter, C. P. Polarization of Nuclear Spins in Metals. *Physical Review* **1953**, *92* (1), 212. https://doi.org/10.1103/PhysRev.92.212.

(23) Ernst, R. R.; Anderson, W. A. Application of Fourier Transform Spectroscopy to Magnetic Resonance. *Review of Scientific Instruments* **1966**, *37* (1), 93–102. https://doi.org/10.1063/1.1719961.

(24) Brutscher, B.; Bru, R.; Ernst, R. R. Backbone Dynamics and Structural Characterization of the Partially Folded A State of Ubiquitin by 1 H , 13 C , and 15 N Nuclear Magnetic Resonance Spectroscopy †. **1997**, *2960* (97), 13043–13053.

(25) Wüthrich, K. NMR Studies of Structure and Function of Biological Macromolecules. In *Bioscience Reports*; **2003**; Vol. 23, pp 119–168. https://doi.org/10.1023/B:BIRE.0000007689.27614.7c.

(26) Spurlin, M. S.; Barker, B. W.; Cross, B. D.; Divine, C. E. Nuclear Magnetic Resonance Logging: Example Applications of an Emerging Tool for Environmental Investigations. *Remediation* **2019**, *29* (2), 63–73. https://doi.org/10.1002/rem.21590.

(27) Bergin, E. A.; Tafalla, M. Cold Dark Clouds: The Initial Conditions for Star Formation. *Annu Rev Astron Astrophys* **2007**, *45*, 339–396. https://doi.org/10.1146/annurev.astro.45.071206.100404.

(28) Ardenkjaer-Larsen, J.; Boebinger, G. S.; Comment, A.; Duckett, S.; Edison, A. S.; Engelke, F.; Griesinger, C.; Griffin, R. G.; Hilty, C.; Maeda, H.; Parigi, G.; Prisner, T.; Ravera, E.; van Bentum, J.; Vega, S.; Webb, A.; Luchinat, C.; Schwalbe, H.; Frydman, L. Neue Ansätze Zur Empfindlichkeitssteigerung in Der Biomolekularen NMR-Spektroskopie. *Angewandte Chemie* **2015**, *127* (32), 9292–9317. https://doi.org/10.1002/ange.201410653.

(29) Lee, J. H.; Okuno, Y.; Cavagnero, S. Sensitivity Enhancement in Solution NMR: Emerging Ideas and New Frontiers. *Journal of Magnetic Resonance* **2014**, *241* (1), 18–31. https://doi.org/10.1016/j.jmr.2014.01.005.

(30) Eills, J.; Budker, D.; Cavagnero, S.; Chekmenev, E. Y.; Elliott, S. J.; Jannin, S.; Lesage, A.; Matysik, J.; Meersmann, T.; Prisner, T.; Reimer, J. A.; Yang, H.; Koptyug, I. V. Spin Hyperpolarization in Modern Magnetic Resonance. *Chemical Reviews*. American Chemical Society February 22, **2023**, pp 1417–1551. https://doi.org/10.1021/acs.chemrev.2c00534.

(31) Nikolaou, P.; Goodson, B. M.; Chekmenev, E. Y. NMR Hyperpolarization Techniques for Biomedicine. *Chemistry - A European Journal* **2015**, *21* (8), 3156–3166. https://doi.org/10.1002/chem.201405253.

(32) Green, R. A.; Adams, R. W.; Duckett, S. B.; Mewis, R. E.; Williamson, D. C.; Green, G. G. R. The Theory and Practice of Hyperpolarization in Magnetic Resonance Using

Parahydrogen. *Prog Nucl Magn Reson Spectrosc* **2012**, *67*, 1–48. https://doi.org/10.1016/j.pnmrs.2012.03.001.

(33) Abraham, M.; McCausland, M. A. H.; Robinson, F. N. H. Dynamic Nuclear Polarization. *Phys Rev Lett* **1959**, *2* (11), 449–451. https://doi.org/10.1103/PhysRevLett.2.449

(34) Cox, S. F. J.; Read, S. F. J.; Th, W.; Cox, S. F. J.; Bouffard, V.; Goldman, M.; Atsarkin, V. A. Principles of Dynamic Nuclear Polarisation. **1978**.

(35) Serrao, E. M.; Brindle, K. M. Dynamic Nuclear Polarisation: The Future of Imaging in Oncology? *Porto Biomed J* **2017**, *2* (3), 71–75. https://doi.org/10.1016/j.pbj.2017.01.002.

(36) Lilly Thankamony, A. S.; Wittmann, J. J.; Kaushik, M.; Corzilius, B. Dynamic Nuclear Polarization for Sensitivity Enhancement in Modern Solid-State NMR. *Prog Nucl Magn Reson Spectrosc* **2017**, *102–103*, 120–195. https://doi.org/10.1016/j.pnmrs.2017.06.002.

(37) Pinon, A. C.; Capozzi, A.; Ardenkjær-Larsen, J. H. Hyperpolarized Water through Dissolution Dynamic Nuclear Polarization with UV-Generated Radicals. *Commun Chem* **2020**, *3* (1), 1–9. https://doi.org/10.1038/s42004-020-0301-6.

(38) Min, H.; Sekar, G.; Hilty, C. Polarization Transfer from Ligands Hyperpolarized by Dissolution Dynamic Nuclear Polarization for Screening in Drug Discovery. *ChemMedChem* **2015**, *10* (9), 1559–1563. https://doi.org/10.1002/cmdc.201500241.

(39) Rosay, M.; Lansing, J. C.; Haddad, K. C.; Bachovchin, W. W.; Herzfeld, J.; Temkin, R. J.; Griffin, R. G. High-Frequency Dynamic Nuclear Polarization in MAS Spectra of Membrane and Soluble Proteins. **2003**, 13626–13627.

(40) Abragam, A.; Goldman, M. Principles of Dynamic Nuclear Polarisation. *Reports on Progress in Physics* **1978**, *41* (3), 395–467. https://doi.org/10.1088/0034-4885/41/3/002.

(41) Albers, M. J.; Bok, R.; Chen, A. P.; Cunningham, C. H.; Zierhut, M. L.; Zhang, V. Y.; Kohler, S. J.; Tropp, J.; Hurd, R. E.; Yen, Y. F.; Nelson, S. J.; Vigneron, D. B.; Kurhanewicz, J. Hyperpolarized 13C Lactate, Pyruvate, and Alanine: Noninvasive Biomarkers for Prostate Cancer Detection and Grading. *Cancer Res* **2008**, *68* (20), 8607–8615. https://doi.org/10.1158/0008-5472.CAN-08-0749.

(42) Miloushev, V. Z.; Granlund, K. L.; Boltyanskiy, R.; Lyashchenko, S. K.; DeAngelis, L. M.; Mellinghoff, I. K.; Brennan, C. W.; Tabar, V.; Yang, T. J.; Holodny, A. I.; Sosa, R. E.; Guo, Y. W. W.; Chen, A. P.; Tropp, J.; Robb, F.; Keshari, K. R. Metabolic Imaging of the Human Brain with Hyperpolarized 13C Pyruvate Demonstrates 13C Lactate Production in Brain Tumor Patients. *Cancer Res* **2018**, *78* (14), 3755–3760. https://doi.org/10.1158/0008-5472.CAN-18-0221.

(43) Walker, T. G. Fundamentals of Spin-Exchange Optical Pumping. *J Phys Conf Ser* **2011**, *294* (1). https://doi.org/10.1088/1742-6596/294/1/012001.

(44) Birchall, J. R.; Nikolaou, P.; Irwin, R. K.; Barlow, M. J.; Ranta, K.; Coffey, A. M.; Goodson, B. M.; Pokochueva, E. V.; Kovtunov, K. V.; Koptyug, I. V.; Chekmenev, E. Y. Helium-Rich Mixtures for Improved Batch-Mode Clinical-Scale Spin-Exchange Optical Pumping of Xenon-129. *Journal of Magnetic Resonance* **2020**, *315*, 106739. https://doi.org/10.1016/j.jmr.2020.106739.

(45) Khan, A. S.; Harvey, R. L.; Birchall, J. R.; Irwin, R. K.; Nikolaou, P.; Schrank, G.; Emami, K.; Dummer, A.; Barlow, M. J.; Goodson, B. M.; Chekmenev, E. Y. Enabling Clinical Technologies for Hyperpolarized 129Xenon Magnetic Resonance Imaging and Spectroscopy. *Angewandte Chemie - International Edition*. John Wiley and Sons Inc October 4, **2021**, pp 22126–22147. https://doi.org/10.1002/anie.202015200.

(46) Heisenberg, W. Mehrkorperprobleme Und Resonanz. **1985**, *267* (1927), 1926–1927.

(47) Kronig, R. de L. Zur Deutung Der Bandenspektren. *Zeitschrift für Physik* **1928**, *46* (11–12), 814–825. https://doi.org/10.1007/BF01391018.

(48) Dennison, David. M. A Note on the Specific Heat of the Hydrogen Molecule. *Proceedings of the Royal Society A* **1927**, *42*, 483–486.

(49) Harteck, P.; Bonhoeffer, K. F. Experimente Über Para- Und Orthowasserstoff. *Naturwisseaschaften* **1929**, No. 17, 182.

(50) Pauli, W. Exclusion Principle and Quantum Mechanics. *Writings on Physics and Philosophy* **1994**, *11* (1923), 165–181. https://doi.org/10.1007/978-3-662-02994-7_20.

(51) Born, M.; Oppenheimer, R. J. On the Quantum Theory of Molecules (English Translation). *Ann Phys* **1927**, *84* (1927), 457.

(52) Atkins, P.; de Paula, J.; Keeler, J. *Physical Chemistry*, 11th edition.; Oxford University Press: Oxford, UK, **2018**.

(53) Serway, A. R.; Moses, J. C.; Moyer, A. C. *Modern Physics*, 3rd Editio.; Thomson Learning Academic Resource Center: Belmont, CA, USA., **2005**.

(54) Friedrich, B. A Paramount Problem Solved at Last: Paramagnetic Catalysis of Ortho-para Hydrogen Conversion. *Natural Sciences* **2021**, *1* (1), 1–3. https://doi.org/10.1002/ntls.10004.

(55) Schmauch A H Singleton, G. E. *Technical Aspects Of Ortho-Parahydrogen Conversion*; UTC, **2025**; Vol. 12. https://pubs.acs.org/sharingguidelines.

(56) Ren, J.; Dyosiba, X.; Musyoka, N. M.; Langmi, H. W.; Mathe, M. Development of Functional Metal-Organic Frameworks (MOFs) for Storing Hydrogen in Para Form. *Procedia Manuf* **2017**, *7*, 34–38. https://doi.org/10.1016/j.promfg.2016.12.012.

(57) Al Ghafri, S. Z.; Munro, S.; Cardella, U.; Funke, T.; Notardonato, W.; Trusler, J. P. M.; Leachman, J.; Span, R.; Kamiya, S.; Pearce, G.; Swanger, A.; Rodriguez, E. D.; Bajada, P.; Jiao, F.; Peng, K.; Siahvashi, A.; Johns, M. L.; May, E. F. Hydrogen Liquefaction: A Review of the Fundamental Physics, Engineering Practice and Future Opportunities. *Energy and Environmental Science*. Royal Society of Chemistry April 21, **2022**, pp 2690–2731. https://doi.org/10.1039/d2ee00099g.

(58) Xu, P.; Wen, J.; Li, K.; Wang, S.; Li, Y. Review of the Continuous Catalytic Ortho-Para Hydrogen Conversion Technology for Hydrogen Liquefaction. *International Journal of Hydrogen Energy*. Elsevier Ltd April 10, **2024**, pp 473–487. https://doi.org/10.1016/j.ijhydene.2024.03.085.

(59) Ilisca, E. Hydrogen Conversion in Nanocages. *Hydrogen* **2021**, *2* (2), 160–206. https://doi.org/10.3390/hydrogen2020010.

(60) Hövener, J. B.; Bär, S.; Leupold, J.; Jenne, K.; Leibfritz, D.; Hennig, J.; Duckett, S. B.; Von Elverfeldt, D. A Continuous-Flow, High-Throughput, High-Pressure Parahydrogen Converter for Hyperpolarization in a Clinical Setting. *NMR Biomed* **2013**, *26* (2), 124–131. https://doi.org/10.1002/nbm.2827.

(61) Chapman, B.; Joalland, B.; Meersman, C.; Ettedgui, J.; Swenson, R. E.; Krishna, M. C.; Nikolaou, P.; Kovtunov, K. V.; Salnikov, O. G.; Koptyug, I. V.; Gemeinhardt, M. E.; Goodson, B. M.; Shchepin, R. V.; Chekmenev, E. Y. Low-Cost High-Pressure Clinical-Scale 50% Parahydrogen Generator Using Liquid Nitrogen at 77 K. *Anal Chem* **2021**, *93* (24), 8476–8483. https://doi.org/10.1021/acs.analchem.1c00716.

(62) Cimenti, M.; Hill, J. M. Direct Utilization of Liquid Fuels in SOFC for Portable Applications: Challenges for the Selection of Alternative Anodes. *Energies (Basel)* **2009**, *2* (2), 377–410. https://doi.org/10.3390/en20200377.

(63) Bowers, C. R.; Weitekamp, D. P. Transformation of Symmetrization Order to Nuclear-Spin Magnetization by Chemical Reaction and Nuclear Magnetic Resonance. *Phys Rev Lett* **1986**, *57* (21), 2645–2648. https://doi.org/10.1103/PhysRevLett.57.2645.

(64) Ward, H. R.; Lawler, R. G.; Fischer, H.; Bargon, J.; Ward, H.; Acc ; Kaptein, R.; Oosterhoff, L.; Closs, G. L. *Parahydrogen-Induced Polarization: A New Spin on Reactions with Hz*; **1991**; Vol. 24. https://pubs.acs.org/sharingguidelines.

(65) Bowers, Russell. C.; Weitekamp, D. P. Parahydrogen and Synthesis Allow Dramatically Enhanced Nuclear Alignment. *J Am Chem Soc* **1987**, *109*, 5541–5542.

(66) Pravica, Michael. G.; Weitekamp, Daniel. P. Net Nmr Alignment By Adiabatic Transport Of Parahydrogen Addition Products To High Magnetic Field. *Chem Phys Lett* **1987**, *145* (4).

(67) Barskiy, D. A.; Knecht, S.; Yurkovskaya, A. V.; Ivanov, K. L. SABRE: Chemical Kinetics and Spin Dynamics of the Formation of Hyperpolarization. *Prog Nucl Magn Reson Spectrosc* **2019**, *114–115*, 33–70. https://doi.org/10.1016/j.pnmrs.2019.05.005.

(68) Messerle, B. a; Sleigh, C. J.; Partridge, G.; Duckett, S. B. Advanced NMR Studies with Para -Hydrogen Induced Polarisation. **2006**, 1429–1435.

(69) Duckett, Simon. B.; Eisenberg, R. Observation of H2 Oxidative Addition to Chlorocarbonylbis(Triphenylphosphne)Rhodium(I) Using Parahydrogen-Induced Polarization. *J Am Chem Soc* **1993**, No. 115, 5292–5293.

(70) Duckett, S. B.; Blazina, D. The Study of Inorganic Systems by NMR Spectroscopy in Conjunction with Parahydrogen-Induced Polarisation. *Eur J Inorg Chem* **2003**, No. 16, 2901–2912. https://doi.org/10.1002/ejic.200300119.

(71) Duckett, S. B.; Sleigh, C. J. Applications of the Parahydrogen Phenomenon: A Chemical Perspective. *Prog Nucl Magn Reson Spectrosc* **1999**, *34* (1), 71–92. https://doi.org/10.1016/S0079-6565(98)00027-2.

(72) Hasnip, S.; Duckett, S. B.; Taylor, D. R.; Taylor, M. J. Parahydrogen Enhanced NMR Studies on Thermally and Photochemically Generated Products from [IrH3(CO)(PPh3)2]. *Chemical Communications* **1998**, *3* (8), 923–924. https://doi.org/10.1039/a801224e.

(73) Buljubasich, L.; Franzoni, M. B.; Spiess, H. W.; Münnemann, K. Level Anti-Crossings in ParaHydrogen Induced Polarization Experiments with Cs-Symmetric Molecules. *Journal of Magnetic Resonance* **2012**, *219*, 33–40. https://doi.org/10.1016/j.jmr.2012.03.020.

(74) Golman, K.; Axelsson, O.; Jóhannesson, H.; Månsson, S.; Olofsson, C.; Petersson, J. S. Parahydrogen-Induced Polarization in Imaging: Subsecond 13C Angiography. *Magn Reson Med* **2001**, *46* (1), 1–5. https://doi.org/10.1002/mrm.1152.

(75) Haake, M.; Natterer, J.; Bargon, J. Efficient NMR Pulse Sequences to Transfer the Parahydrogen-Induced Polarization to Hetero Nuclei. *J Am Chem Soc* **1996**, *118* (36), 8688–8691. https://doi.org/10.1021/ja960067f.

(76) Goldman, M.; Jóhannesson, H. Conversion de l'ordre Para d'une Paire de Protons En Polarisation de 13C Par Irradiation Rf, Pour Utilisation En IRM. *C R Phys* **2005**, *6* (4-5 SPEC. ISS.), 575–581. https://doi.org/10.1016/j.crhy.2005.03.002.

(77) Roth, M.; Koch, A.; Kindervater, P.; Bargon, J.; Spiess, H. W.; Münnemann, K. 13C Hyperpolarization of a Barbituric Acid Derivative via Parahydrogen Induced Polarization.

Journal of Magnetic Resonance **2010**, *204* (1), 50–55. https://doi.org/10.1016/j.jmr.2010.01.016.

(78) Harthun, A.; Selke, R.; Bargon, J. Proof of a Reversible, Pairwise Hydrogen Transfer during the Homogeneously Rhodium(1)- Catalyzed Hydrogenation of A$-Unsaturated Carbonic Acid Derivatives with In Situ NMR Spectroscopy and Parahydrogen. *Angewandte Chemie International Edition* **1996**, *35* (21), 2505–2507.

(79) Emondts, M.; Schikowski, D.; Klankermayer, J.; Schleker, P. P. M. Non-Pairwise Interactions in Parahydrogen Experiments: Nuclear Exchange of Single Protons Enables Bulk Water Hyperpolarization. *ChemPhysChem* **2018**, *19* (20), 2614–2620. https://doi.org/10.1002/cphc.201800521.

(80) Fox, D. J.; Duckett, S. B.; Flaschenriem, C.; Brennessel, W. W.; Schneider, J.; Gunay, A.; Eisenberg, R. A Model Iridium Hydroformylation System with the Large Bite Angle Ligand Xantphos: Reactivity with Parahydrogen and Implications for Hydroformylation Catalysis. *Inorg Chem* **2006**, *45* (18), 7197–7209. https://doi.org/10.1021/ic0607311.

(81) Permin, A. B.; Eisenberg, R. One-Hydrogen Polarization in Hydroformylation Promoted by Platinum-Tin and Iridium Carbonyl Complexes: A New Type of Parahydrogen-Induced Effect. *J Am Chem Soc* **2002**, *124* (42), 12406–12407. https://doi.org/10.1021/ja026698t.

(82) Cavallari, E.; Carrera, C.; Sorge, M.; Bonne, G.; Muchir, A.; Aime, S.; Reineri, F. The 13C Hyperpolarized Pyruvate Generated by ParaHydrogen Detects the Response of the Heart to Altered Metabolism in Real Time. *Sci Rep* **2018**, *8* (1), 2–10. https://doi.org/10.1038/s41598-018-26583-2.

(83) Cavallari, E.; Carrera, C.; Aime, S.; Reineri, F. Studies to Enhance the Hyperpolarization Level in PHIP-SAH-Produced C13-Pyruvate. *Journal of Magnetic Resonance* **2018**, *289*, 12–17. https://doi.org/10.1016/j.jmr.2018.01.019.

(84) Cavallari, E.; Carrera, C.; Di Matteo, G.; Bondar, O.; Aime, S.; Reineri, F. In-Vitro NMR Studies of Prostate Tumor Cell Metabolism by Means of Hyperpolarized [1-13C]Pyruvate Obtained Using the PHIP-SAH Method. *Front Oncol* **2020**, *10* (April), 1–9. https://doi.org/10.3389/fonc.2020.00497.

(85) Atkinson, K. D.; Cowley, M. J.; Duckett, S. B.; Elliott, P. I. P.; Green, G. G. R.; López-Serrano, J.; Khazal, I. G.; Whitwood, A. C. Para-Hydrogen Induced Polarization without Incorporation of Para-Hydrogen into the Analyte. *Inorg Chem* **2009**, *48* (2), 663–670. https://doi.org/10.1021/ic8020029.

(86) Atkinson, K. D.; Cowley, M. J.; Elliott, P. I. P.; Duckett, S. B.; Green, G. G. R.; López-Serrano, J.; Whitwood, A. C. Spontaneous Transfer of Parahydrogen Derived Spin Order to Pyridine at Low Magnetic Field. *J Am Chem Soc* **2009**, *131* (37), 13362–13368. https://doi.org/10.1021/ja903601p.

(87) Adams, R. W.; Aguilar, J. A.; Atkinson, K. D.; Cowley, M. J.; Elliott, P. I. P.; Duckett, S. B.; Green, G. G. R.; Khazal, i. G.; Lopez-Serrano, J.; Williamson, D. C. Reversible Interactions with Para-Hydrogen Enhance NMR Sensitivity by Polarization Transfer. *Science (1979)* **2009**, *323* (March), 1708–1711.

(88) Mewis, R. E. Developments and Advances Concerning the Hyperpolarisation Technique SABRE. *Magnetic Resonance in Chemistry*. John Wiley and Sons Ltd October 1, **2015**, pp 789–800. https://doi.org/10.1002/mrc.4280.

(89) Kovtunov, K. V.; Pokochueva, E. V.; Salnikov, O. G.; Cousin, S. F.; Kurzbach, D.; Vuichoud, B.; Jannin, S.; Chekmenev, E. Y.; Goodson, B. M.; Barskiy, D. A.; Koptyug, I. V. Hyperpolarized NMR Spectroscopy: D-DNP, PHIP, and SABRE Techniques. *Chem Asian J* **2018**, *13* (15), 1857–1871. https://doi.org/10.1002/asia.201800551.

(90) Tomhon, P.; Abdulmojeed, M.; Adelabu, I.; Nantogma, S.; Kabir, M. S. H.; Lehmkuhl, S.; Chekmenev, E. Y.; Theis, T. Temperature Cycling Enables Efficient 13C SABRE-SHEATH Hyperpolarization and Imaging of [1-13C]-Pyruvate. *J Am Chem Soc* **2022**, *144* (1), 282–287. https://doi.org/10.1021/jacs.1c09581.

(91) Adelabu, I.; TomHon, P.; Kabir, M. S. H.; Nantogma, S.; Abdulmojeed, M.; Mandzhieva, I.; Ettedgui, J.; Swenson, R. E.; Krishna, M. C.; Theis, T.; Goodson, B. M.; Chekmenev, E. Y. Order-Unity 13C Nuclear Polarization of [1-13C]Pyruvate in Seconds and the Interplay of Water and SABRE Enhancement. *ChemPhysChem* **2022**, *23* (2). https://doi.org/10.1002/cphc.202100839.

(92) Zhou, Z.; Yu, J.; Colell, J. F. P.; Laasner, R.; Logan, A.; Barskiy, D. A.; Shchepin, R. V.; Chekmenev, E. Y.; Blum, V.; Warren, W. S.; Theis, T. Long-Lived 13C2 Nuclear Spin States Hyperpolarized by Parahydrogen in Reversible Exchange at Microtesla Fields. *Journal of Physical Chemistry Letters* **2017**, *8* (13), 3008–3014. https://doi.org/10.1021/acs.jpclett.7b00987.

(93) Adelabu, I.; Chowdhury, M. R. H.; Nantogma, S.; Oladun, C.; Ahmed, F.; Stilgenbauer, L.; Sadagurski, M.; Theis, T.; Goodson, B. M.; Chekmenev, E. Y. Efficient SABRE-SHEATH Hyperpolarization of Potent Branched-Chain-Amino-Acid Metabolic Probe [1-13C]Ketoisocaproate. *Metabolites* **2023**, *13* (2). https://doi.org/10.3390/metabo13020200.

(94) Schmidt, A. B.; De Maissin, H.; Adelabu, I.; Nantogma, S.; Ettedgui, J.; Tomhon, P.; Goodson, B. M.; Theis, T.; Chekmenev, E. Y. Catalyst-Free Aqueous Hyperpolarized [1-13C]Pyruvate Obtained by Re-Dissolution Signal Amplification by Reversible Exchange. *ACS Sens* **2022**, *7* (11), 3430–3439. https://doi.org/10.1021/acssensors.2c01715.

(95) Tickner, B. J.; Rayner, P. J.; Duckett, S. B. Using SABRE Hyperpolarized 13C NMR Spectroscopy to Interrogate Organic Transformations of Pyruvate. *Anal Chem* **2020**, *92* (13), 9095–9103. https://doi.org/10.1021/acs.analchem.0c01334.

(96) Pravdivtsev, A. N.; Buckenmaier, K.; Kempf, N.; Stevanato, G.; Scheffler, K.; Engelmann, J.; Plaumann, M.; Koerber, R.; Hövener, J. B.; Theis, T. LIGHT-SABRE Hyperpolarizes 1-13C-Pyruvate Continuously without Magnetic Field Cycling. *Journal of Physical Chemistry C* **2023**, *127* (14), 6744–6753. https://doi.org/10.1021/acs.jpcc.3c01128.

(97) Adelabu, I.; Ettedgui, J.; Joshi, S. M.; Nantogma, S.; Chowdhury, M. R. H.; McBride, S.; Theis, T.; Sabbasani, V. R.; Chandrasekhar, M.; Sail, D.; Yamamoto, K.; Swenson, R. E.; Krishna, M. C.; Goodson, B. M.; Chekmenev, E. Y. Rapid 13C Hyperpolarization of the TCA Cycle Intermediate α-Ketoglutarate via SABRE-SHEATH. *Anal Chem* **2022**, *94* (39), 13422–13431. https://doi.org/10.1021/acs.analchem.2c02160.

(98) Shchepin, R. V.; Barskiy, D. A.; Coffey, A. M.; Theis, T.; Shi, F.; Warren, W. S.; Goodson, B. M.; Chekmenev, E. Y. 15N Hyperpolarization of Imidazole-15N2 for Magnetic Resonance PH Sensing via SABRE-SHEATH. *ACS Sens* **2016**, *1* (6), 640–644. https://doi.org/10.1021/acssensors.6b00231.

(99) Truong, M. L.; Theis, T.; Coffey, A. M.; Shchepin, R. V.; Waddell, K. W.; Shi, F.; Goodson, B. M.; Warren, W. S.; Chekmenev, E. Y. 15N Hyperpolarization by Reversible

Exchange Using SABRE-SHEATH. *Journal of Physical Chemistry C* **2015**, *119* (16), 8786–8797. https://doi.org/10.1021/acs.jpcc.5b01799.

(100) Shchepin, R. V.; Barskiy, D. A.; Mikhaylov, D. M.; Chekmenev, E. Y. Efficient Synthesis of Nicotinamide-1-15N for Ultrafast NMR Hyperpolarization Using Parahydrogen. *Bioconjug Chem* **2016**, *27* (4), 878–882. https://doi.org/10.1021/acs.bioconjchem.6b00148.

(101) Barskiy, D. A.; Shchepin, R. V.; Coffey, A. M.; Theis, T.; Warren, W. S.; Goodson, B. M.; Chekmenev, E. Y. Over 20% 15N Hyperpolarization in under One Minute for Metronidazole, an Antibiotic and Hypoxia Probe. *J Am Chem Soc* **2016**, *138* (26), 8080–8083. https://doi.org/10.1021/jacs.6b04784.

(102) MacCulloch, K.; Browning, A.; Tomhon, P.; Lehmkuhl, S.; Chekmenev, E. Y.; Theis, T. Parahydrogen in Reversible Exchange Induces Long-Lived 15N Hyperpolarization of Anticancer Drugs Anastrozole and Letrozole. *Anal Chem* **2023**, *95* (20), 7822–7829. https://doi.org/10.1021/acs.analchem.2c04817.

(103) Knecht, S.; Kiryutin, A. S.; Yurkovskaya, A. V.; Ivanov, K. L. Efficient Conversion of Anti-Phase Spin Order of Protons into 15N Magnetisation Using SLIC-SABRE. *Mol Phys* **2019**, *117* (19), 2762–2771. https://doi.org/10.1080/00268976.2018.1515999.

(104) Shchepin, R. V.; Goodson, B. M.; Theis, T.; Warren, W. S.; Chekmenev, E. Y. Toward Hyperpolarized 19F Molecular Imaging via Reversible Exchange with Parahydrogen. *ChemPhysChem* **2017**, *18* (15), 1961–1965. https://doi.org/10.1002/cphc.201700594.

(105) Olaru, A. M.; Robertson, T. B. R.; Lewis, J. S.; Antony, A.; Iali, W.; Mewis, R. E.; Duckett, S. B. Extending the Scope of 19F Hyperpolarization through Signal

Amplification by Reversible Exchange in MRI and NMR Spectroscopy. *ChemistryOpen* **2018**, *7* (1), 97–105. https://doi.org/10.1002/open.201700166.

(106) Burns, M. J.; Rayner, P. J.; Green, G. G. R.; Highton, L. A. R.; Mewis, R. E.; Duckett, S. B. Improving the Hyperpolarization of 31P Nuclei by Synthetic Design. *Journal of Physical Chemistry B* **2015**, *119* (15), 5020–5027. https://doi.org/10.1021/acs.jpcb.5b00686.

(107) Zhivonitko, V. V.; Skovpin, I. V.; Koptyug, I. V. Strong 31P Nuclear Spin Hyperpolarization Produced via Reversible Chemical Interaction with Parahydrogen. *Chemical Communications* **2015**, *51* (13), 2506–2509. https://doi.org/10.1039/c4cc08115c.

(108) Olaru, A. M.; Burt, A.; Rayner, P. J.; Hart, S. J.; Whitwood, A. C.; Green, G. G. R.; Duckett, S. B. Using Signal Amplification by Reversible Exchange (SABRE) to Hyperpolarise 119Sn and 29Si NMR Nuclei. *Chemical Communications* **2016**, *52* (100), 14482–14485. https://doi.org/10.1039/c6cc07109k.

(109) Rayner, P. J.; Duckett, S. B. Signal Amplification by Reversible Exchange (SABRE): From Discovery to Diagnosis. *Angewandte Chemie - International Edition* **2018**, *57* (23), 6742–6753. https://doi.org/10.1002/anie.201710406.

(110) Tickner, B. J.; Zhivonitko, V. V. Advancing Homogeneous Catalysis for Parahydrogen-Derived Hyperpolarisation and Its NMR Applications. *Chemical Science*. Royal Society of Chemistry March 22, **2022**, pp 4670–4696. https://doi.org/10.1039/d2sc00737a.

(111) Salnikov, O. G.; Assaf, C. D.; Yi, A. P.; Duckett, S. B.; Chekmenev, E. Y.; Hövener, J. B.; Koptyug, I. V.; Pravdivtsev, A. N. Modeling Ligand Exchange Kinetics in Iridium

Complexes Catalyzing SABRE Nuclear Spin Hyperpolarization. *Anal Chem* **2024**, *96* (29), 11790–11799. https://doi.org/10.1021/acs.analchem.4c01374.

(112) Mewis, R. E. Developments and Advances Concerning the Hyperpolarisation Technique SABRE. *Magnetic Resonance in Chemistry*. John Wiley and Sons Ltd October 1, **2015**, pp 789–800. https://doi.org/10.1002/mrc.4280.

(113) Barskiy, D. A.; Pravdivtsev, A. N.; Ivanov, K. L.; Kovtunov, K. V.; Koptyug, I. V. A Simple Analytical Model for Signal Amplification by Reversible Exchange (SABRE) Process. *Physical Chemistry Chemical Physics* **2016**, *18* (1), 89–93. https://doi.org/10.1039/c5cp05134g.

(114) Lin, K.; TomHon, P.; Lehmkuhl, S.; Laasner, R.; Theis, T.; Blum, V. Density Functional Theory Study of Reaction Equilibria in Signal Amplification by Reversible Exchange. *ChemPhysChem* **2021**, *22* (19), 1947–1957. https://doi.org/10.1002/cphc.202100204.

(115) Tickner, B. J.; John, R. O.; Roy, S. S.; Hart, S. J.; Whitwood, A. C.; Duckett, S. B. Using Coligands to Gain Mechanistic Insight into Iridium Complexes Hyperpolarized with: Para-Hydrogen. *Chem Sci* **2019**, *10* (20), 5235–5245. https://doi.org/10.1039/c9sc00444k.

(116) Cowley, M. J.; Adams, R. W.; Atkinson, K. D.; Cockett, M. C. R.; Duckett, S. B.; Green, G. G. R.; Lohman, J. A. B.; Kerssebaum, R.; Kilgour, D.; Mewis, R. E. Iridium N-Heterocyclic Carbene Complexes as Efficient Catalysts for Magnetization Transfer from Para -Hydrogen. *J Am Chem Soc* **2011**, *133* (16), 6134–6137. https://doi.org/10.1021/ja200299u.

(117) Barskiy, D. A.; Knecht, S.; Yurkovskaya, A. V.; Ivanov, K. L. SABRE: Chemical Kinetics and Spin Dynamics of the Formation of Hyperpolarization. *Progress in Nuclear*

Magnetic Resonance Spectroscopy. Elsevier B.V. October 1, **2019**, pp 33–70. https://doi.org/10.1016/j.pnmrs.2019.05.005.

(118) van Weerdenburg, B. J. A.; Glöggler, S.; Eshuis, N.; Engwerda, A. H. T.; Smits, J. M. M.; de Gelder, R.; Appelt, S.; Wymenga, S. S.; Tessari, M.; Feiters, M. C.; Blümich, B.; Rutjes, F. P. J. T. Ligand Effects of NHC–Iridium Catalysts for Signal Amplification by Reversible Exchange (SABRE). *Chemical Communications* **2013**, *49* (67), 7388–7390. https://doi.org/10.1039/c3cc43423k.

(119) Hillier, A. C.; Sommer, W. J.; Yong, B. S.; Petersen, J. L.; Cavallo, L.; Nolan, S. P. A Combined Experimental and Theoretical Study Examining the Binding of N-Heterocyclic Carbenes (NHC) to the Cp*RuCl (Cp* = H5-C5Me5) Moiety: Insight into Stereoelectronic Differences between Unsaturated and Saturated NHC Ligands. *Organometallics* **2003**, *22* (21), 4322–4326. https://doi.org/10.1021/om034016k.

(120) Clavier, H.; Nolan, S. P. Percent Buried Volume for Phosphine and N-Heterocyclic Carbene Ligands: Steric Properties in Organometallic Chemistry. *Chemical Communications*. Royal Society of Chemistry **2010**, pp 841–861. https://doi.org/10.1039/b922984a.

(121) Tolman, C. A. *Steric Effects of Phosphorus Ligands in Organometallic Chemistry and Homogeneous Catalysis*^. https://pubs.acs.org/sharingguidelines.

(122) Kelly, R. A.; Clavier, H.; Giudice, S.; Scott, N. M.; Stevens, E. D.; Bordner, J.; Samardjiev, I.; Hoff, C. D.; Cavallo, L.; Nolan, S. P. Determination of N-Heterocyclic Carbene (NHC) Steric and Electronic Parameters Using the [(NHC)Ir(CO)2Cl] System. *Organometallics* **2008**, *27* (2), 202–210. https://doi.org/10.1021/om701001g.

(123) Zhao, Y.; Gilbertson, S. R. Synthesis of Proline-Based N - Heterocyclic Carbene Ligands. *Org Lett* **2014**, No. 16, 1033–1035.

(124) Wong, C. M.; Fekete, M.; Nelson-Forde, R.; Gatus, M. R. D.; Rayner, P. J.; Whitwood, A. C.; Duckett, S. B.; Messerle, B. A. Harnessing Asymmetric N-Heterocyclic Carbene Ligands to Optimise SABRE Hyperpolarisation. *Catal Sci Technol* **2018**, *8* (19), 4925–4933. https://doi.org/10.1039/c8cy01214h.

(125) Hadjiali, S.; Savka, R.; Plaumann, M.; Bommerich, U.; Bothe, S.; Gutmann, T.; Ratajczyk, T.; Bernarding, J.; Limbach, H. H.; Plenio, H.; Buntkowsky, G. Substituent Influences on the NMR Signal Amplification of Ir Complexes with Heterocyclic Carbene Ligands. *Appl Magn Reson* **2019**, *50* (7), 895–902. https://doi.org/10.1007/s00723-019-01115-x.

(126) Rayner, P. J., Norcott, P., Appleby, K. M., Iali, W., John, R. O., Hart, S. J., Whitwood, A. C., & Duckett, S. B. (2018). Fine-tuning the efficiency of para-hydrogen-induced hyperpolarization by rational N-heterocyclic carbene design. *Nature Communications*, *9*(1). https://doi.org/10.1038/s41467-018-06766-1

(127) Pham, P.; Hilty, C. Tunable Iridium Catalyst Designs with Bidentate N-Heterocyclic Carbene Ligands for SABRE Hyperpolarization of Sterically Hindered Substrates. *Chemical Communications* **2020**, *56* (98), 15466–15469. https://doi.org/10.1039/d0cc06840c.

(128) Van Weerdenburg, B. J. A.; Eshuis, N.; Tessari, M.; Rutjes, F. P. J. T.; Feiters, M. C. Application of the π-Accepting Ability Parameter of N-Heterocyclic Carbene Ligands in Iridium Complexes for Signal Amplification by Reversible Exchange (SABRE). *Dalton Transactions* **2015**, *44* (35), 15387–15390. https://doi.org/10.1039/c5dt02340h.

(129) Dücker, E. B.; Kuhn, L. T.; Münnemann, K.; Griesinger, C. Similarity of SABRE Field Dependence in Chemically Different Substrates. *Journal of Magnetic Resonance* **2012**, *214*, 159–165. https://doi.org/10.1016/j.jmr.2011.11.001.

(130) Colell, J. F. P.; Logan, A. W. J.; Zhou, Z.; Lindale, J. R.; Laasner, R.; Shchepin, R. V.; Chekmenev, E. Y.; Blum, V.; Warren, W. S.; Malcolmson, S. J.; Theis, T. Rational Ligand Choice Extends the SABRE Substrate Scope. *Chemical Communications* **2020**, *56* (65), 9336–9339. https://doi.org/10.1039/d0cc01330g.

(131) Rayner, P. J.; Gillions, J. P.; Hannibal, V. D.; John, R. O.; Duckett, S. B. Hyperpolarisation of Weakly Binding N-Heterocycles Using Signal Amplification by Reversible Exchange. *Chem Sci* **2021**, *12* (16), 5910–5917. https://doi.org/10.1039/d0sc06907h.

(132) Tickner, B. J.; Borozdina, Y.; Duckett, S. B.; Angelovski, G. Exploring the Hyperpolarisation of EGTA-Based Ligands Using SABRE. *Dalton Transactions* **2021**, *50* (7), 2448–2461. https://doi.org/10.1039/d0dt03839c.

(133) Iali, W.; Roy, S. S.; Tickner, B. J.; Ahwal, F.; Kennerley, A. J.; Duckett, S. B. Hyperpolarising Pyruvate through Signal Amplification by Reversible Exchange (SABRE). *Angewandte Chemie* **2019**, *131* (30), 10377–10381. https://doi.org/10.1002/ange.201905483.

(134) Tickner, B. J.; Semenova, O.; Iali, W.; Rayner, P. J.; Whitwood, A. C.; Duckett, S. B. Optimisation of Pyruvate Hyperpolarisation Using SABRE by Tuning the Active Magnetisation Transfer Catalyst. *Catal Sci Technol* **2020**, *10* (5), 1343–1355. https://doi.org/10.1039/c9cy02498k.

(135) Tickner, B. J.; Duckett, S. B. Iridium Trihydride and Tetrahydride Complexes and Their Role in Catalytic Polarisation Transfer from Parahydrogen to Pyruvate. *Chem Sci* **2024**. https://doi.org/10.1039/d4sc06138a.

(136) Assaf, C. D.; Gui, X.; Auer, A. A.; Duckett, S. B.; Hövener, J. B.; Pravdivtsev, A. N. J Coupling Constants of <1 Hz Enable 13C Hyperpolarization of Pyruvate via Reversible Exchange of Parahydrogen. *Journal of Physical Chemistry Letters* **2024**, *15* (5), 1195–1203. https://doi.org/10.1021/acs.jpclett.3c02980.

(137) Tickner, Ben. J.; Ahwal, F.; Whitwood, A. C.; Duckett, S. B. Reversible Hyperpolarization of Ketoisocaproate Using Sulfoxide-Containing Polarization Transfer Catalysts. *ChemPhysChem* **2021**, *22* (1), 13–17. https://doi.org/https://doi.org/10.1002/cphc.202000825.

(138) Tickner, B. J.; Parker, R. R.; Whitwood, A. C.; Duckett, S. B. Probing the Hydrogenation of Vinyl Sulfoxides Using Para-Hydrogen. *Organometallics* **2019**, *38* (22), 4377–4382. https://doi.org/10.1021/acs.organomet.9b00610.

(139) Tickner, B. J.; Lewis, J. S.; John, R. O.; Whitwood, A. C.; Duckett, S. B. Mechanistic Insight into Novel Sulfoxide Containing SABRE Polarisation Transfer Catalysts. *Dalton Transactions* **2019**, *48* (40), 15198–15206. https://doi.org/10.1039/c9dt02951f.

(140) Mewis, R. E.; Green, R. A.; Cockett, M. C. R.; Cowley, M. J.; Duckett, S. B.; Green, G. G. R.; John, R. O.; Rayner, P. J.; Williamson, D. C. Strategies for the Hyperpolarization of Acetonitrile and Related Ligands by SABRE. *Journal of Physical Chemistry B* **2015**, *119* (4), 1416–1424. https://doi.org/10.1021/jp511492q.

(141) Tanner, C. P. N.; Lindale, J. R.; Eriksson, S. L.; Zhou, Z.; Colell, J. F. P.; Theis, T.; Warren, W. S. Selective Hyperpolarization of Heteronuclear Singlet States via Pulsed

Microtesla SABRE. *Journal of Chemical Physics* **2019**, *151* (4). https://doi.org/10.1063/1.5108644.

(142) Fekete, M.; Ahwal, F.; Duckett, S. B. Remarkable Levels of 15N Polarization Delivered through SABRE into Unlabeled Pyridine, Pyrazine, or Metronidazole Enable Single Scan NMR Quantification at the MM Level. *Journal of Physical Chemistry B* **2020**, *124* (22), 4573–4580. https://doi.org/10.1021/acs.jpcb.0c02583.

(143) Iali, W.; Rayner, P. J.; Alshehri, A.; Holmes, A. J.; Ruddlesden, A. J.; Duckett, S. B. Direct and Indirect Hyperpolarisation of Amines Using: Para Hydrogen. *Chem Sci* **2018**, *9* (15), 3677–3684. https://doi.org/10.1039/c8sc00526e.

(144) McBride, S. J.; Pike, M.; Curran, E.; Zavriyev, A.; Adebesin, B.; Tucker, L.; Harzan, J. M.; Senanayake, I. M.; Shen, S.; Abdulmojeed, M.; Theiss, F.; Boele, T.; Gade, T. P.; Duckett, S.; Goodson, B. M.; Rosen, M. S.; Chekmenev, E. Y.; Yuan, H.; Dedesma, C.; Kadlecek, S.; Theis, T.; TomHon, P. Scalable Hyperpolarized MRI Enabled by Ace-SABRE of [1-13C]Pyruvate. *Angewandte Chemie International Edition* **2025**. https://doi.org/10.1002/anie.202501231.

(145) McBride, S. J.; MacCulloch, K.; TomHon, P.; Browning, A.; Meisel, S.; Abdulmojeed, M.; Goodson, B. M.; Chekmenev, E. Y.; Theis, T. Carbon-13 Hyperpolarization of α-Ketocarboxylates with Parahydrogen in Reversible Exchange. *ChemMedChem* **2024**. https://doi.org/10.1002/cmdc.202400378.

(146) Rayner, P. J.; Fekete, M.; Gater, C. A.; Ahwal, F.; Turner, N.; Kennerley, A. J.; Duckett, S. B. Real-Time High-Sensitivity Reaction Monitoring of Important Nitrogen-Cycle Synthons by 15N Hyperpolarized Nuclear Magnetic Resonance. *J Am Chem Soc* **2022**, *144* (19), 8756–8769. https://doi.org/10.1021/jacs.2c02619.

(147) Moreno, K. X.; Nasr, K.; Milne, M.; Sherry, A. D.; Goux, W. J. Nuclear Spin Hyperpolarization of the Solvent Using Signal Amplification by Reversible Exchange (SABRE). *Journal of Magnetic Resonance* **2015**, *257*, 15–23. https://doi.org/10.1016/j.jmr.2015.04.013.

(148) Zeng, H.; Xu, J.; Gillen, J.; McMahon, M. T.; Artemov, D.; Tyburn, J. M.; Lohman, J. A. B.; Mewis, R. E.; Atkinson, K. D.; Green, G. G. R.; Duckett, S. B.; Van Zijl, P. C. M. Optimization of SABRE for Polarization of the Tuberculosis Drugs Pyrazinamide and Isoniazid. *Journal of Magnetic Resonance* **2013**, *237*, 73–78. https://doi.org/10.1016/j.jmr.2013.09.012.

(149) Iali, W.; Rayner, P. J.; Duckett, S. B. Using Parahydrogen to Hyperpolarize Amines, Amides, Carboxylic Acids, Alcohols, Phosphates, and Carbonates. *Sci Adv* **2018**, *4* (1), 1–7. https://doi.org/10.1126/sciadv.aao6250.

(150) Park, H.; Zhang, G.; Bae, J.; Theis, T.; Warren, W. S.; Wang, Q. Application of 15N2-Diazirines as a Versatile Platform for Hyperpolarization of Biological Molecules by d-DNP. *Bioconjug Chem* **2020**, *31* (3), 537–541. https://doi.org/10.1021/acs.bioconjchem.0c00028.

(151) Colell, J. F. P.; Emondts, M.; Logan, A. W. J.; Shen, K.; Bae, J.; Shchepin, R. V.; Ortiz, G. X.; Spannring, P.; Wang, Q.; Malcolmson, S. J.; Chekmenev, E. Y.; Feiters, M. C.; Rutjes, F. P. J. T.; Blümich, B.; Theis, T.; Warren, W. S. Direct Hyperpolarization of Nitrogen-15 in Aqueous Media with Parahydrogen in Reversible Exchange. *J Am Chem Soc* **2017**, *139* (23), 7761–7767. https://doi.org/10.1021/jacs.7b00569.

(152) Spannring, P.; Reile, I.; Emondts, M.; Schleker, P. P. M.; Hermkens, N. K. J.; van der Zwaluw, N. G. J.; van Weerdenburg, B. J. A.; Tinnemans, P.; Tessari, M.; Blümich, B.;

Rutjes, F. P. J. T.; Feiters, M. C. A New Ir-NHC Catalyst for Signal Amplification by Reversible Exchange in D2O. *Chemistry - A European Journal* **2016**, *22* (27), 9277–9282. https://doi.org/10.1002/chem.201601211.

(153) Fekete, M.; Gibard, C.; Dear, G. J.; Green, G. G. R.; Hooper, A. J. J.; Roberts, A. D.; Cisnetti, F.; Duckett, S. B. Utilisation of Water Soluble Iridium Catalysts for Signal Amplification by Reversible Exchange. *Dalton Transactions* **2015**, *44* (17), 7870–7880. https://doi.org/10.1039/c5dt00311c.

(154) Iali, W.; Olaru, A. M.; Green, G. G. R.; Duckett, S. B. Achieving High Levels of NMR-Hyperpolarization in Aqueous Media With Minimal Catalyst Contamination Using SABRE. *Chemistry - A European Journal* **2017**, *23* (44), 10491–10495. https://doi.org/10.1002/chem.201702716.

(155) Truong, M. L.; Shi, F.; He, P.; Yuan, B.; Plunkett, K. N.; Coffey, A. M.; Shchepin, R. V.; Barskiy, D. A.; Kovtunov, K. V.; Koptyug, I. V.; Waddell, K. W.; Goodson, B. M.; Chekmenev, E. Y. Irreversible Catalyst Activation Enables Hyperpolarization and Water Solubility for NMR Signal Amplification by Reversible Exchange. *Journal of Physical Chemistry B* **2014**, *118* (48), 13882–13889. https://doi.org/10.1021/jp510825b.

(156) Zhao, E. W.; Maligal-Ganesh, R.; Du, Y.; Zhao, T. Y.; Collins, J.; Ma, T.; Zhou, L.; Goh, T. W.; Huang, W.; Bowers, C. R. Surface-Mediated Hyperpolarization of Liquid Water from Parahydrogen. *Chem* **2018**, *4* (6), 1387–1403. https://doi.org/10.1016/j.chempr.2018.03.004.

(157) Ivanov, K. L.; Pravdivtsev, A. N.; Yurkovskaya, A. V.; Vieth, H. M.; Kaptein, R. The Role of Level Anti-Crossings in Nuclear Spin Hyperpolarization. *Prog Nucl Magn Reson Spectrosc* **2014**, *81*, 1–36. https://doi.org/10.1016/j.pnmrs.2014.06.001.

(158) Truong, M. L.; Theis, T.; Coffey, A. M.; Shchepin, R. V.; Waddell, K. W.; Shi, F.; Goodson, B. M.; Warren, W. S.; Chekmenev, E. Y. 15N Hyperpolarization by Reversible Exchange Using SABRE-SHEATH. *Journal of Physical Chemistry C* **2015**, *119* (16), 8786–8797. https://doi.org/10.1021/acs.jpcc.5b01799.

(159) Colell, J. F. P.; Logan, A. W. J.; Zhou, Z.; Shchepin, R. V.; Barskiy, D. A.; Ortiz, G. X.; Wang, Q.; Malcolmson, S. J.; Chekmenev, E. Y.; Warren, W. S.; Theis, T. Generalizing, Extending, and Maximizing Nitrogen-15 Hyperpolarization Induced by Parahydrogen in Reversible Exchange. *Journal of Physical Chemistry C* **2017**, *121* (12), 6626–6634. https://doi.org/10.1021/acs.jpcc.6b12097.

(160) Vaupel, P.; Kallinowski, F.; Okunieff, P. Blood Flow, Oxygen and Nutrient Supply, and Metabolic Microenvironment of Human Tumors: A Review. *Cancer Res* **1989**, *49* (23), 6449–6465.

(161) Tannock, I. F.; Rotin, D. Acid PH in Tumors and Its Potential for Therapeutic Exploitation. *Cancer Res* **1989**, *49* (16), 4373–4384.

(162) Gerweck, L. E.; Seetharaman, K. Cellular PH Gradient in Tumor versus Normal Tissue: Potential Exploitation for the Treatment of Cancer. *Cancer Res* **1996**, *56* (6), 1194–1198.

(163) Griffiths, J. R. *Are Cancer Cells Acidic?*; 1991; Vol. 64.

(164) Lee, S. H.; Griffiths, J. R. How and Why Are Cancers Acidic? Carbonic Anhydrase Ix and the Homeostatic Control of Tumour Extracellular Ph. *Cancers*. MDPI AG June 1, 2020, pp 1–23. https://doi.org/10.3390/cancers12061616.

(165) Thews, O.; Riemann, A. Tumor PH and Metastasis: A Malignant Process beyond Hypoxia. *Cancer and Metastasis Reviews* **2019**, *38* (1–2), 113–129. https://doi.org/10.1007/s10555-018-09777-y.

(166) Martin, G. R.; Jain, R. K. Noninvasive Measurement of Interstitial PH Profiles in Normal and Neoplastic Tissue Using Fluorescence Ratio Imaging Microscopy. *Cancer Res* **1994**, *54* (21), 5670–5674.

(167) Jokivarsi, K. T.; Gröhn, H. I.; Gröhn, O. H.; Kauppinen, R. A. Proton Transfer Ratio, Lactate, and Intracellular PH in Acute Cerebral Ischemia. *Magn Reson Med* **2007**, *57* (4), 647–653. https://doi.org/10.1002/mrm.21181.

(168) Gorodetsky, A. A.; Kirilyuk, I. A.; Khramtsov, V. V.; Komarov, D. A. Functional Electron Paramagnetic Resonance Imaging of Ischemic Rat Heart: Monitoring of Tissue Oxygenation and PH. *Magn Reson Med* **2016**, *76* (1), 350–358. https://doi.org/10.1002/mrm.25867.

(169) Longo, D. L.; Cutrin, J. C.; Michelotti, F.; Irrera, P.; Aime, S. Noninvasive Evaluation of Renal PH Homeostasis after Ischemia Reperfusion Injury by CEST-MRI. *NMR Biomed* **2017**, *30* (7). https://doi.org/10.1002/nbm.3720.

(170) Bruno, C. M.; Valenti, M. Acid-Base Disorders in Patients with Chronic Obstructive Pulmonary Disease: A Pathophysiological Review. *Journal of Biomedicine and Biotechnology*. 2012. https://doi.org/10.1155/2012/915150.

(171) Kurtzman, N. A. Renal Tubular Acidosis Syndromes. *South Med J* **2000**, *93* (11), 1042—1052.

(172) Huber, V.; Camisaschi, C.; Berzi, A.; Ferro, S.; Lugini, L.; Triulzi, T.; Tuccitto, A.; Tagliabue, E.; Castelli, C.; Rivoltini, L. Cancer Acidity: An Ultimate Frontier of Tumor Immune Escape and a Novel Target of Immunomodulation. *Seminars in Cancer Biology*. Academic Press April 1, 2017, pp 74–89. https://doi.org/10.1016/j.semcancer.2017.03.001.

(173) Wang, B. Y.; Zhang, J.; Wang, J. L.; Sun, S.; Wang, Z. H.; Wang, L. P.; Zhang, Q. L.; Lv, F. F.; Cao, E. Y.; Shao, Z. M.; Fais, S.; Hu, X. C. Intermittent High Dose Proton Pump Inhibitor Enhances the Antitumor Effects of Chemotherapy in Metastatic Breast Cancer. *Journal of Experimental and Clinical Cancer Research* **2015**, *34* (1). https://doi.org/10.1186/s13046-015-0194-x.

(174) Nakagawa, Y.; Negishi, Y.; Shimizu, M.; Takahashi, M.; Ichikawa, M.; Takahashi, H. Effects of Extracellular PH and Hypoxia on the Function and Development of Antigen-Specific Cytotoxic T Lymphocytes. *Immunol Lett* **2015**, *167* (2), 72–86. https://doi.org/10.1016/j.imlet.2015.07.003.

(175) Jardim-Perassi, B. V.; Irrera, P.; Oluwatola, O. E.; Abrahams, D.; Estrella, V. C.; Ordway, B.; Byrne, S. R.; Ojeda, A. A.; Whelan, C. J.; Kim, J.; Beatty, M. S.; Damgaci-Erturk, S.; Longo, D. L.; Gaspar, K. J.; Siegers, G. M.; Centeno, B. A.; Lau, J. Y. C.; Pilon-Thomas, S. A.; Ibrahim-Hashim, A.; Gillies, R. J. L-DOS47 Elevates Pancreatic Cancer Tumor PH and Enhances Response to Immunotherapy. *Biomedicines* **2024**, *12* (2). https://doi.org/10.3390/biomedicines12020461.

(176) Irrera, P.; Roberto, M.; Consolino, L.; Anemone, A.; Villano, D.; Navarro-Tableros, V.; Carella, A.; Dastrù, W.; Aime, S.; Longo, D. L. Effect of Esomeprazole Treatment on Extracellular Tumor PH in a Preclinical Model of Prostate Cancer by MRI-CEST Tumor PH Imaging. *Metabolites* **2023**, *13* (1). https://doi.org/10.3390/metabo13010048.

(177) Dhakan, C.; Anemone, A.; Ventura, V.; Carella, A.; Corrado, A.; Pirotta, E.; Villano, D.; Romdhane, F.; Gammaraccio, F.; Aime, S.; Longo, D. L. Assessing the Therapeutic Efficacy of Proton Transport Inhibitors in a Triple-Negative Breast Cancer Murine Model

with Magnetic Resonance Imaging—Chemical Exchange Saturation Transfer Tumor PH Imaging. *Metabolites* **2023**, *13* (11). https://doi.org/10.3390/metabo13111161.

(178) Pilon-Thomas, S.; Kodumudi, K. N.; El-Kenawi, A. E.; Russell, S.; Weber, A. M.; Luddy, K.; Damaghi, M.; Wojtkowiak, J. W.; Mulé, J. J.; Ibrahim-Hashim, A.; Gillies, R. J. Neutralization of Tumor Acidity Improves Antitumor Responses to Immunotherapy. *Cancer Res* **2016**, *76* (6), 1381–1390. https://doi.org/10.1158/0008-5472.CAN-15-1743.

(179) Kim, H.; Krishnamurthy, L. C.; Sun, P. Z. Brain PH Imaging and Its Applications. *Neuroscience* **2021**, *474*, 51–62. https://doi.org/10.1016/j.neuroscience.2021.01.026.

(180) Gillies, R. J.; Raghunand, N.; Garcia-Martin, M. L.; Gatenby, R. A. *PH Imaging A Review of PH Measurement Methods and Applications in Cancers*.

(181) Gillies, R. J.; Raghunand, N.; Garcia-Martin, M. L.; Gatenby, R. A. *PH Imaging*; 2004; Vol. 23. https://doi.org/10.1109/MEMB.2004.1360409.

(182) Anemone, A.; Consolino, L.; Arena, F.; Capozza, M.; Longo, D. L. Imaging Tumor Acidosis: A Survey of the Available Techniques for Mapping in Vivo Tumor PH. *Cancer and Metastasis Reviews* **2019**, *38* (1–2), 25–49. https://doi.org/10.1007/s10555-019-09782-9.

(183) Chen, J.; Hackett, E. P.; Singh, J.; Kovács, Z.; Park, J. M. Simultaneous Assessment of Intracellular and Extracellular PH Using Hyperpolarized [1-13C]Alanine Ethyl Ester. *Anal Chem* **2020**, *92* (17), 11681–11686. https://doi.org/10.1021/acs.analchem.0c01568.

(184) Hashim, A. I.; Zhang, X.; Wojtkowiak, J. W.; Martinez, G. V.; Gillies, R. J. Imaging PH and Metastasis. *NMR Biomed* **2011**, *24* (6), 582–591. https://doi.org/10.1002/nbm.1644.

(185) Gillies, R. J.; Liu, Z.; Bhujwalla, Z. 31P-MRS Measurements of Extracellular PH of Tumors Using 3- Aminopropylphosphonate. *Am J Physiol Cell Physiol* **1994**, *267* (1 36-1). https://doi.org/10.1152/ajpcell.1994.267.1.c195.

(186) García-Martín, M.-L.; Hérigault, G.; Rémy, C.; Farion, R.; Ballesteros, P.; Coles, J. A.; Cerdán, S.; Ziegler, A. Mapping Extracellular PH in Rat Brain Gliomas in Vivo by 1H Magnetic Resonance Spectroscopic Imaging: Comparison with Maps of Metabolites 1. *Cancer Res* **2001**, *61*, 6524–6531.

(187) Chen, L. Q.; Pagel, M. D. Evaluating PH in the Extracellular Tumor Microenvironment Using CEST MRI and Other Imaging Methods. *Adv Radiol* **2015**, *2015*, 1–25. https://doi.org/10.1155/2015/206405.

(188) Gil, S.; Zaderenzo, P.; Cruz, F.; Cerdan, S.; Ballesteros, P. Imidazol-1-Ylalkanoic Acids as Extrinsic 1H NMR Probes for the Determination of Intracellular PH, Extracellular PH and Cell Volume. *Bioorganic & iMedicinal Chemistry* **1994**, *2* (5), 305–314.

(189) Halse, M. E. Perspectives for Hyperpolarisation in Compact NMR. *TrAC - Trends in Analytical Chemistry* **2016**, *83*, 76–83. https://doi.org/10.1016/j.trac.2016.05.004.

(190) Ardenkjaer-Larsen, J. H.; Boebinger, G. S.; Comment, A.; Duckett, S.; Edison, A. S.; Engelke, F.; Griesinger, C.; Griffin, R. G.; Hilty, C.; Maeda, H.; Parigi, G.; Prisner, T.; Ravera, E.; Van Bentum, J.; Vega, S.; Webb, A.; Luchinat, C.; Schwalbe, H.; Frydman, L. Facing and Overcoming Sensitivity Challenges in Biomolecular NMR Spectroscopy. *Angewandte Chemie - International Edition* **2015**, *54* (32), 9162–9185. https://doi.org/10.1002/anie.201410653.

(191) Nikolaou, P.; Goodson, B. M.; Chekmenev, E. Y. NMR Hyperpolarization Techniques for Biomedicine. *Chemistry - A European Journal* **2015**, *21* (8), 3156–3166. https://doi.org/10.1002/chem.201405253.

(192) Korenchan, D. E.; Taglang, C.; Von Morze, C.; Blecha, J. E.; Gordon, J. W.; Sriram, R.; Larson, P. E. Z.; Vigneron, D. B.; Vanbrocklin, H. F.; Kurhanewicz, J.; Wilson, D. M.; Flavell, R. R. Dicarboxylic Acids as PH Sensors for Hyperpolarized 13C Magnetic Resonance Spectroscopic Imaging. *Analyst* **2017**, *142* (9), 1429–1433. https://doi.org/10.1039/c7an00076f.

(193) Düwel, S.; Hundshammer, C.; Gersch, M.; Feuerecker, B.; Steiger, K.; Buck, A.; Walch, A.; Haase, A.; Glaser, S. J.; Schwaiger, A.; Schilling, F. Imaging of PH in Vivo Using Hyperpolarized 13C-Labelled Zymonic Acid. *Nat Commun* **2017**, *8* (May). https://doi.org/10.1038/ncomms15126.

(194) Flavell, R. R.; Von Morze, C.; Blecha, J. E.; Korenchan, D. E.; Van Criekinge, M.; Sriram, R.; Gordon, J. W.; Chen, H. Y.; Subramaniam, S.; Bok, R. A.; Wang, Z. J.; Vigneron, D. B.; Larson, P. E.; Kurhanewicz, J.; Wilson, D. M. Application of Good's Buffers to PH Imaging Using Hyperpolarized 13C MRI. *Chemical Communications* **2015**, *51* (74), 14119–14122. https://doi.org/10.1039/c5cc05348j.

(195) Grashei, M.; Wodtke, P.; Skinner, J. G.; Sühnel, S.; Setzer, N.; Metzler, T.; Gulde, S.; Park, M.; Witt, D.; Mohr, H.; Hundshammer, C.; Strittmatter, N.; Pellegata, N. S.; Steiger, K.; Schilling, F. Simultaneous Magnetic Resonance Imaging of PH, Perfusion and Renal Filtration Using Hyperpolarized 13C-Labelled Z-OMPD. *Nat Commun* **2023**, *14* (1). https://doi.org/10.1038/s41467-023-40747-3.

(196) Theis, T.; Truong, M. L.; Coffey, A. M.; Shchepin, R. V.; Waddell, K. W.; Shi, F.; Goodson, B. M.; Warren, W. S.; Chekmenev, E. Y. Microtesla SABRE Enables 10% Nitrogen-15 Nuclear Spin Polarization. *J Am Chem Soc* **2015**, *137* (4), 1404–1407. https://doi.org/10.1021/ja512242d.

(197) Hövener, J. B.; Pravdivtsev, A. N.; Kidd, B.; Bowers, C. R.; Glöggler, S.; Kovtunov, K. V.; Plaumann, M.; Katz-Brull, R.; Buckenmaier, K.; Jerschow, A.; Reineri, F.; Theis, T.; Shchepin, R. V.; Wagner, S.; Bhattacharya, P.; Zacharias, N. M.; Chekmenev, E. Y. Parahydrogen-Based Hyperpolarization for Biomedicine. *Angewandte Chemie - International Edition* **2018**, *57* (35), 11140–11162. https://doi.org/10.1002/anie.201711842.

(198) Green, R. A.; Adams, R. W.; Duckett, S. B.; Mewis, R. E.; Williamson, D. C.; Green, G. G. R. The Theory and Practice of Hyperpolarization in Magnetic Resonance Using Parahydrogen. *Prog Nucl Magn Reson Spectrosc* **2012**, *67* (November), 1–48. https://doi.org/10.1016/j.pnmrs.2012.03.001.

(199) Fear, E. J.; Kennerley, A. J.; Rayner, P. J.; Norcott, P.; Roy, S. S.; Duckett, S. B. SABRE Hyperpolarized Anticancer Agents for Use in 1H MRI. *Magn Reson Med* **2022**, No. December 2021, 1–17. https://doi.org/10.1002/mrm.29166.

(200) Kidd, B. E.; Gesiorski, J. L.; Gemeinhardt, M. E.; Shchepin, R. V.; Kovtunov, K. V.; Koptyug, I. V.; Chekmenev, E. Y.; Goodson, B. M. Facile Removal of Homogeneous SABRE Catalysts for Purifying Hyperpolarized Metronidazole, a Potential Hypoxia Sensor. *Journal of Physical Chemistry C* **2018**, *122* (29), 16848–16852. https://doi.org/10.1021/acs.jpcc.8b05758.

(201) Schmidt, A. B.; Eills, J.; Dagys, L.; Gierse, M.; Keim, M.; Lucas, S.; Bock, M.; Schwartz, I.; Zaitsev, M.; Chekmenev, E. Y.; Knecht, S. Over 20% Carbon-13 Polarization of Perdeuterated Pyruvate Using Reversible Exchange with Parahydrogen and Spin-Lock Induced Crossing at 50 MT. *J Phys Chem Lett* **2023**, *14* (23), 5305–5309. https://doi.org/10.1021/acs.jpclett.3c00707.

(202) Knecht, S.; Kiryutin, A. S.; Yurkovskaya, A. V.; Ivanov, K. L. Efficient Conversion of Anti-Phase Spin Order of Protons into 15N Magnetisation Using SLIC-SABRE. *Mol Phys* **2019**, *117* (19), 2762–2771. https://doi.org/10.1080/00268976.2018.1515999.

(203) Rios, A. C.; Bera, P. P.; Moreno, J. A.; Cooper, G. Pyruvate Aldol Condensation Product: A Metabolite That Escaped Synthetic Preparation for over a Century. *ACS Omega* **2020**, *5* (25), 15063–15068. https://doi.org/10.1021/acsomega.0c00877.

(204) Notes, U.; References, U.; Boese, A. D.; Handy, N. C.; Cammi, R.; Cappelli, C.; Corni, S.; Tomasi, J.; Clemente, F.; Vreven, T.; Frisch, M. J.; Collins, M. A.; Fukui, K.; Henderson, T. M.; Izmaylov, A. F.; Scalmani, G.; Scuseria, G. E.; Izmaylov, A. F.; Scuseria, G.; Frisch, M. J.; Marenich, A. V; Cramer, C. J.; Truhlar, D. G. Gaussian 09 Revision B . 01 Release Notes. **2010**, *125* (August), 8–11.

(205) Stephens, P. J.; Devlin, F. J.; Chabalowski, C. F.; Frisch, M. J. Ab Initio Calculation of Vibrational Absorption and Circular Dichroism Spectra Using Functional Force Fields. *Physical Chemistry &copy* **1994**, *98*, 54.

(206) Vosko, S. H.; Wilk, L.; Nusair, M. Accurate Spin-Dependent Electron Liquid Correlation Energies for Local Spin Density Calculations: A Critical Analysis. *Can J Phys* **1980**, *58* (8), 1200–1211. https://doi.org/10.1139/p80-159.

(207) Lee, C.; Yang, W.; Parr, R. G. Development of the Colle-Salvetti Correlation-Energy Formula into a Functional of the Electron Density. *Phys Rev B* **1988**, *37* (2), 785–789. https://doi.org/10.1103/PhysRevB.37.785.

(208) Becke, A. D. Density-functional Thermochemistry. III. The Role of Exact Exchange. *J Chem Phys* **1993**, *98* (7), 5648–5652. https://doi.org/10.1063/1.464913.

(209) Ehlers, A. W.; Böhme, M.; Dapprich, S.; Gobbi, A.; Höllwarth, A.; Jonas, V.; Köhler, K. F.; Stegmann, R.; Veldkamp, A.; Frenking, G. A Set of F-Polarization Functions for Pseudo-Potential Basis Sets of the Transition Metals Sc-Cu, Y-Ag and La-Au. *Chem Phys Lett* **1993**, *208* (1), 111–114. https://doi.org/https://doi.org/10.1016/0009-2614(93)80086-5.

(210) Ditchfield, R.; Hehre, W. J.; Pople, J. A. Self-Consistent Molecular-Orbital Methods. IX. An Extended Gaussian-Type Basis for Molecular-Orbital Studies of Organic Molecules. *J Chem Phys* **1971**, *54* (2), 724–728. https://doi.org/10.1063/1.1674902.

(211) Browning, A.; Mcculloch, K.; Bedoya, G.; Dedesma, C.; Boyd, M.; Rosen, M. S.; Chekmenev, E. Y.; Yen, Y. Facile Hyperpolarization Chemistry for Molecular Imaging and Metabolic Tracking of [1- 13 C] Pyruvate in Vivo. 1–24.

(212) Hövener, J. B.; Knecht, S.; Schwaderlapp, N.; Hennig, J.; Von Elverfeldt, D. Continuous Re-Hyperpolarization of Nuclear Spins Using Parahydrogen: Theory and Experiment. *ChemPhysChem* **2014**, *15* (12), 2451–2457. https://doi.org/10.1002/cphc.201402177.

(213) Pravdivtsev, A. N.; Kempf, N.; Plaumann, M.; Bernarding, J.; Scheffler, K.; Hövener, J.-B.; Buckenmaier, K. Coherent Evolution of Signal Amplification by Reversible Exchange in Two Alternating Fields (Alt-SABRE). *ChemPhysChem* **2021**, *22* (23), 2381–2386. https://doi.org/https://doi.org/10.1002/cphc.202100543.

(214) Köcher, S. S.; Düwel, S.; Hundshammer, C.; Glaser, S. J.; Schilling, F.; Granwehr, J.; Scheurer, C. Ab Initio Simulation of PH-Sensitive Biomarkers in Magnetic Resonance Imaging. *Journal of Physical Chemistry A* **2018**, *122* (40), 7983–7990. https://doi.org/10.1021/acs.jpca.8b04665.

(215) MacCulloch, K.; Browning, A.; Guarin Bedoya, D. O.; McBride, S. J.; Abdulmojeed, M. B.; Dedesma, C.; Goodson, B. M.; Rosen, M. S.; Chekmenev, E. Y.; Yen, Y.-F.; TomHon, P.; Theis, T. Facile Hyperpolarization Chemistry for Molecular Imaging and Metabolic Tracking of [1–13C]Pyruvate in Vivo. *J Magn Reson Open* **2023**, *16–17* (July), 100129. https://doi.org/10.1016/j.jmro.2023.100129.

(216) de Maissin, H.; Groß, P. R.; Mohiuddin, O.; Weigt, M.; Nagel, L.; Herzog, M.; Wang, Z.; Willing, R.; Reichardt, W.; Pichotka, M.; Heß, L.; Reinheckel, T.; Jessen, H. J.; Zeiser, R.; Bock, M.; von Elverfeldt, D.; Zaitsev, M.; Korchak, S.; Glöggler, S.; Hövener, J.-B.; Chekmenev, E. Y.; Schilling, F.; Knecht, S.; Schmidt, A. B.; de Maissin, H.; Groß, P. R.; Mohiuddin, O.; Weigt, M.; Herzog, M.; Wang, Z.; Willing, R.; Reichardt, W.; Pichotka, M.; Bock, M.; von Elverfeldt, D.; Zaitsev, M.; Schmidt, A. B.; Nagel, L.; Schilling, F.; Heß, L.; Reinheckel, T.; Jessen, H. J.; Zeiser, R.; Korchak, S.; Glöggler, S.; Hövener, J.; Chekmenev, E. Y.; Knecht, S. Magnetic Resonance Imaging In Vivo Metabolic Imaging of [1-13 C]Pyruvate-d 3 Hyperpolarized By Reversible Exchange With Parahydrogen. *Angew. Chem. Int. Ed* **2023**, *62*, 202306654–202306655. https://doi.org/10.26434/chemrxiv-2023-9trxb.

(217) Fiedorowicz, M.; Wieteska, M.; Rylewicz, K.; Kossowski, B.; Piatkowska-Janko, E.; Czarnecka, A. M.; Toczylowska, B.; Bogorodzki, P. Hyperpolarized 13C Tracers:

Technical Advancements and Perspectives for Clinical Applications. *Biocybern Biomed Eng* **2021**, *41* (4), 1466–1485. https://doi.org/10.1016/j.bbe.2021.03.010.

(218) Ruddlesden, A. J.; Duckett, S. B. Solvent Responsive Catalyst Improves NMR Sensitivity via Efficient Magnetisation Transfer †. *Chem. Commun* **2016**, *52*, 8467. https://doi.org/10.15124/cdaf969f-ba47-401e-876b-512c0cece55c.

(219) Shi, F.; He, P.; Best, Q. A.; Groome, K.; Truong, M. L.; Coffey, A. M.; Zimay, G.; Shchepin, R. V.; Waddell, K. W.; Chekmenev, E. Y.; Goodson, B. M. Aqueous NMR Signal Enhancement by Reversible Exchange in a Single Step Using Water-Soluble Catalysts. *Journal of Physical Chemistry C* **2016**, *120* (22), 12149–12156. https://doi.org/10.1021/acs.jpcc.6b04484.

(220) Richards, F. M.; Wycoff, H. W.; Corcoran, R.; Labelle, M.; Czarnik, A. W.; Breslow, R. *The Enzymes*; UTC, 1982; Vol. 15. https://pubs.acs.org/sharingguidelines.

(221) Sundberg, R. J.; Bruce Martin, R. *Interactions of Histidine and Other Imidazole Derivatives with Transition Metal Ions in Chemical and Biological Systems*. https://pubs.acs.org/sharingguidelines.

(222) Teli, P.; Sahiba, N.; Sethiya, A.; Soni, J.; Agarwal, S. Imidazole Derivatives: Impact and Prospects in Antiviral Drug Discovery. In *Imidazole-Based Drug Discovery*; Elsevier, 2021; pp 167–193. https://doi.org/10.1016/B978-0-323-85479-5.00001-0.

(223) Noubhani, A. M.; Dieryck, W.; Bakalara, N.; Latxague, L.; Santarelli, X. Evaluation of Chromatographic Recycling for Imidazole Used in the Chromatographic Purification of His-Tag Recombinant Proteins. *J Chromatogr B Analyt Technol Biomed Life Sci* **2003**, *790* (1–2), 153–159. https://doi.org/10.1016/S1570-0232(03)00088-6.

(224) Van Sluis, R.; Bhujwalla, Z. M.; Raghunand, N.; Ballesteros, P.; Alvarez, J.; Cerdán, S.; Galons, J. P.; Gillies, R. J. In Vivo Imaging of Extracellular PH Using 1H MRSI. *Magn Reson Med* **1999**, *41* (4), 743–750. https://doi.org/10.1002/(SICI)1522-2594(199904)41:4<743::AID-MRM13>3.0.CO;2-Z.

(225) Hayashi, N.; Kuyama, H.; Nakajima, C.; Kawahara, K.; Miyagi, M.; Nishimura, O.; Matsuo, H.; Nakazawa, T. Imidazole C-2 Hydrogen/Deuterium Exchange Reaction at Histidine for Probing Protein Structure and Function with Matrix-Assisted Laser Desorption Ionization Mass Spectrometry. *Biochemistry* **2014**, *53* (11), 1818–1826. https://doi.org/10.1021/bi401260f.

(226) Bollinger, K. M.; Brouwer, D. M.; Mackor, E. L.; MacLean, C.; Olah, G. A.; Liang, G.; Mo, Y. K.; Amer, J.; Tolman, C. A.; Hasek, W. K.; Smith, W. C.; Englehardt, V. A.; Olah, A.; White, A. M.; Wong, J. L.; Keck, J. H. *) (A) Positional Reactivities and Mechanisms of Deuteration of 1-Methylimidazole in PD and-D0 Regions. Reinvestigation of the Kinetics of 2-Hydrogen Exchange in Imidazole * ¿Q>nd *2= N<0>N II I III |0D"*; Academic Press, 1974; Vol. 39. https://pubs.acs.org/sharingguidelines.

(227) Pravdivtsev, A. N.; Yurkovskaya, A. V.; Vieth, H. M.; Ivanov, K. L.; Kaptein, R. Level Anti-Crossings Are a Key Factor for Understanding Para-Hydrogen-Induced Hyperpolarization in SABRE Experiments. *ChemPhysChem* **2013**, *14* (14), 3327–3331. https://doi.org/10.1002/cphc.201300595.

(228) Lloyd, L. S.; Asghar, A.; Burns, M. J.; Charlton, A.; Coombes, S.; Cowley, M. J.; Dear, G. J.; Duckett, S. B.; Genov, G. R.; Green, G. G. R.; Highton, L. A. R.; Hooper, A. J. J.; Khan, M.; Khazal, I. G.; Lewis, R. J.; Mewis, R. E.; Roberts, A. D.; Ruddlesden, A. J.

Hyperpolarisation through Reversible Interactions with Parahydrogen. *Catal Sci Technol* **2014**, *4* (10), 3544–3554. https://doi.org/10.1039/c4cy00464g.

(229) Rayner, P. J.; Norcott, P.; Appleby, K. M.; Iali, W.; John, R. O.; Hart, S. J.; Whitwood, A. C.; Duckett, S. B. Fine-Tuning the Efficiency of Para-Hydrogen-Induced Hyperpolarization by Rational N-Heterocyclic Carbene Design. *Nat Commun* **2018**, *9* (1). https://doi.org/10.1038/s41467-018-06766-1.

(230) Semenova, O.; Richardson, P. M.; Parrott, A. J.; Nordon, A.; Halse, M. E.; Duckett, S. B. Reaction Monitoring Using SABRE-Hyperpolarized Benchtop (1 T) NMR Spectroscopy. *Anal Chem* **2019**, *91* (10), 6695–6701. https://doi.org/10.1021/acs.analchem.9b00729.

(231) Chae, H.; Min, S.; Jeong, H. J.; Namgoong, S. K.; Oh, S.; Kim, K.; Jeong, K. Organic Reaction Monitoring of a Glycine Derivative Using Signal Amplification by Reversible Exchange-Hyperpolarized Benchtop Nuclear Magnetic Resonance Spectroscopy. *Anal Chem* **2020**, *92* (16), 10902–10907. https://doi.org/10.1021/acs.analchem.0c01270.

(232) Zhang, G.; Schilling, F.; Glaser, S. J.; Hilty, C. Reaction Monitoring Using Hyperpolarized NMR with Scaling of Heteronuclear Couplings by Optimal Tracking. *Journal of Magnetic Resonance* **2016**, *272*, 123–128. https://doi.org/10.1016/j.jmr.2016.09.006.

(233) Nonaka, H.; Hata, R.; Doura, T.; Nishihara, T.; Kumagai, K.; Akakabe, M.; Tsuda, M.; Ichikawa, K.; Sando, S. A Platform for Designing Hyperpolarized Magnetic Resonance Chemical Probes. *Nat Commun* **2013**, *4*. https://doi.org/10.1038/ncomms3411.

(234) Giernoth, R.; Heinrich, H.; Adams, N. J.; Deeth, R. J.; Bargon, J.; Brown, J. M. PHIP Detection of a Transient Rhodium Dihydride Intermediate in the Homogeneous

Hydrogenation of Dehydroamino Acids. *Journal of the American Chemical Society*. December 13, 2000, pp 12381–12382. https://doi.org/10.1021/ja002516o.

(235) Godard, C.; López-Serrano, J.; Gálvez-López, M. D.; Roselló-Merino, M.; Duckett, S. B.; Khazal, I.; Lledós, A.; Whitwood, A. C. Detection of Platinum Dihydride Bisphosphine Complexes and Studies of Their Reactivity through Para-Hydrogen-Enhanced NMR Methods. *Magnetic Resonance in Chemistry* **2008**, *46* (SUPPL. 1). https://doi.org/10.1002/mrc.2342.

(236) Shchepin, R. V.; Birchall, J. R.; Chukanov, N. V.; Kovtunov, K. V.; Koptyug, I. V.; Theis, T.; Warren, W. S.; Gelovani, J. G.; Goodson, B. M.; Shokouhi, S.; Rosen, M. S.; Yen, Y. F.; Pham, W.; Chekmenev, E. Y. Hyperpolarizing Concentrated Metronidazole 15NO2 Group over Six Chemical Bonds with More than 15 % Polarization and a 20 Minute Lifetime. *Chemistry - A European Journal* **2019**, *25* (37), 8829–8836. https://doi.org/10.1002/chem.201901192.

(237) Shchepin, R. V.; Barskiy, D. A.; Coffey, A. M.; Theis, T.; Shi, F.; Warren, W. S.; Goodson, B. M.; Chekmenev, E. Y. 15N Hyperpolarization of Imidazole-15N2 for Magnetic Resonance PH Sensing via SABRE-SHEATH. *ACS Sens* **2016**, *1* (6), 640–644. https://doi.org/10.1021/acssensors.6b00231.

(238) Mukhopadhyay, S.; Batra, S. Applications of Sodium Nitrite in Organic Synthesis. *European Journal of Organic Chemistry*. Wiley-VCH Verlag October 17, 2019, pp 6424–6451. https://doi.org/10.1002/ejoc.201900951.

(239) Schwander, H. R. *HETEROCYCLIC COUPLING COMPONENTS*.

(240) Addy, P. S.; Erickson, S. B.; Italia, J. S.; Chatterjee, A. A Chemoselective Rapid Azo-Coupling Reaction (CRACR) for Unclickable Bioconjugation. *J Am Chem Soc* **2017**, *139* (34), 11670–11673. https://doi.org/10.1021/jacs.7b05125.

(241) Vaiano, F.; Mari, F.; Busardò, F. P.; Bertol, E. Enhancing the Sensitivity of the LC-MS/MS Detection of Propofol in Urine and Blood by Azo-Coupling Derivatization Forensic Toxicology. *Anal Bioanal Chem* **2014**, *406* (15), 3579–3587. https://doi.org/10.1007/s00216-013-7573-y.

(242) Gamliel, A.; Uppala, S.; Sapir, G.; Harris, T.; Nardi-Schreiber, A.; Shaul, D.; Sosna, J.; Gomori, J. M.; Katz-Brull, R. Hyperpolarized [15 N]Nitrate as a Potential Long Lived Hyperpolarized Contrast Agent for MRI. *Journal of Magnetic Resonance* **2019**, *299*, 188–195. https://doi.org/10.1016/j.jmr.2019.01.001.

APPENDICES

Appendix A: Cartesian Coordinates and Energies of Optimized Structures

The structures shown in **Figure 4.3A** in in chapter 4were optimized using Density functional theory at the B3LYP3–6 level of theory with a D3 dispersion correction, and 6-311g (d) basis set for C, O, N and S atoms. Iridium was modelled with the Stuttgart-Dresden effective core potential and its associated basis from the GENECP key word within Gaussian with an f-polarization function derived from Ehlers et al.7,8 The cartesian coordinates of the optimized geometries are listed below as extracted from their respective log files.

1. Complex A1 Fully deprotonated (Gibbs Free Energy: -1954.592000 a.u)

Center Number	Atomic Number	Forces (Hartrees/Bohr) X	Y	Z
1	6	-0.000009791	-0.000010479	0.000015024
2	6	0.000004651	0.000006933	-0.000015165
3	1	0.000000345	0.000001397	-0.000002113
4	1	-0.000000281	0.000003402	-0.000002947
5	6	0.000004490	0.000002004	-0.000001554
6	7	-0.000000508	0.000007402	-0.000005397
7	7	-0.000001803	0.000000773	0.000002257
8	6	0.000006837	0.000003172	-0.000014467
9	6	0.000005240	0.000001144	-0.000002742
10	6	-0.000007827	0.000000069	0.000001241

11	6	-0.000007526	0.000002672	-0.000000357
12	1	-0.000000926	0.000001059	-0.000001426
13	6	0.000005955	-0.000002626	-0.000003443
14	1	-0.000001584	-0.000000862	-0.000002660
15	6	-0.000002353	-0.000000824	0.000000297
16	1	0.000000422	0.000001263	-0.000002651
17	1	-0.000002536	-0.000000959	-0.000003046
18	1	-0.000000621	0.000000937	-0.000003873
19	6	-0.000002348	0.000000228	0.000003462
20	6	0.000000064	0.000003022	-0.000000037
21	6	0.000002083	-0.000001386	-0.000002961
22	6	0.000001663	0.000000198	0.000000008
23	1	0.000000706	0.000001110	0.000000184
24	6	-0.000000687	0.000000961	0.000001200
25	1	-0.000000163	-0.000001171	0.000000097
26	6	0.000001559	-0.000000006	0.000002061
27	1	0.000000393	0.000001490	0.000001369
28	1	0.000000186	-0.000001129	0.000000652
29	1	0.000000701	0.000000211	0.000001609
30	77	-0.000006295	-0.000018140	0.000001475
31	1	0.000000321	-0.000000527	-0.000001245
32	1	0.000000316	0.000002754	-0.000000542
33	8	-0.000002921	-0.000003218	0.000000659

34	16	0.000003005	0.000005386	-0.000005667
35	8	0.000008452	-0.000005373	0.000005215
36	6	-0.000002120	0.000012124	-0.000003187
37	8	-0.000008586	0.000000967	-0.000003062
38	6	0.000001771	-0.000005622	0.000005504
39	8	0.000002781	0.000000489	0.000000468
40	6	0.000000062	-0.000006054	0.000006117
41	1	0.000000898	-0.000001806	0.000000194
42	6	0.000000575	0.000000543	-0.000001584
43	6	0.000004949	-0.000007982	0.000003165
44	1	-0.000000610	0.000001125	0.000001369
45	1	-0.000000881	0.000004219	0.000001092
46	1	-0.000000550	-0.000001043	0.000001837
47	6	0.000001819	0.000001286	0.000004300
48	8	-0.000001248	-0.000005513	0.000003459
49	8	-0.000000738	-0.000003392	0.000002418
50	6	-0.000000327	0.000001382	0.000003751
51	1	0.000001764	0.000001463	0.000001134
52	1	-0.000000028	0.000002206	0.000001056
53	1	0.000001016	0.000000796	-0.000000856
54	6	0.000000036	0.000003903	0.000002627
55	1	-0.000000372	-0.000000715	0.000002973
56	1	-0.000000193	0.000000051	0.000000595

57	1	0.000000766	0.000000686	0.000002113

---

2. Complex A2 Fully deprotonated (Gibbs Free Energy: -1954.605112 a.u)

Center Number	Atomic Number	Forces (Hartrees/Bohr) X	Y	Z
1	6	0.000000414	0.000000264	-0.000000245
2	6	-0.000000211	0.000000536	-0.000002044
3	1	0.000000468	-0.000000473	0.000000650
4	1	0.000000184	0.000000704	-0.000002646
5	6	-0.000000050	0.000001301	-0.000001243
6	7	-0.000000845	-0.000000121	0.000001587
7	7	-0.000000359	0.000000344	-0.000001632
8	6	0.000000422	-0.000000732	0.000002071
9	6	0.000000736	-0.000002871	0.000002343
10	6	-0.000002838	-0.000000232	0.000003023
11	6	0.000000536	-0.000001637	0.000004543
12	1	0.000002880	-0.000001308	0.000003368
13	6	-0.000001090	-0.000000617	0.000005079
14	1	-0.000003116	0.000000179	0.000003037
15	6	-0.000000306	-0.000001913	0.000006160

16	1	0.000002261	-0.000002702	0.000005380
17	1	-0.000003007	-0.000000805	0.000005874
18	1	-0.000000422	-0.000002213	0.000007197
19	6	0.000000063	0.000002085	-0.000003728
20	6	0.000000595	0.000001564	-0.000005217
21	6	-0.000002324	0.000002094	-0.000003855
22	6	0.000000350	0.000002175	-0.000006446
23	1	0.000001620	0.000000750	-0.000004759
24	6	-0.000002592	0.000002910	-0.000005878
25	1	-0.000003344	0.000002417	-0.000003045
26	6	-0.000001277	0.000002591	-0.000006846
27	1	0.000001272	0.000001958	-0.000007540
28	1	-0.000003900	0.000003430	-0.000005980
29	1	-0.000001539	0.000003228	-0.000008190
30	77	-0.000000791	0.000003354	-0.000000252
31	1	-0.000003574	0.000000918	-0.000001692
32	1	-0.000002288	0.000001463	0.000000440
33	8	0.000001974	0.000000347	-0.000002359
34	16	-0.000000256	-0.000000081	-0.000002056
35	8	-0.000004682	-0.000000073	0.000001583
36	6	-0.000000466	0.000001129	0.000001520
37	8	-0.000003645	-0.000001211	0.000001548
38	8	0.000005445	0.000003395	-0.000003976

39	6	-0.000004437	-0.000006167	0.000004777
40	8	0.000005809	-0.000000220	0.000005602
41	6	-0.000001391	-0.000002326	0.000006260
42	6	0.000001703	-0.000000080	0.000001280
43	1	0.000001143	-0.000001634	0.000004394
44	6	0.000002216	-0.000004447	0.000005559
45	1	0.000002822	-0.000002516	0.000005860
46	1	0.000003663	-0.000002718	0.000003566
47	1	0.000002803	-0.000001999	0.000005390
48	6	0.000000617	-0.000001240	0.000002980
49	8	-0.000001020	-0.000001216	0.000001275
50	6	0.000002621	-0.000000372	-0.000001526
51	1	0.000003146	-0.000001376	0.000000149
52	1	0.000000271	0.000000119	-0.000001764
53	1	0.000002917	-0.000000951	-0.000002482
54	6	0.000000353	0.000001483	-0.000004054
55	1	-0.000001023	0.000001105	-0.000003960
56	1	-0.000000075	0.000001856	-0.000004736
57	1	0.000001568	0.000000554	-0.000004346

---

3. Complex A3 Fully deprotonated (Gibbs Free Energy: -1954.603561 a.u)

Center Number	Atomic Number	Forces (Hartrees/Bohr) X	Y	Z
1	6	0.000002912	-0.000001727	0.000003994
2	6	-0.000000183	0.000000631	-0.000004469
3	1	-0.000000182	-0.000000610	-0.000001042
4	1	-0.000000298	-0.000001389	-0.000003909
5	6	-0.000011878	0.000002021	-0.000002941
6	7	0.000001854	0.000011096	-0.000000446
7	7	0.000004133	-0.000006532	-0.000010260
8	6	0.000001283	-0.000003857	0.000003263
9	6	-0.000003773	-0.000001029	-0.000001845

10	6	0.000001178	-0.000000231	-0.000000257
11	6	0.000002501	0.000000403	-0.000000198
12	1	0.000000115	0.000001095	0.000000623
13	6	0.000001218	0.000000898	0.000000425
14	1	0.000001330	0.000000477	0.000000403
15	6	0.000001003	0.000002195	0.000001472
16	1	-0.000000617	0.000000698	0.000001624
17	1	0.000001198	0.000001055	0.000000843
18	1	0.000000616	0.000000976	0.000002104
19	6	-0.000004246	-0.000009282	0.000006981
20	6	0.000002813	-0.000005033	0.000001641
21	6	0.000010086	0.000010178	0.000006092
22	6	-0.000002116	-0.000001126	-0.000005143
23	1	-0.000003315	0.000000217	-0.000003122
24	6	-0.000001978	-0.000005921	-0.000011594
25	1	-0.000003059	-0.000007719	-0.000004897
26	6	-0.000001573	0.000000978	0.000001713
27	1	0.000000365	-0.000001956	-0.000000848
28	1	0.000002141	-0.000000381	-0.000001628
29	1	-0.000000013	-0.000001467	-0.000003401
30	77	0.000001913	0.000012554	-0.000002365
31	1	-0.000007086	-0.000000225	-0.000006404
32	1	-0.000001332	0.000000980	-0.000003980

33	8	-0.000004428	0.000001142	0.000013791
34	16	0.000015932	-0.000013717	-0.000009783
35	8	0.000004808	0.000004244	0.000019627
36	6	-0.000003317	-0.000003779	-0.000007882
37	8	-0.000003183	0.000000073	0.000006341
38	6	0.000001586	0.000003862	-0.000011466
39	8	0.000024890	-0.000022786	0.000010074
40	6	-0.000022334	0.000016748	-0.000008680
41	6	-0.000000805	0.000007366	0.000001198
42	1	0.000001733	0.000000151	0.000001426
43	1	0.000000296	-0.000000116	0.000001913
44	1	0.000000515	-0.000002916	0.000002212
45	8	-0.000002538	0.000014574	0.000002123
46	8	-0.000000204	0.000002242	0.000001364
47	6	0.000002315	-0.000015490	0.000001784
48	6	-0.000000146	-0.000006955	0.000018755
49	1	0.000002756	-0.000001428	0.000002600
50	6	-0.000017905	0.000023974	0.000008809
51	1	0.000010870	-0.000000482	-0.000014000
52	1	0.000002108	-0.000003243	0.000001598
53	1	0.000000436	-0.000002910	-0.000001901
54	6	-0.000002478	0.000007667	-0.000008969
55	1	0.000002066	-0.000001356	-0.000000321

56	1	-0.000004453	-0.000006299	0.000005368
57	1	-0.000003531	0.000001468	0.000001589

---

4. Complex A1 prime Fully deprotonated (Gibbs Free Energy :- 1954.597375)

Center Number	Atomic Number	Atomic Type	Coordinates (Angstroms) X	Y	Z
1	6	0	1.975660	3.443026	0.069038
2	6	0	3.174033	2.833173	-0.020252
3	1	0	1.710408	4.473252	0.232642
4	1	0	4.176754	3.218455	0.045518
5	6	0	1.571807	1.225041	-0.322754
6	7	0	1.009078	2.461473	-0.123765
7	7	0	2.924045	1.483252	-0.267821
8	6	0	-0.399714	2.733592	-0.070935
9	6	0	-0.985902	3.035044	1.154272
10	6	0	-1.158194	2.680318	-1.235932
11	6	0	-2.358413	3.264517	1.216619
12	1	0	-0.374004	3.067634	2.049053
13	6	0	-2.530339	2.903949	-1.165447
14	1	0	-0.677406	2.435840	-2.175055
15	6	0	-3.132438	3.188666	0.059729

16	1	0	-2.824266	3.484084	2.171077
17	1	0	-3.131057	2.844661	-2.066518
18	1	0	-4.205344	3.336407	0.115155
19	6	0	3.990687	0.535895	-0.407548
20	6	0	4.195330	-0.118200	-1.620947
21	6	0	4.843706	0.314485	0.672096
22	6	0	5.241495	-1.028953	-1.738989
23	1	0	3.535420	0.084969	-2.454369
24	6	0	5.893895	-0.594229	0.545302
25	1	0	4.687554	0.846931	1.603631
26	6	0	6.087715	-1.273347	-0.656130
27	1	0	5.398092	-1.544744	-2.679884
28	1	0	6.552697	-0.772542	1.387779
29	1	0	6.900684	-1.984614	-0.752527
30	77	0	0.580796	-0.488314	-0.548749
31	1	0	1.908827	-1.094872	-1.108183
32	1	0	0.267188	-0.037749	-2.054418
33	8	0	-0.099496	-2.042766	2.372905
34	16	0	1.021886	-1.304758	1.672176
35	8	0	-0.618995	-2.247651	-0.844054
36	8	0	-1.494707	0.052144	0.154641
37	6	0	-2.352247	-0.829086	-0.010474
38	6	0	-1.846135	-2.231239	-0.456648

39	8	0	-2.590206	-3.202210	-0.374732
40	6	0	-3.730199	-0.502576	0.312475
41	1	0	-3.818536	0.284829	1.055870
42	6	0	-4.881968	-0.875863	-0.282533
43	6	0	-5.033914	-1.803614	-1.446970
44	1	0	-4.093676	-2.063812	-1.925384
45	1	0	-5.518247	-2.728691	-1.121628
46	1	0	-5.710500	-1.352963	-2.176582
47	6	0	-6.201291	-0.256230	0.266741
48	8	0	-7.252861	-0.759224	-0.194565
49	8	0	-6.095381	0.662566	1.114637
50	6	0	1.578818	0.006779	2.798035
51	1	0	0.746018	0.700157	2.900813
52	1	0	1.832316	-0.439392	3.759068
53	1	0	2.435298	0.514409	2.359257
54	6	0	2.484327	-2.377586	1.701033
55	1	0	2.247289	-3.235792	1.074774
56	1	0	3.327585	-1.830577	1.282290
57	1	0	2.676424	-2.686860	2.728262

5. Complex A2 prime Fully deprotonated(Gibbs Free Energy: -1954.604068)

Center Number	Atomic Number	Atomic Type	Coordinates (Angstroms) X	Y	Z

1	6	0	1.586118	3.538246	0.415267
2	6	0	2.768709	2.893634	0.401168
3	1	0	1.332905	4.557932	0.649152
4	1	0	3.767022	3.231179	0.619740
5	6	0	1.168748	1.382724	-0.232418
6	7	0	0.618500	2.618694	0.018387
7	7	0	2.512453	1.585740	-0.007989
8	6	0	-0.768041	2.973013	-0.086957
9	6	0	-1.495097	3.224716	1.071866
10	6	0	-1.357827	3.084920	-1.341462
11	6	0	-2.839532	3.573150	0.973283
12	1	0	-1.018657	3.110389	2.038107
13	6	0	-2.702110	3.434688	-1.434908
14	1	0	-0.769971	2.880041	-2.227478
15	6	0	-3.445450	3.674340	-0.278713
16	1	0	-3.416689	3.748631	1.874660
17	1	0	-3.169811	3.515672	-2.410386
18	1	0	-4.494962	3.938993	-0.353738
19	6	0	3.566450	0.623129	-0.133857
20	6	0	4.260058	0.226479	1.006739
21	6	0	3.925172	0.138443	-1.390402
22	6	0	5.319148	-0.672227	0.888835
23	1	0	3.942276	0.591049	1.974325

24	6	0	4.973603	-0.771488	-1.499997
25	1	0	3.378998	0.468133	-2.264841
26	6	0	5.672541	-1.177344	-0.361501
27	1	0	5.854596	-0.989034	1.777145
28	1	0	5.248527	-1.158097	-2.475266
29	1	0	6.489620	-1.885236	-0.450490
30	77	0	0.201675	-0.279814	-0.667546
31	1	0	1.482652	-0.818420	-1.404163
32	1	0	-0.236172	0.382316	-2.049041
33	8	0	1.661594	-0.727265	2.460661
34	16	0	0.996347	-1.464447	1.312403
35	8	0	-0.998301	-2.088889	-0.969889
36	6	0	-2.206713	-1.947426	-1.391806
37	8	0	-2.579578	-1.464192	-2.459570
38	8	0	-1.844527	0.264485	0.071183
39	6	0	-2.323778	-0.033102	1.204988
40	8	0	-1.796612	0.062888	2.320220
41	6	0	-3.942183	-1.944438	0.495382
42	1	0	-4.804850	-2.458898	0.918798
43	6	0	-3.291347	-2.555517	-0.515698
44	6	0	-3.699351	-3.929247	-0.976661
45	1	0	-4.512404	-4.344342	-0.378379
46	1	0	-4.010822	-3.897180	-2.025150

47	1	0	-2.844449	-4.612546	-0.924313
48	6	0	-3.739082	-0.626919	1.139790
49	8	0	-4.672676	-0.069786	1.706165
50	6	0	-0.217825	-2.616167	2.025447
51	1	0	-0.928055	-2.005272	2.574875
52	1	0	-0.714676	-3.116179	1.196319
53	1	0	0.304310	-3.314262	2.679126
54	6	0	2.182196	-2.708643	0.715746
55	1	0	1.667002	-3.346619	-0.001514
56	1	0	2.994956	-2.176920	0.229295
57	1	0	2.545834	-3.283217	1.568043

6. Complex A3 prime Fully deprotonated(Gibbs Free Energy: -1954.603521)

Center Number	Atomic Number	Atomic Type	Coordinates (Angstroms) X	Y	Z
1	6	0	1.119522	3.560782	0.566791
2	6	0	2.382109	3.093786	0.536008
3	1	0	0.723118	4.526254	0.829950
4	1	0	3.322308	3.567980	0.757964
5	6	0	1.012938	1.383638	-0.135676
6	7	0	0.294228	2.520315	0.151342
7	7	0	2.315375	1.769902	0.097413
8	6	0	-1.123704	2.691546	-0.011091

9	6	0	-1.963750	2.587644	1.091671
10	6	0	-1.631990	2.993978	-1.272311
11	6	0	-3.335676	2.770396	0.928920
12	1	0	-1.547465	2.331064	2.058350
13	6	0	-3.002804	3.181450	-1.429839
14	1	0	-0.956518	3.067566	-2.116220
15	6	0	-3.854522	3.066121	-0.330541
16	1	0	-3.994092	2.632623	1.776512
17	1	0	-3.404996	3.409495	-2.411009
18	1	0	-4.923782	3.198288	-0.457675
19	6	0	3.505817	0.999718	-0.112279
20	6	0	4.395363	0.829486	0.947675
21	6	0	3.813641	0.509576	-1.379806
22	6	0	5.590433	0.142942	0.742904
23	1	0	4.157309	1.237273	1.923730
24	6	0	5.003273	-0.186765	-1.575001
25	1	0	3.127612	0.678241	-2.198244
26	6	0	5.892253	-0.373720	-0.515717
27	1	0	6.279472	0.008698	1.569442
28	1	0	5.240618	-0.573168	-2.560240
29	1	0	6.820033	-0.912898	-0.673720
30	77	0	0.223694	-0.359538	-0.673390
31	1	0	1.310118	-0.515787	-1.793828

32	1	0	-0.596087	0.435138	-1.777156
33	8	0	2.668205	-2.436413	0.765248
34	16	0	1.347482	-1.737954	1.021254
35	8	0	-1.289828	-0.362752	0.987270
36	8	0	-0.709924	-2.189435	-1.250628
37	6	0	-3.015336	-1.352282	-1.367547
38	6	0	-3.907194	-1.294548	-2.576795
39	1	0	-3.316291	-1.038768	-3.463442
40	1	0	-4.353488	-2.272760	-2.767653
41	1	0	-4.698454	-0.551527	-2.464708
42	6	0	-1.954195	-2.446480	-1.436879
43	8	0	-2.386757	-3.575173	-1.688915
44	6	0	-2.511016	-0.576412	0.968885
45	6	0	-3.242976	-0.711007	2.319685
46	8	0	-2.742997	-1.539094	3.109928
47	8	0	-4.240962	0.029517	2.448608
48	6	0	-3.297560	-0.638498	-0.262978
49	1	0	-4.225240	-0.076758	-0.211420
50	6	0	0.180258	-3.012594	1.590539
51	1	0	-0.096770	-3.592983	0.713770
52	1	0	0.705482	-3.624231	2.324084
53	1	0	-0.698891	-2.533994	2.023146
54	6	0	1.477427	-0.800689	2.572710

55	1	0	0.486389	-0.407455	2.793563
56	1	0	1.832608	-1.464928	3.360244
57	1	0	2.179876	0.011200	2.406162

7. Complex E1 Fully deprotonated (Gibbs Free Energy: -1954.596799 a.u)

Center Number	Atomic Number	Forces (Hartrees/Bohr) X	Y	Z
1	77	-0.000075059	0.000035770	-0.000120485
2	1	-0.000013070	0.000035635	0.000008835
3	6	-0.000018965	-0.000024024	-0.000022283
4	6	-0.000037966	0.000033092	0.000027251
5	1	0.000002548	-0.000007768	-0.000010070
6	1	0.000005606	-0.000009026	-0.000004885
7	6	-0.000012261	0.000070572	0.000110918
8	7	-0.000036920	-0.000024838	-0.000068930
9	7	0.000043728	0.000033569	-0.000053187
10	6	0.000012598	0.000020049	0.000025650
11	6	0.000011632	0.000004686	-0.000000851
12	6	-0.000009753	-0.000009665	-0.000001613
13	6	-0.000001065	-0.000006636	-0.000018993
14	1	-0.000000760	-0.000003798	-0.000004101

15	6	0.000016926	-0.000003701	0.000016068
16	1	0.000006262	-0.000003505	0.000003160
17	6	-0.000004057	0.000008775	-0.000002016
18	1	-0.000000639	-0.000003831	-0.000001865
19	1	-0.000000867	-0.000003659	-0.000000680
20	1	-0.000000811	-0.000005872	0.000001717
21	6	-0.000012592	-0.000045843	-0.000017333
22	6	-0.000010059	0.000002000	0.000028799
23	6	0.000013458	-0.000024086	0.000008328
24	6	0.000025713	-0.000012286	0.000006198
25	1	0.000007442	0.000009591	-0.000007661
26	6	-0.000025351	0.000021620	0.000018923
27	1	-0.000007917	0.000001436	-0.000001678
28	6	-0.000010635	0.000002176	-0.000037838
29	1	0.000007302	0.000009448	0.000002483
30	1	0.000004913	0.000000067	0.000009501
31	1	-0.000003901	0.000008773	-0.000005869
32	8	-0.000102902	-0.000108431	0.000002013
33	16	0.000089176	-0.000013247	0.000121292
34	1	0.000001322	-0.000057153	0.000013058
35	8	0.000106009	0.000019465	-0.000106272
36	8	0.000038093	0.000045511	0.000015422
37	6	0.000030475	0.000010544	0.000021584

38	8	0.000069528	-0.000014572	-0.000026221
39	6	-0.000038908	-0.000015218	-0.000018813
40	6	-0.000066751	-0.000023691	0.000064858
41	1	-0.000001054	-0.000005291	-0.000001791
42	6	0.000030890	-0.000027197	0.000022414
43	6	-0.000017251	0.000044769	-0.000023758
44	1	-0.000009324	-0.000009285	-0.000012665
45	1	0.000010101	-0.000013888	0.000028272
46	1	-0.000000952	-0.000013785	0.000043387
47	6	0.000024354	0.000062892	-0.000009573
48	8	-0.000039542	-0.000027976	0.000022164
49	8	-0.000001552	-0.000044053	-0.000032948
50	6	0.000000891	0.000018544	0.000009158
51	1	0.000004012	-0.000003200	-0.000005650
52	1	-0.000006731	-0.000005099	0.000014546
53	1	-0.000007012	0.000011927	0.000001716
54	6	0.000011366	0.000064494	-0.000044405
55	1	0.000004224	0.000003086	0.000015846
56	1	0.000007955	-0.000010228	-0.000007264
57	1	-0.000011893	0.000002360	0.000006136

---

8. Complex E2 Fully deprotonated (Gibbs Free Energy: -1954.608547 a.u)

Center Number	Atomic Number	Forces (Hartrees/Bohr) X	Y	Z
1	77	0.000001263	-0.000002270	-0.000004674
2	1	0.000001494	0.000005591	-0.000001792
3	6	0.000001430	-0.000004767	-0.000005455
4	6	-0.000001903	-0.000000043	-0.000003501
5	1	0.000000084	-0.000003562	-0.000007578
6	1	0.000000525	-0.000002437	-0.000010831
7	6	0.000001987	-0.000002458	-0.000002714
8	7	0.000001347	-0.000000040	-0.000010563
9	7	-0.000007483	0.000000258	-0.000003100
10	6	0.000000449	-0.000001619	0.000001040
11	6	0.000000303	-0.000001389	-0.000002668
12	6	-0.000000834	-0.000004335	0.000000371
13	6	0.000000478	-0.000001749	-0.000001865
14	1	0.000000244	0.000000637	-0.000005390
15	6	0.000000583	-0.000005002	0.000002265
16	1	-0.000001009	-0.000003848	0.000002124
17	6	-0.000000099	-0.000002279	0.000001965
18	1	0.000000127	-0.000000350	-0.000002237
19	1	-0.000000494	-0.000005234	0.000004691
20	1	-0.000000222	-0.000003426	0.000002773

21	6	0.000009058	0.000001493	-0.000008268
22	6	-0.000003052	0.000010028	-0.000008522
23	6	-0.000000173	-0.000004125	-0.000005971
24	6	0.000001243	0.000004189	-0.000003348
25	1	0.000000077	0.000005780	-0.000005730
26	6	0.000000087	0.000000142	-0.000006868
27	1	0.000000318	-0.000002945	-0.000005517
28	6	0.000001734	0.000010106	-0.000007317
29	1	0.000000327	0.000007995	-0.000006839
30	1	0.000000363	-0.000000823	-0.000006971
31	1	0.000000739	0.000002257	-0.000007151
32	8	-0.000005232	0.000011498	0.000009139
33	16	0.000006785	0.000003008	0.000009429
34	1	-0.000000238	0.000001327	0.000001401
35	8	-0.000001640	-0.000001508	0.000004508
36	6	-0.000001415	0.000001957	0.000002054
37	8	-0.000004196	-0.000004586	0.000000312
38	6	0.000007638	-0.000003862	0.000001061
39	6	-0.000001659	-0.000004310	0.000000433
40	1	0.000001131	0.000001349	0.000000575
41	1	-0.000001310	0.000000796	0.000003735
42	1	0.000000177	-0.000003389	0.000001944
43	6	0.000001412	-0.000003656	0.000003246

44	1	-0.000000787	-0.000007377	0.000000674
45	6	0.000013572	-0.000004272	0.000003168
46	8	-0.000003897	0.000005357	-0.000004272
47	8	0.000001198	-0.000006367	0.000009964
48	6	-0.000013215	-0.000009470	0.000007692
49	8	-0.000002893	-0.000012141	0.000002208
50	6	0.000000183	0.000008336	0.000006360
51	1	-0.000000392	0.000008286	0.000004985
52	1	-0.000000528	0.000008341	0.000009377
53	1	-0.000000739	0.000008037	0.000006721
54	6	0.000001557	0.000003364	0.000005735
55	1	-0.000001095	0.000002942	0.000011821
56	1	-0.000001092	0.000001917	0.000008778
57	1	-0.000002315	-0.000001353	0.000008593

---

9. Complex E3 Fully deprotonated (Gibbs Free Energy: -1954.599704 a.u)

Center Number	Atomic Number	Forces (Hartrees/Bohr) X	Y	Z
1	77	-0.000021113	-0.000006703	-0.000007255

2	1	0.000004535	-0.000000862	-0.000002902
3	6	0.000003395	0.000000308	-0.000009061
4	6	-0.000000494	0.000003770	0.000008726
5	1	0.000001515	0.000000837	-0.000000160
6	1	0.000001564	0.000000563	0.000003943
7	6	0.000000484	0.000001583	-0.000010878
8	7	0.000006397	0.000001741	0.000017495
9	7	-0.000000505	-0.000006390	-0.000000033
10	6	0.000001615	-0.000000690	-0.000003939
11	6	-0.000001698	-0.000003505	-0.000000769
12	6	0.000007875	0.000001671	0.000000139
13	6	-0.000000407	0.000001218	-0.000004768
14	1	-0.000000618	-0.000000544	-0.000002530
15	6	0.000001351	0.000000356	-0.000005682
16	1	0.000005697	0.000001311	0.000001681
17	6	0.000000520	0.000002196	-0.000006962
18	1	-0.000001002	0.000000337	-0.000005713
19	1	0.000001273	0.000002858	-0.000006366
20	1	0.000000655	0.000001285	-0.000008065
21	6	-0.000007046	-0.000001850	0.000006657
22	6	0.000004152	-0.000000468	0.000007134
23	6	-0.000000817	0.000001179	0.000001710
24	6	-0.000002081	0.000007792	0.000003575

25	1	-0.000003207	-0.000004450	0.000004943
26	6	0.000005473	0.000009962	0.000003610
27	1	0.000002977	-0.000000421	0.000005450
28	6	0.000004373	-0.000025274	0.000010310
29	1	-0.000003021	-0.000002539	0.000006949
30	1	0.000001991	0.000001420	0.000004370
31	1	-0.000002114	0.000004422	0.000005912
32	8	0.000008148	-0.000004794	-0.000026767
33	6	-0.000008569	-0.000009873	0.000050598
34	8	0.000006074	0.000014641	-0.000020855
35	8	0.000001383	0.000019051	0.000009268
36	6	0.000002636	-0.000025695	0.000007344
37	6	-0.000001515	0.000004374	-0.000004425
38	6	0.000002832	0.000001273	0.000000197
39	1	0.000003818	0.000003431	0.000000209
40	1	0.000003369	0.000003720	-0.000002232
41	1	0.000004944	0.000004549	0.000002208
42	6	0.000009493	-0.000011020	-0.000000674
43	8	0.000002161	0.000002311	-0.000009438
44	8	-0.000025124	0.000003180	0.000022934
45	6	0.000002111	0.000011727	0.000001010
46	1	0.000002226	0.000002143	0.000001139
47	8	-0.000006667	-0.000003129	-0.000003020

48	16	0.000006075	0.000000567	-0.000003952
49	1	-0.000004330	0.000005355	-0.000008079
50	6	-0.000004498	-0.000004489	-0.000001476
51	1	-0.000004633	-0.000003221	-0.000004763
52	1	-0.000003250	-0.000003539	-0.000004465
53	1	-0.000005109	-0.000002215	-0.000004249
54	6	-0.000002562	0.000001393	0.000001825
55	1	-0.000002073	-0.000001433	-0.000006434
56	1	-0.000001633	0.000000378	-0.000008294
57	1	0.000002974	0.000000206	-0.000005131

---

10. Complex A1 Singly deprotonated at C1 (Gibbs Free Energy: -1955.046914 a.u)

Center Number	Atomic Number	Forces (Hartrees/Bohr) X	Y	Z
1	6	-0.000003877	-0.000002431	0.000005625
2	6	0.000001234	-0.000000504	0.000001937
3	1	-0.000003068	-0.000000413	0.000004004
4	1	-0.000001541	-0.000000039	0.000005501
5	6	-0.000006796	-0.000002178	0.000003911
6	7	0.000004110	0.000001874	-0.000000281

7	7	-0.000000293	-0.000000492	0.000003461
8	6	-0.000005648	-0.000000313	0.000004704
9	6	-0.000006055	-0.000001012	0.000002586
10	6	0.000001668	-0.000001684	0.000001405
11	6	-0.000002333	0.000000986	0.000002794
12	1	-0.000001829	-0.000001601	0.000001779
13	6	-0.000004501	-0.000001354	0.000001905
14	1	0.000000992	0.000001523	0.000002578
15	6	0.000000323	-0.000001280	0.000001140
16	1	-0.000004110	-0.000001218	0.000000626
17	1	-0.000000557	0.000000337	0.000001483
18	1	-0.000002820	-0.000001950	0.000000398
19	6	-0.000000793	0.000001064	0.000003922
20	6	0.000000777	-0.000000822	0.000003272
21	6	-0.000002091	-0.000000302	0.000002433
22	6	0.000000382	0.000001167	0.000003706
23	1	-0.000001185	-0.000000784	0.000004133
24	6	0.000001267	0.000001925	0.000003748
25	1	0.000003167	0.000001769	0.000004093
26	6	0.000002155	0.000001540	0.000004075
27	1	-0.000000098	0.000000685	0.000003233
28	1	0.000003291	0.000002395	0.000003728
29	1	0.000001602	0.000001748	0.000003431

30	77	-0.000002189	0.000016699	-0.000003103
31	1	0.000003129	0.000003401	0.000004882
32	1	0.000003791	-0.000000859	0.000001090
33	8	-0.000000260	0.000002526	0.000001027
34	16	0.000002701	-0.000020727	0.000003979
35	8	0.000010622	-0.000002495	-0.000000468
36	6	-0.000015392	0.000003370	-0.000006221
37	8	0.000004636	0.000003299	-0.000004084
38	6	0.000002243	0.000005789	-0.000001597
39	8	0.000006195	-0.000004019	-0.000007012
40	6	-0.000002648	-0.000002326	-0.000007464
41	1	0.000004013	0.000000961	-0.000003531
42	6	0.000000405	0.000001243	0.000001624
43	6	0.000003031	-0.000004486	-0.000002691
44	1	-0.000000778	-0.000001530	-0.000007031
45	1	-0.000001499	-0.000001603	-0.000006850
46	1	-0.000001204	-0.000000905	-0.000006889
47	6	0.000004309	-0.000003355	-0.000004766
48	8	-0.000000630	0.000001561	-0.000007308
49	8	0.000003493	0.000001169	-0.000010345
50	1	0.000004426	0.000001607	-0.000007614
51	6	0.000002148	-0.000002797	-0.000004135
52	1	-0.000000577	0.000001871	-0.000003268

53	1	-0.000000337	-0.000000972	-0.000001749
54	1	-0.000001997	-0.000000120	-0.000001336
55	6	-0.000003689	0.000001424	-0.000000189
56	1	0.000001384	-0.000000645	-0.000000950
57	1	0.000000325	0.000001289	-0.000000418
58	1	0.000000978	0.000001995	0.000001086

---

11. Complex A2 Singly deprotonated C1 (Gibbs Free Energy: -1955.050699 a.u)

Center Number	Atomic Number	Forces (Hartrees/Bohr) X	Y	Z
1	6	0.000007953	-0.000006682	-0.000005694
2	6	-0.000006316	0.000000985	0.000005884
3	1	0.000002985	-0.000000864	-0.000000783
4	1	0.000002925	-0.000004077	0.000001408
5	6	-0.000012356	-0.000003414	-0.000013313
6	7	0.000001630	0.000012067	0.000000755
7	7	0.000005883	-0.000003245	0.000009590
8	6	0.000006003	0.000003794	0.000005506
9	6	0.000005218	0.000006223	-0.000003663

10	6	0.000002120	-0.000000453	-0.000002969
11	6	-0.000002138	0.000004269	-0.000004083
12	1	-0.000003408	-0.000007262	0.000003463
13	6	0.000003596	-0.000004563	0.000000110
14	1	0.000003620	0.000001877	-0.000002528
15	6	0.000006707	0.000005009	-0.000007354
16	1	-0.000001137	0.000004134	-0.000002244
17	1	0.000003122	0.000002991	-0.000002900
18	1	0.000001422	0.000004989	-0.000003201
19	6	0.000000164	0.000000988	-0.000012913
20	6	0.000002097	-0.000010893	-0.000005181
21	6	-0.000000843	-0.000000734	0.000008874
22	6	0.000002416	-0.000006909	0.000019638
23	1	0.000004314	-0.000002352	0.000002786
24	6	0.000005595	-0.000006812	0.000001088
25	1	0.000002864	-0.000001256	0.000000523
26	6	0.000000911	-0.000006286	0.000002304
27	1	-0.000000273	-0.000007193	0.000003906
28	1	0.000002284	-0.000005201	0.000001777
29	1	0.000000833	-0.000006641	0.000004075
30	77	0.000014181	-0.000011112	0.000011053
31	1	-0.000000894	-0.000002704	0.000001151
32	1	-0.000001532	-0.000003132	0.000002173

33	8	0.000013922	-0.000038331	0.000032845
34	16	-0.000046948	0.000048519	-0.000052602
35	8	-0.000006201	-0.000001248	0.000002051
36	6	0.000004486	-0.000001553	-0.000001859
37	8	-0.000002522	-0.000000420	0.000000733
38	8	-0.000007393	-0.000002714	-0.000005238
39	6	0.000007618	0.000018960	-0.000029539
40	6	0.000000848	0.000005126	-0.000002314
41	6	-0.000002102	0.000003562	-0.000000199
42	1	-0.000000542	0.000003890	-0.000000834
43	6	-0.000000149	0.000004549	-0.000001934
44	1	-0.000000478	0.000005890	-0.000002803
45	1	-0.000001311	0.000005585	-0.000001776
46	1	0.000001360	0.000004647	-0.000003583
47	6	0.000002009	0.000006863	-0.000001077
48	8	-0.000002283	0.000004475	0.000001260
49	8	0.000016717	-0.000012660	0.000023289
50	1	-0.000016420	0.000000350	-0.000001939
51	6	-0.000005226	0.000011542	0.000002498
52	1	0.000000416	-0.000001658	0.000014012
53	1	-0.000002974	-0.000000555	0.000004146
54	1	-0.000006375	-0.000004685	0.000002577
55	6	-0.000005650	-0.000002120	-0.000003287

56	1	0.000002361	-0.000002670	-0.000000603
57	1	0.000001593	0.000002081	0.000001711
58	1	-0.000004699	-0.000002970	0.000005227

---

12. Complex A3 Singly deprotonated at C1 (Gibbs Free Energy: -1955.033732 a.u)

Center Number	Atomic Number	Forces (Hartrees/Bohr) X	Y	Z
1	6	-0.000005053	0.000002485	-0.000011793
2	6	0.000001654	0.000002710	-0.000001136
3	1	-0.000000764	-0.000000099	-0.000001224
4	1	-0.000000741	-0.000000650	-0.000002967
5	6	0.000011419	-0.000008379	-0.000001676
6	7	-0.000004265	-0.000005213	-0.000001325
7	7	-0.000000468	0.000000319	0.000006888
8	6	-0.000004428	0.000001891	-0.000001286
9	6	-0.000007244	0.000002218	0.000003303
10	6	0.000006756	-0.000000984	0.000002169
11	6	0.000003684	-0.000002277	-0.000001343
12	1	0.000001183	0.000000503	-0.000002613
13	6	-0.000009012	0.000000590	0.000004101

14	1	-0.000002822	-0.000002256	-0.000000722
15	6	0.000000749	0.000000312	-0.000003294
16	1	-0.000000365	0.000000618	-0.000000121
17	1	-0.000000619	-0.000001810	-0.000000510
18	1	-0.000001072	-0.000001567	0.000000574
19	6	-0.000006301	0.000002460	-0.000007472
20	6	0.000004379	0.000006044	-0.000003854
21	6	-0.000000290	-0.000003700	-0.000000628
22	6	-0.000001188	0.000001906	-0.000001344
23	1	0.000000129	0.000001634	-0.000003551
24	6	-0.000003454	0.000001878	-0.000002244
25	1	-0.000001838	-0.000000850	-0.000002116
26	6	0.000001449	0.000000600	-0.000001882
27	1	0.000000550	0.000003438	-0.000003044
28	1	-0.000001424	-0.000001214	-0.000002189
29	1	-0.000000341	0.000001535	-0.000004127
30	77	-0.000009092	-0.000000431	0.000004974
31	1	0.000002099	0.000000180	-0.000001472
32	1	-0.000000529	-0.000003565	-0.000000724
33	8	0.000003387	0.000005447	-0.000004675
34	16	-0.000006319	0.000004483	0.000007255
35	8	0.000007580	-0.000002963	0.000002948
36	6	-0.000011166	0.000002596	-0.000007207

37	6	0.000002432	0.000003182	0.000018161
38	8	-0.000002825	0.000016147	0.000003219
39	6	0.000007201	-0.000029018	-0.000006121
40	6	-0.000000098	-0.000000983	-0.000001700
41	1	-0.000001147	-0.000002846	0.000004230
42	1	-0.000000112	-0.000002356	0.000003774
43	1	-0.000002827	-0.000004928	0.000003032
44	8	0.000000620	-0.000002281	0.000009020
45	8	0.000002611	0.000003553	0.000012803
46	6	0.000002337	0.000006443	-0.000003565
47	6	-0.000011198	-0.000006022	-0.000003466
48	1	0.000000633	0.000001647	0.000005637
49	8	0.000017230	0.000001406	-0.000002400
50	1	-0.000002585	-0.000005298	0.000001427
51	6	0.000009194	-0.000000840	-0.000005582
52	1	-0.000000027	0.000000618	0.000003002
53	1	0.000001102	0.000002413	0.000003170
54	1	0.000004163	0.000002278	0.000001364
55	6	-0.000006079	0.000003365	-0.000008369
56	1	0.000003453	0.000004718	0.000008111
57	1	0.000003936	-0.000001053	0.000000953
58	1	0.000005765	0.000001966	-0.000002374

---

13. Complex A1 prime Singly deprotonated at C1 (Gibbs Free Energy: -1955.055321a.u)

Center Number	Atomic Number	Atomic Type	Coordinates (Angstroms) X	Y	Z
1	6	0	2.170311	3.396265	-0.443929
2	6	0	3.324604	2.732858	-0.663644
3	1	0	1.955152	4.447709	-0.362054
4	1	0	4.331089	3.083625	-0.812792
5	6	0	1.680401	1.167958	-0.444627
6	7	0	1.175637	2.432760	-0.307136
7	7	0	3.017192	1.374046	-0.656904
8	6	0	-0.181202	2.729291	0.055637
9	6	0	-0.566894	2.571951	1.384203
10	6	0	-1.086913	3.142805	-0.914548
11	6	0	-1.891161	2.813757	1.741032
12	1	0	0.165564	2.243851	2.113347
13	6	0	-2.408648	3.390513	-0.548760
14	1	0	-0.761415	3.249508	-1.943140
15	6	0	-2.812532	3.219132	0.774630
16	1	0	-2.203568	2.683361	2.771533
17	1	0	-3.124848	3.704260	-1.300217

18	1	0	-3.845680	3.398609	1.052297
19	6	0	4.019859	0.350671	-0.739657
20	6	0	4.424578	-0.290259	0.429717
21	6	0	4.579454	0.026243	-1.970674
22	6	0	5.396165	-1.285081	0.358304
23	1	0	3.962279	-0.015076	1.370990
24	6	0	5.555827	-0.967799	-2.033441
25	1	0	4.243299	0.537168	-2.865812
26	6	0	5.960874	-1.625411	-0.872298
27	1	0	5.711939	-1.793805	1.262695
28	1	0	5.994164	-1.230545	-2.989934
29	1	0	6.717166	-2.401145	-0.925427
30	77	0	0.653490	-0.533739	-0.378298
31	1	0	2.021319	-1.239550	-0.644719
32	1	0	0.501345	-0.455595	-1.974905
33	8	0	1.814973	0.255734	2.727260
34	16	0	0.983634	-0.772339	1.985755
35	8	0	-0.557017	-2.330557	-0.329327
36	8	0	-1.508095	0.134740	-0.152024
37	6	0	-2.346097	-0.767904	-0.196168
38	6	0	-1.830653	-2.235772	-0.206328
39	8	0	-2.626687	-3.152378	-0.037145
40	6	0	-3.757460	-0.386980	-0.088793

41	1	0	-3.906988	0.489779	0.534889
42	6	0	-4.825786	-0.888092	-0.732184
43	6	0	-4.852315	-1.987712	-1.748688
44	1	0	-3.860027	-2.354737	-1.988314
45	1	0	-5.449375	-2.826606	-1.381895
46	1	0	-5.335935	-1.633898	-2.662586
47	6	0	-6.130990	-0.204118	-0.411950
48	8	0	-6.262122	0.742760	0.330995
49	8	0	-7.165260	-0.779677	-1.048917
50	1	0	-7.977376	-0.309961	-0.802226
51	6	0	1.684799	-2.412330	2.313125
52	1	0	1.726685	-2.579806	3.388901
53	1	0	1.056577	-3.148456	1.812403
54	1	0	2.681997	-2.413334	1.876777
55	6	0	-0.591648	-0.940042	2.878387
56	1	0	-0.373010	-1.081823	3.935956
57	1	0	-1.149047	-0.019230	2.717432
58	1	0	-1.141739	-1.791224	2.479119

14. Complex A2 prime Singly deprotonated at C1 (Gibbs Free Energy: -1955.035719 a.u)

Center Number	Atomic Number	Atomic Type	Coordinates (Angstroms) X	Y	Z

1	6	0	1.831176	3.412980	0.050763
2	6	0	2.994592	2.732826	0.031386
3	1	0	1.618458	4.459892	0.180820
4	1	0	4.014379	3.059838	0.136463
5	6	0	1.322043	1.219902	-0.304554
6	7	0	0.816915	2.485306	-0.163501
7	7	0	2.678499	1.394262	-0.194612
8	6	0	-0.567626	2.863501	-0.236279
9	6	0	-1.240435	3.203556	0.931331
10	6	0	-1.202926	2.898698	-1.473196
11	6	0	-2.582455	3.567928	0.860890
12	1	0	-0.724300	3.153655	1.882686
13	6	0	-2.544852	3.261784	-1.536689
14	1	0	-0.653437	2.623463	-2.365220
15	6	0	-3.236230	3.590620	-0.370213
16	1	0	-3.120979	3.813101	1.769511
17	1	0	-3.051779	3.282340	-2.495320
18	1	0	-4.285112	3.862586	-0.420531
19	6	0	3.702613	0.397000	-0.335801
20	6	0	4.489188	0.072357	0.763984
21	6	0	3.934805	-0.183324	-1.580919
22	6	0	5.518782	-0.855041	0.618327

23	1	0	4.289202	0.532258	1.724520
24	6	0	4.957111	-1.118341	-1.717118
25	1	0	3.316422	0.096237	-2.424941
26	6	0	5.749632	-1.454910	-0.618305
27	1	0	6.131005	-1.115298	1.474645
28	1	0	5.139107	-1.577505	-2.682579
29	1	0	6.547765	-2.181180	-0.728325
30	77	0	0.273617	-0.441646	-0.508707
31	1	0	1.565799	-1.119622	-1.064096
32	1	0	-0.036487	0.029976	-2.023714
33	8	0	2.202782	-2.004390	1.785269
34	16	0	0.893040	-1.254603	1.675773
35	8	0	-1.124669	-2.197811	-0.656561
36	6	0	-2.194570	-1.962426	-1.224423
37	8	0	-1.853964	0.241561	-0.023267
38	6	0	-2.557667	0.106143	1.023432
39	8	0	-2.237365	0.265037	2.204598
40	6	0	-4.249682	-1.700292	0.139391
41	1	0	-5.223669	-2.092738	0.423087
42	6	0	-3.506376	-2.445449	-0.693820
43	6	0	-3.928467	-3.792137	-1.209960
44	1	0	-4.885617	-4.095130	-0.785878
45	1	0	-4.013961	-3.777875	-2.300962

46	1	0	-3.176959	-4.547188	-0.958451
47	6	0	-4.001280	-0.354861	0.738713
48	8	0	-4.952214	0.330326	1.075180
49	8	0	-2.300834	-1.316708	-2.364135
50	1	0	-1.435950	-0.893588	-2.565130
51	6	0	0.913278	0.092330	2.889888
52	1	0	1.677249	0.798164	2.568567
53	1	0	-0.074521	0.550164	2.874757
54	1	0	1.159697	-0.324456	3.866231
55	6	0	-0.377316	-2.319413	2.415136
56	1	0	-1.278007	-1.732798	2.577431
57	1	0	-0.562960	-3.125649	1.709265
58	1	0	0.029675	-2.699984	3.351573

15. Complex A3 prime Singly deprotonated at C1 (Gibbs Free Energy: -1955.03513 a.u)

Center Number	Atomic Number	Atomic Type	Coordinates (Angstroms) X	Y	Z
1	6	0	0.729242	3.671636	0.188198
2	6	0	2.023996	3.301455	0.235557
3	1	0	0.253908	4.623228	0.352155
4	1	0	2.919044	3.861792	0.443451
5	6	0	0.807823	1.442403	-0.312974

6	7	0	-0.003964	2.537942	-0.151589
7	7	0	2.066290	1.944099	-0.079674
8	6	0	-1.429603	2.579755	-0.333686
9	6	0	-2.268358	2.502027	0.772935
10	6	0	-1.947121	2.731893	-1.617812
11	6	0	-3.649311	2.564399	0.587869
12	1	0	-1.852920	2.341487	1.759876
13	6	0	-3.327081	2.792530	-1.795944
14	1	0	-1.271096	2.789059	-2.462788
15	6	0	-4.178471	2.707665	-0.693506
16	1	0	-4.306033	2.469221	1.444335
17	1	0	-3.735881	2.902650	-2.794435
18	1	0	-5.253250	2.747366	-0.834680
19	6	0	3.299447	1.217066	-0.147259
20	6	0	4.074786	1.091883	1.005243
21	6	0	3.735714	0.689999	-1.360685
22	6	0	5.293446	0.418630	0.942536
23	1	0	3.719439	1.513495	1.939189
24	6	0	4.953765	0.017938	-1.414943
25	1	0	3.122093	0.807154	-2.243985
26	6	0	5.732647	-0.119699	-0.266193
27	1	0	5.894674	0.313727	1.838749
28	1	0	5.294122	-0.396797	-2.357289

29	1	0	6.679784	-0.645950	-0.312779
30	77	0	0.214613	-0.420630	-0.679227
31	1	0	1.149207	-0.455367	-1.942901
32	1	0	-0.880060	0.188573	-1.650799
33	8	0	2.843980	-2.472970	0.370333
34	16	0	1.737989	-1.542530	0.804020
35	8	0	-1.137457	-0.454206	1.114025
36	8	0	-0.507487	-2.405917	-0.992533
37	6	0	-2.891126	-1.843031	-0.924087
38	6	0	-3.829254	-2.101720	-2.069520
39	1	0	-3.302457	-1.962122	-3.020409
40	1	0	-4.174782	-3.138038	-2.050861
41	1	0	-4.691050	-1.432972	-2.050917
42	6	0	-1.720561	-2.818105	-0.879929
43	6	0	-2.370828	-0.556549	1.172282
44	6	0	-3.094762	-0.147016	2.507797
45	8	0	-2.364387	0.337918	3.393631
46	8	0	-4.331264	-0.336941	2.504120
47	6	0	-3.200114	-0.953679	0.039517
48	1	0	-4.180718	-0.492090	0.030803
49	8	0	-2.041839	-4.030586	-0.778727
50	1	0	-1.441716	-4.565952	-1.302974
51	6	0	2.368809	-0.480314	2.085490

52	1	0	1.825773	-0.652772	2.991178
53	1	0	3.405511	-0.691361	2.245518
54	1	0	2.254343	0.541713	1.790095
55	6	0	0.674573	-2.421795	1.928493
56	1	0	0.059410	-3.103055	1.378620
57	1	0	1.270474	-2.966484	2.630715
58	1	0	0.054591	-1.724394	2.452089

16. Complex E1 Singly deprotonated at C1 (Gibbs Free Energy: -1955.052399 a.u)

Center Number	Atomic Number	Forces (Hartrees/Bohr) X	Y	Z
1	77	-0.000002916	-0.000007581	0.000001187
2	1	0.000000713	0.000001533	-0.000001384
3	6	-0.000000986	0.000000405	0.000000534
4	6	-0.000005069	-0.000003849	-0.000000929
5	1	-0.000000437	0.000001075	-0.000000936
6	1	-0.000001400	0.000000371	0.000000194
7	6	-0.000004639	0.000005433	-0.000001319
8	7	0.000003436	0.000000983	-0.000000321
9	7	-0.000000105	-0.000000638	0.000001500
10	6	-0.000001217	0.000000934	-0.000001100

11	6	-0.000000399	0.000002170	-0.000001169
12	6	0.000001479	0.000000828	-0.000000439
13	6	0.000001187	0.000002106	-0.000001112
14	1	-0.000000140	0.000002122	-0.000001163
15	6	0.000001362	0.000001625	-0.000001055
16	1	0.000002506	0.000000643	-0.000001783
17	6	0.000002177	0.000002387	-0.000001314
18	1	0.000000712	0.000003270	-0.000001849
19	1	0.000002472	0.000001552	-0.000000453
20	1	0.000002244	0.000002751	-0.000001318
21	6	-0.000002348	-0.000000616	-0.000001163
22	6	-0.000002760	0.000001860	0.000000200
23	6	-0.000000203	-0.000000753	-0.000001688
24	6	-0.000003115	-0.000000510	0.000001083
25	1	-0.000002657	0.000000524	-0.000000576
26	6	-0.000002720	-0.000002428	0.000002079
27	1	-0.000002080	-0.000002097	0.000000388
28	6	-0.000003996	-0.000001638	-0.000000370
29	1	-0.000003270	-0.000000314	-0.000000223
30	1	-0.000002822	-0.000002567	0.000000893
31	1	-0.000003532	-0.000001631	0.000000418
32	8	-0.000000207	0.000001889	0.000000186
33	16	0.000000681	0.000001448	-0.000005016

34	1	-0.000001382	0.000001024	0.000000702
35	8	0.000007039	0.000007290	-0.000000808
36	8	-0.000002636	0.000003155	0.000002149
37	6	-0.000001085	-0.000005745	-0.000004895
38	8	0.000000934	0.000001672	0.000001312
39	6	0.000000893	-0.000004717	0.000005090
40	6	0.000000195	-0.000000468	0.000001984
41	1	0.000001808	-0.000000215	0.000001851
42	6	0.000003277	-0.000002369	-0.000000118
43	6	-0.000001491	-0.000002617	0.000001868
44	1	0.000000136	-0.000002413	0.000002246
45	1	0.000000380	-0.000001244	0.000001651
46	1	0.000000431	-0.000001821	0.000001928
47	6	0.000005672	-0.000007154	0.000005417
48	8	0.000000061	-0.000003614	0.000001978
49	8	-0.000000454	0.000001348	-0.000002558
50	1	0.000003299	-0.000003054	0.000002208
51	6	0.000001073	-0.000005645	0.000002675
52	1	0.000001820	0.000002156	0.000000058
53	1	0.000001964	0.000001046	-0.000000657
54	1	0.000000550	0.000001892	-0.000001024
55	6	0.000004924	0.000002279	-0.000000496
56	1	-0.000000347	0.000002801	-0.000000965

57	1	-0.000000804	0.000002858	-0.000002573
58	1	0.000001792	0.000002267	-0.000001005

---

17. Complex E2 Singly deprotonated at C1 (Gibbs Free Energy: -1955.061097 a.u)

Center Number	Atomic Number	Forces (Hartrees/Bohr) X	Y	Z
1	77	-0.000007926	0.000003764	-0.000002447
2	1	-0.000000732	-0.000001190	0.000000263

3	6	-0.000000105	-0.000003198	0.000004903
4	6	0.000002215	0.000001477	-0.000003103
5	1	0.000001715	-0.000000159	-0.000003047
6	1	0.000002426	0.000000754	-0.000004578
7	6	0.000002328	0.000000787	0.000000392
8	7	0.000000340	0.000001374	-0.000008837
9	7	-0.000000677	-0.000002631	0.000001399
10	6	0.000001891	-0.000002617	-0.000000246
11	6	-0.000000644	-0.000002047	-0.000001876
12	6	0.000000380	0.000000121	0.000000110
13	6	0.000001601	-0.000002881	-0.000001575
14	1	0.000000667	-0.000002162	-0.000002222
15	6	-0.000000860	-0.000000790	-0.000001005
16	1	0.000001360	-0.000000298	-0.000000924
17	6	0.000000550	-0.000001264	-0.000002310
18	1	0.000000349	-0.000002891	-0.000002325
19	1	0.000000178	-0.000000897	-0.000000463
20	1	-0.000000045	-0.000002435	-0.000001166
21	6	0.000001875	0.000000267	0.000001504
22	6	0.000001402	-0.000001037	0.000000310
23	6	-0.000000396	0.000000592	-0.000001619
24	6	-0.000000317	0.000000285	-0.000000120
25	1	-0.000000006	-0.000001067	-0.000001013

26	6	0.000001411	0.000001534	0.000000043
27	1	0.000001194	0.000002076	-0.000001572
28	6	0.000000186	0.000001216	-0.000000507
29	1	0.000000033	-0.000000248	-0.000000118
30	1	0.000001264	0.000002084	-0.000000116
31	1	0.000000556	0.000001090	0.000000139
32	8	-0.000003838	-0.000000509	-0.000000425
33	16	0.000001976	0.000000767	0.000000964
34	1	0.000000554	-0.000001277	0.000000698
35	8	0.000006388	-0.000003567	-0.000003656
36	6	-0.000007825	0.000002495	0.000002096
37	6	0.000003348	0.000002166	-0.000002505
38	6	-0.000001100	0.000003275	0.000002346
39	1	0.000000238	0.000002402	0.000001658
40	1	-0.000000483	0.000002384	0.000002067
41	1	0.000000048	0.000003116	0.000001416
42	6	0.000002411	0.000004852	0.000004674
43	1	-0.000000807	0.000001593	0.000000460
44	6	-0.000001313	-0.000000223	-0.000006598
45	8	0.000000298	-0.000001463	0.000002395
46	8	-0.000004305	-0.000002773	0.000003367
47	6	0.000008802	0.000004562	0.000002499
48	8	-0.000002847	0.000001574	0.000000954

49	8	-0.000000534	0.000001578	0.000006148
50	1	0.000001716	0.000001544	0.000000002
51	6	-0.000004401	-0.000000299	-0.000000753
52	1	-0.000001528	-0.000001933	0.000003746
53	1	0.000000059	0.000000413	0.000001860
54	1	-0.000000097	-0.000000257	0.000002599
55	6	-0.000004480	-0.000003395	0.000003955
56	1	-0.000002546	-0.000002311	0.000001590
57	1	-0.000001519	-0.000001954	-0.000000016
58	1	-0.000000423	-0.000002366	0.000000586

---

18. Complex E3 Singly deprotonated at C1 (Gibbs Free Energy: -1955.030590 a.u)

Center Number	Atomic Number	Forces (Hartrees/Bohr) X	Y	Z
1	77	0.000010318	0.000016274	-0.000001926
2	1	-0.000000279	0.000000911	0.000004940
3	6	0.000000915	0.000012449	-0.000001929
4	6	0.000007369	0.000006677	-0.000010720
5	1	-0.000000075	-0.000002206	0.000004952

6	1	-0.000003183	-0.000000523	0.000004455
7	6	0.000018618	0.000024509	0.000011168
8	7	-0.000011769	-0.000032075	-0.000008144
9	7	-0.000010043	-0.000012089	0.000002327
10	6	-0.000004141	0.000010846	0.000004246
11	6	0.000001158	-0.000003937	0.000005161
12	6	-0.000003918	0.000063256	-0.000003515
13	6	0.000000805	-0.000001449	0.000006430
14	1	-0.000000096	0.000001200	0.000004268
15	6	0.000000631	-0.000002121	0.000007060
16	1	0.000001182	-0.000055379	0.000003986
17	6	0.000000540	0.000001765	0.000002162
18	1	0.000000837	0.000001609	0.000004821
19	1	-0.000001254	0.000000750	0.000003502
20	1	0.000000103	0.000001420	0.000004921
21	6	0.000001363	-0.000000243	0.000003519
22	6	0.000003308	0.000003048	0.000001664
23	6	-0.000002024	0.000001593	-0.000005312
24	6	0.000006954	0.000001814	0.000000772
25	1	0.000002170	-0.000000930	-0.000001575
26	6	0.000001232	0.000003154	-0.000007617
27	1	0.000000011	-0.000001841	-0.000001980
28	6	-0.000001035	-0.000002234	-0.000002520

29	1	0.000001699	-0.000001119	-0.000002280
30	1	-0.000001824	-0.000000786	-0.000003056
31	1	0.000004848	0.000004366	-0.000001853
32	8	0.000004224	-0.000003132	0.000006008
33	6	0.000039046	-0.000002244	-0.000008492
34	8	-0.000013066	-0.000004402	0.000015612
35	6	-0.000015092	0.000008124	-0.000018782
36	6	-0.000019035	-0.000006494	-0.000021147
37	6	0.000005033	0.000000368	-0.000000770
38	1	-0.000004398	0.000000116	-0.000001485
39	1	-0.000004265	-0.000004702	-0.000001418
40	1	-0.000001159	-0.000002574	0.000000359
41	6	0.000013183	-0.000010840	-0.000013600
42	8	-0.000003948	-0.000001203	-0.000001233
43	8	-0.000002964	-0.000001690	0.000007350
44	6	-0.000005519	-0.000007284	0.000006834
45	1	-0.000001552	0.000000802	0.000000990
46	8	0.000005696	0.000029996	-0.000009343
47	16	0.000006800	-0.000036505	-0.000007174
48	1	0.000002336	-0.000000439	0.000012092
49	8	-0.000038060	0.000094346	0.000029235
50	1	-0.000000625	-0.000092948	-0.000018185
51	6	-0.000011855	-0.000007931	0.000018223

52	1	0.000007123	0.000002410	-0.000001869
53	1	0.000006254	-0.000004271	-0.000007247
54	1	0.000002739	0.000010899	-0.000000749
55	6	0.000000146	-0.000014983	-0.000001148
56	1	0.000002008	-0.000002913	-0.000002314
57	1	0.000000133	0.000010140	-0.000002651
58	1	0.000002400	0.000008644	-0.000007023
